DISSERTATION

MOLECULAR DYNAMICS SIMULATION STUDIES AND EXPERIMENTAL MEASUREMENTS OF RADIOFREQUENCY HEATING FOR STRONGLY COUPLED AND EXTREMELY MAGNETIZED ULTRACOLD NEUTRAL PLASMAS

Submitted by

Puchang Jiang

Department of Physics

In partial fulfillment of the requirements

For the Degree of Doctor of Philosophy

Colorado State University

Fort Collins, Colorado

Fall 2023

Doctoral Committee:

Advisor: Jacob L. Roberts

Dylan Yost
Siu Au Lee
Azer Yalin

ABSTRACT

MOLECULAR DYNAMICS SIMULATION STUDIES AND EXPERIMENTAL MEASUREMENTS OF RADIOFREQUENCY HEATING FOR STRONGLY COUPLED AND EXTREMELY MAGNETIZED ULTRACOLD NEUTRAL PLASMAS

Ultracold neutral plasmas(UNPs) are good experimental platforms for fundamental plasma physics studies because of their experimentally adjustable parameters, accessible timescales, ability to enter the strong coupling parameter regime, and easy access to large degrees of electron magnetization. The work in this thesis contains both simulation and experimental studies of UNPs. One simulation project describes a new UNP heating mechanism discovered using Molecular Dynamics simulations: DC electric field heating. This DC electric field heating mechanism occurs when a DC electric field is present when the plasma is formed. sets a lower limit of how cold UNP electron temperatures can be reached experimentally. A second simulation project investigates a many-body physics effect on collisional damping in UNPs and a breakdown in standard plasma theory treatments when the plasma is approaching the strongly coupled regime. This breakdown arises due to the increasing significance of three- or many-body electron-ion interactions influencing the plasma transport properties and particle collisions. My simulations find evidence for this being the case. Experimental studies of UNP electron-ion collision physics during the application of high-frequency RF electric fields to the UNP were conducted, and measurements of the RF-induced electron heating rate from the weak magnetized regime to extremely magnetized regime were performed. The results obtained are in qualitative agreement with the theory prediction but there's quantitative disagreement. Possibilities for resolving this disagreement are presented.

ACKNOWLEDGEMENTS

Doing physics research is fascinating but sometimes hard. I would like to thank Professor Jacob Roberts for offering me unconditional help and always being patient when I get confused or stuck on certain projects. Diagnosing a problem can be frustrating because there are so many steps and tests on the checklist, sometimes I don't have a complete view of the problems, or I just don't have enough knowledge. At those moments professor Roberts would help me through, explain things patiently and find key points I left out. Sometimes I have difficulties in study or in personal life, he's always there supporting me and ready for all kinds of conversation. I'm a shy person and usually I feel better when I'm alone but having conversation with him never makes me stress and I always feel comfortable when I speak out and express my thoughts. I want to thank him from the bottom of my heart, not only for guiding me through my degree, but also for setting up an example of what I can improve to make myself a better person.

I would also like to thank a bunch of graduate students who did research with me together. Thank Dr. John Guthrie and Dr. Weiting Chen for teaching me most of the experiment procedure and basic plasma concepts. John is good at explaining difficult and confusing concept using simple words and I benefit from this quite a lot. Thank Dr. John Gilbert as we become close friends and being supportive for my living and studying in US. We talked a lot when we are in the office or meet at gym, I enjoy talking with John and still treasure those memories. Thank Bridget and Ryan for helping me through the main experiment project I was working on, otherwise I couldn't collect enough data points every day which potentially leads to lager error bars in the end. Thanks to the Air Force Office of Scientific Research for funding these projects.

TABLE OF CONTENTS

LIST OF TABLES

LIST OF FIGURES

Chapter 1

Introduction

Ultracold neutral plasmas (UNPs) [1,2] are a kind of plasma created in laboratories with table-top-scale apparatuses. They contain two or more particle species: electrons plus one or more types of ions. UNP formation often starts with an ultracold atom gas cloud whose temperature is below 1mK. That cloud is photoionized to create free electrons and ions from the ultracold atoms. Some of the electrons escape right away after the photoionization, while the much higher mass ions do not since their velocities are far lower. This electron escape results in a positive space charge that eventually confines the electrons, thus forming a UNP. Plasma physics experiments can then be conducted on the UNPs.

UNPs have good diagnostics available [3] and controllable initial conditions. They are a clean and relatively pure system for plasma research. The ionization state is known exactly in UNPs, which often is not the case in other plasmas – and uncertainty in the distribution of charge states complicates the analysis of experimental measurements in these other plasmas. The fact that the electrons are cold enough that they do not have significant interactions with neutral atoms also contributes to the relative simplicity of the physics of UNPs. The electron and ion temperatures both can be as low as a Kelvin [4, 5]. This is advantageous for exploring unusual and extreme plasma conditions. Cold temperatures lead to interesting particle behavior such as strong coupling [4,6,7], three-body recombination [8–10], and significant magnetization in applied magnetic fields [11]. Besides their cold temperature, UNPs have another relatively rare feature compared to other highly ionized plasmas: they have comparatively low density. Typical densities for UNPs in our experiments are around $10^{13}m^{-3}$, which is several orders of magnitude less than many other laboratory plasmas. Low temperature and low density mean slower electron speed and plasma evolution timescales. This makes it possible to use moderately fast electronics to measure UNP dynamics, which is a simplification compared to many other plasma systems. Combining all these

advantages, UNPs allow the exploration of comparatively extreme plasma conditions in a table-top-scale experimental apparatus.

The physics of particle collisions in UNPs is a topic that we are studying in many of our projects. In previous work done by a former graduate student Weiting Chen [4], strong coupling was found to have a larger influence on electron-ion collision rates than what was initially predicted in theory. Strongly-coupled plasmas are those where the typical nearest-neighbor Coulomb energy between plasma particles is comparable to the thermal energy $k_B T$. These conditions break common assumptions used in the theoretical description of these plasmas and introduce particle correlation effects. While not the main focus of that work, an unreported heating mechanism caused by DC electric fields was discovered through UNP simulations. This heating mechanism can be significant at lower densities, becoming the main limitation for the lowest achievable temperatures [12]. There had been no detailed simulation of this heating mechanism, so I performed work that looked at how the heating rate scaled with respect to changes in density and initial electron temperature as well as providing a means to estimate how large this heating was likely to be. Due to this heating effect, there is a low-temperature limit to what can be achieved in the electron component of UNPs whenever a DC electric field is present, and this limitation in part determines the degree of strong coupling strength UNPs can reach. This work is described in chapter 4 on DC electric field heating in this thesis.

Particle collisions also cause the damping of center-of-mass oscillations that result from an initial displacement between electron and ion centers of mass. The theory prediction of the damping rate breaks down when UNPs enter the strongly coupled regime. It turns out that this is in part due to the fact that typical theory treatments only consider binary collisions between electrons and ions. We traced simulated electron trajectories using Molecular Dynamics (MD) simulation methods and studied the electron collision deflections [13]. We analyzed the simulations to show that many-body collisions also contribute to oscillation damping in addition to binary collisions for the degree of strong coupling that could be obtained in the electron component of UNPs at experimentally accessible low temperatures. That is because some electrons can be temporarily bound to a

single ion or a small cloud of ions and then scatter back to an unbound state via electron-electron collisions. This process contributes significantly to the oscillation damping rate because of the momentum transfer between electrons and ions that results from this binding/scattering process. We found the discrepancies between theory and the simulation cannot be ignored even in the moderate coupled regime if at least moderate accuracy in the theory predictions is desired. The simulation work on the effect of many-body physics on oscillation damping rates is presented in chapter 5 in this thesis.

UNPs are easier to magnetize because the interparticle spacing, mean free path and several other length scales are longer than in hot and dense plasmas while the length scale describing the degree of magnetization can easily be made to be shorter than these other scales in UNPs. This is particularly true for the electron component of the UNPs. Electron magnetization effects can easily dominate multiple elements of plasma dynamics. We studied UNP AC conductivity under the influence of a magnetic field. A natural prediction would be for the conductivity to increase with applied magnetic field since the electrons would increasingly be pinned to the magnetic field lines. However, 180-degree collisions are always possible. Further, the magnetic field also influences the screening in sufficiently magnetized plasmas. So, the prediction that the conductivity along the magnetic field direction increases with increasing magnetization may not happen after all, and indeed that is what we observed.

We conducted experiments and simulations measuring the UNP heating rate when applying an off-resonance radiofrequency (RF) electric field to the UNP when different magnetic fields were applied. This RF field can drive electron-ion collisions and momentum transfers thus heats up the UNP. The heating rate is associated with the electron ion collision rate. We compared the theory predictions, experiment, and simulation results and found that the theory and simulation predictions qualitatively agree with the experimental results, but at present there are quantitative differences. These experiment results are exciting because they represent some of the first laboratory measurements conducted with extreme magnetization conditions for the electrons. Also, they suggest that further development of these theories and simulations are necessary, which is relevant

not only to UNP physics but to other magnetized plasmas as well. Magnetic fields are present in astrophysical systems like white dwarf atmospheres [14] and fusion-relevant plasmas in ICF – where magnetic fields are being added deliberately to improve ICF stability [15] – and in MagLIF fusion experiments [16]. In some cases, the degree of magnetization in these other systems is much less than what we can achieve, but by encouraging better theoretical understanding we can improve the state-of-the-art in predicting and modeling the relevant plasma physics in these systems.

Chapter 2 is an overview of relevant plasma parameters and basic plasma physics such as plasma oscillations, three-body recombination physics, strong coupling and plasma heating mechanisms. I also discuss length scales, how these length scale affect particle collisions and other plasma physics mentioned above, and how the UNP length scales compare with other plasmas. These length scales also characterize plasma magnetization. In addition, I explain the experimental details of UNP production and measurement in our apparatus.

In chapter 3, I present details about the simulation work I've done in the past few years, starting with a brief introduction of the molecular dynamics (MD) simulation algorithm, which is a commonly used tool to look at plasma evolution and plasma properties. I also discuss its limitations and current difficulties that we have with the simulation. After this material is presented, I use the MD simulation to characterize show the electron temperature will rise in UNPs when a DC electric field exists at the time of plasma formation, discover that in strongly coupled UNPs not only the binary collisions but also the many-body interaction collisions plays an important role in UNP oscillation damping and so it contributes to the damping rate of oscillations in the plasma as described above and in more detail in chapter 5. I report studies of the RF off-resonance heating under different degrees of magnetization and had some preliminary simulation results that can be compared to our experimental results in chapter 6.

Chapter 6 presents the details of RF off-resonant heating experiments that were performed. It includes a description of how we do the measurements, necessary calibrations, and checks on the assumptions made concerning the experiment. It also presents the results of off-resonant RF heating rate measurements as a function of electron magnetization. This includes the calculated

RF heating rate and the associated error bars under several different magnetic fields. The MD simulation, theory predictions and the experiment results are all compared and the implications of that comparison are discussed. Our experiment results show both MD simulations and the theory prediction have their own defects as they are not in agreement in certain magnetized regime. Possible explanations are given.

Chapter 2

Basic Plasma Physics

This chapter touches briefly on several aspects of basic plasma physics that are relevant to the scientific work presented in this thesis. The material in this chapter is meant to be a overview of these properties rather than an exhaustive treatment. For additional details, the reader is referred to the references in each section.

2.1 Plasma properties and length scale

Plasma is one of the four states of matter. It is made up of free electrons and ions under conditions where these particles behave collectively [17, 18]. One special characteristic of a plasma is the screening effect: When electrons are attracted by a nearby ion they form a volume of increased negative charge around the positive ion, and the electrons outside the volume feel less electric field force due to the screening. The volume is often called the Debye sphere, and the radius of Debye sphere is called Debye screening length λ_D.

$$\lambda_D = \sqrt{\frac{\epsilon_0 k_B T_e}{n_e e^2}} \tag{2.1}$$

λ_D is a function of plasma density n_e and electron temperature T_e. ϵ_0 is the vacuum permittivity, k_B is the Boltzmann constant and e is the fundamental charge. A collection of free charged particles is not a guarantee of having a plasma. It's necessary that λ_D is smaller than the object size so that particles have collective behavior required to be considered a plasma.

Plasma density, temperature and size cover a huge range of magnitude. Fusion plasma temperatures can reach to $10^8 K$, while ultracold plasma can be as cold as $1K$ or colder [7]. The core of the sun has a density around $10^{33} m^{-3}$, while the interstellar medium only has a density around $10^5 m^{-3}$. Because of the wide variety of temperature and density, particle interactions and plasma lifetimes have huge differences. To characterize the particle interaction, several plasma

length scales can be introduced for convenience and comparison, the importance of the physics associated with each length scale can be determined by comparing its length scale to other length scales. The Debye length is one of them. Besides the Debye length, there are mean free path λ_{col}, average interparticle spacing a_{WS}, and distance of closest approach r_L which can be expressed as follows:

$$\lambda_{col} = 3\sqrt{\frac{\pi}{2}}\frac{(k_B T_e)^2 4\pi\epsilon_0^2}{ln(\Lambda)ne^4} \tag{2.2}$$

$$a_{WS} = (\frac{3}{4\pi n_e})^{1/3} \tag{2.3}$$

$$r_L = \frac{e^2}{4\pi\epsilon_0 k_B T_e} \tag{2.4}$$

Note that the ln(Λ) term is the Coulomb logarithm [17], and Λ will be defined in section 2.4. These length scales can be orders of magnitude different, or they can have similar ratios in different plasmas with orders of magnitude variations in temperature and density. UNPs created in our lab have an electron temperature T_e tunable from 1K-1000K with an ion temperature T_i around 0.1K. The particle density is around $10^{13}/m^3$. Figure 2.1 shows a typical temperature and density value for different kinds of plasmas. More detailed length scale values for UNPs we created in our lab are listed in the Table 2.1 below.

Table 2.1: UNP Parameters

Parameter	**Value**
Electron Temperature (T_e)	1 K - 1000 K
Ion Temperature (T_i)	0.1 K
Density(n_e)	$10^{13}m^{-3}$
Particle Number(N_e)	1 million
Mean Free Path (λ_{col})	1 mm

2.2 Strong Coupling

In most plasmas, the thermal energy of the electrons and ions is much greater than the Coulomb potential energy between nearest-neighbor particles. In these weakly-coupled plasmas, there are no

significant spatial correlations between particles and many simplifying assumptions can be applied to the plasma, such as the assumption that there are many particles (e.g. electrons) in a Debye screening volume (λ_D^3). [18]. The coupling strength in a plasma is defined via a dimensionless parameter Γ as

$$\Gamma = \frac{e^2}{4\pi\varepsilon_0 a_{WS}} \cdot \frac{1}{k_B T}. \tag{2.5}$$

Γ is the ratio between the nearest-neighbor Coulomb energy of particles in the plasma and the thermal energy of those particles.

As either the density of the plasma is increased (making a_{WS} smaller) or the temperature is decreased, the value of Γ increases. As Γ approaches 1, the plasma is then no longer weakly-coupled and begins to enter the strongly-coupled regime. Strongly-coupled plasma develop spatial correlations between the particles in the plasma, and in extreme cases can make phase transitions to liquid and solid states [19] for Γ values greater than 1 and much greater then one, respectively. Even for moderately coupled plasmas where $0.1<\Gamma<1$ many of the standard assumptions for weakly-coupled plasmas break down. In addition, long-range interactions become important. Previous work with UNPs at CSU examined the effect of strong coupling on collision rates and found that while careful application of existing theories matched the experimental measurements better than a more naive application, there were still discrepancies [4]. These discrepancies are the subject of chapter 5 in this thesis.

To get a sense of how strongly-coupled different plasma systems are, refer to Figure 2.1. The red line in that plot represents the border separating the weakly and strongly coupled plasmas ($\Gamma = 1$). UNPs can be strongly coupled due to the cold temperature they can reach.

2.3 Three-body recombination

Three-body recombination (TBR) is a collisional process happening throughout the plasma lifetime [20]. When two electrons collide near an ion, one electron has a chance to become bound to the ion and form a neutral Rydberg atom. The other electron will carry away the extra kinetic energy, which leads to an increase in electron temperature. The TBR rate ν is heavily dependent

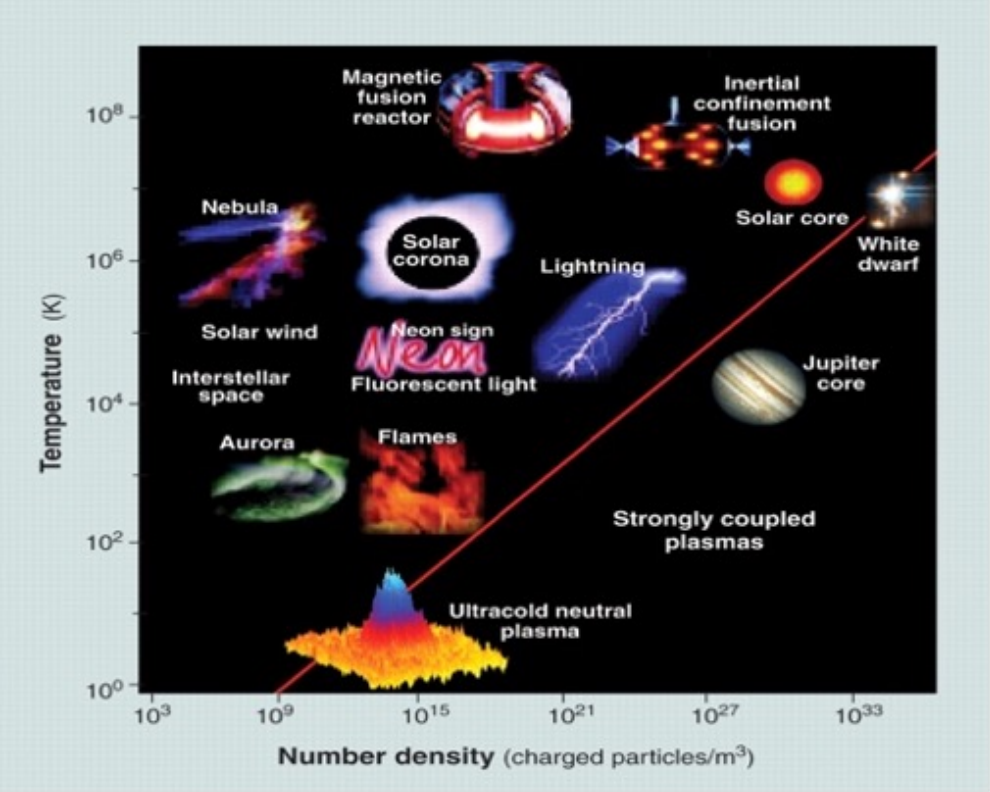

Figure 2.1: A figure shows the plasma density vs plasma temperature. The red line represents the border separating the weakly and strongly coupled plasmas [6]

on electron temperature for weakly-coupled plasmas: $\nu \sim n^2 T^{-9/2}$. This relation is justified by experiments and simulations in hotter plasmas, but breakdown is expected when it goes to ultracold and strongly-coupled regime [10]. Three-body recombination rates are not explicitly studied as part of this thesis, but they are relevant to the understanding of electron oscillation damping in strongly-coupled plasmas (see chapter 5).

2.4 Plasma Oscillations

Plasma particles have collective behavior. As an example, consider displacing the electrons' center of mass by a tiny amount. The electron cloud will oscillate as the Coulomb force between electron and ion clouds acts as the restoring force. The electron oscillation frequency $\omega 9_p = \sqrt{\frac{n_e e^2}{m_e \epsilon_0}}$ can be derived by setting up Maxwell's equations and the charge continuity equation. In a UNP, such oscillation will damp out due to the momentum transfer between electrons and ions because of the electron-ion collisions. The energy in the oscillation will eventually turn into electron thermal energy. Considering a classical Rutherford scattering picture of an electron colliding with an ion, the electron momentum change can be expressed as

$$\Delta\, p_z \;=\; -2|\mathbf{p}| \sin^2\left(\frac{\chi}{2}\right) \tag{2.6}$$

Averaging over all the possible χ and changing variables from χ to the maximum impact parameter b we can obtain the average momentum transfer rate equation:

$$\langle \dot{\mathbf{p}} \rangle = -\frac{ne^4}{4\pi\epsilon_0^2 m_e v^2} ln\Lambda \tag{2.7}$$

All impact parameters are possible, but mathematically only some are allowed if divergence of the collision rate is to be avoided. Equation (2.7) is derived with the assumption that the minimum impact parameter is 0 and maximum possible impact parameter is b_{max} which is proportional to λ_D. $ln\Lambda$ is the Coulomb logarithm and $\Lambda = \sqrt{1 + b_{\max}^2/b_\perp^2}$. $b_\perp$is the characteristic impact parameter when $\chi = \pi/2$. The value of $b_{\max}$ is taken to be 0.765 λ_D following [21–23]. The use of λ_D as

the impact parameter cutoff is motivated by the fact that screening prevents significant collision interactions if the impact parameter is larger than the screening length. Electron oscillation damping can thus be used to measure electron-ion collision rates, but applying a binary-collision theory alone and expecting agreement with experimental measurement requires that three- and higher-body collisions not be relevant. As has been mentioned at other points in this chapter, this is not necessarily the case for plasmas with Γ approaching 1.

2.5 Charged Particle Motion in Magnetic Fields

In the presence of a magnetic field, electrons and ions undergo what is known as cyclotron motion, driven by the Lorentz force. A length scale called the cyclotron radius is associated with this motion, which characterizes the radius of the particle's circular trajectory(see Figure 2.2). The cyclotron radius for an individual particle can be expressed as

$$r_c = \frac{mv_\perp}{|q|B} \tag{2.8}$$

To characterize a typical value of r_c associated with a gas or particles, the numerator in the above equation can be replaced by $\sqrt{mk_BT}$. As the magnetic field strength increases, the average electron cyclotron radius decreases. Eventually, it can become smaller than the values of λ_{col}, r_L, and λ_D. As the value of r_c becomes smaller than each of these values in turn as the magnetic field increases, the effects of magnetization have significant impact on basic plasma properties. [11] As r_c becomes less than λ_{col}, transport rates are affected. Likewise, the magnetic field affects screening as r_c becomes smaller then λ_D. When r_c is less than r_L the magnetic field influences binary collisions. Figure 2.3 illustrates the various magnetized regimes based on the relationship between r_c and other length scales. Our study of particle collisions in UNP spanned the weakly to extremely magnetized regimes.

The length scale r_L, typically the smallest among all characteristic length scales in unmagnetized plasmas, is inversely proportional to the electron temperature T_e. In contrast to hotter and

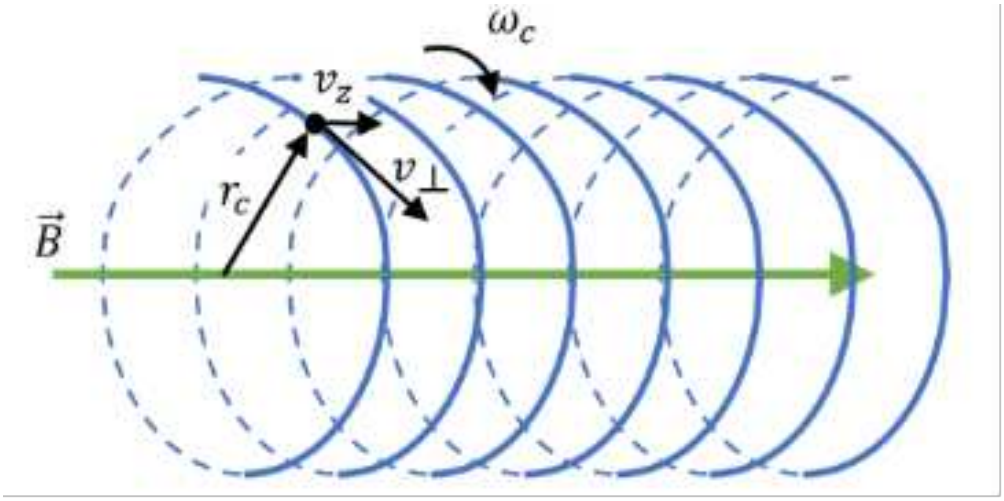

Figure 2.2: electron cyclotron motion under the influence of a magnetic field [24]

denser plasmas, and not only for r_L, these length scales are significantly larger in UNPs, which makes it easier for r_c to become the smallest length scale in the plasma even when moderate laboratory-scale magnetic fields are applied. This is especially true for the electron component of the plasma. The scaling of the cyclotron radius to other length scales can be expressed via a ratio and depends on the electron temperature and/or density. For example: $r_c/\lambda_D \sim n^{1/2}$, $r_c/r_L \sim T_e^{3/2}$. Magnetic field effects are thus expected to be significant for collisions and screening when T_e and n are smaller. The electron component of UNPs can become extremely magnetized at a few hundred Gauss while magnetic fields of thousands or millions of Tesla are required to achieve comparable magnetization in hotter plasmas. For example, 100G for a T_e=1K UNP is equivalent to 10^6T at 10^5K in terms of extreme magnetization, with this latter temperature being typical of that found in a white dwarf atmosphere. Thus, astrophysical degrees of magnetization can be achieved in a laboratory setting with UNPs. Through dimensionless scaling relations of the different characteristic plasmas lengths, the results of UNP experiments inform theories that are applicable to hotter and denser plasmas as well.

When dealing with magnetized plasmas, studying their dynamics poses theoretical challenges. Unlike the unmagnetized case, electron scattering within the field of an ion most often lacks an analytical solution. The complexity of electron trajectories far exceeds the simple Rutherford scat-

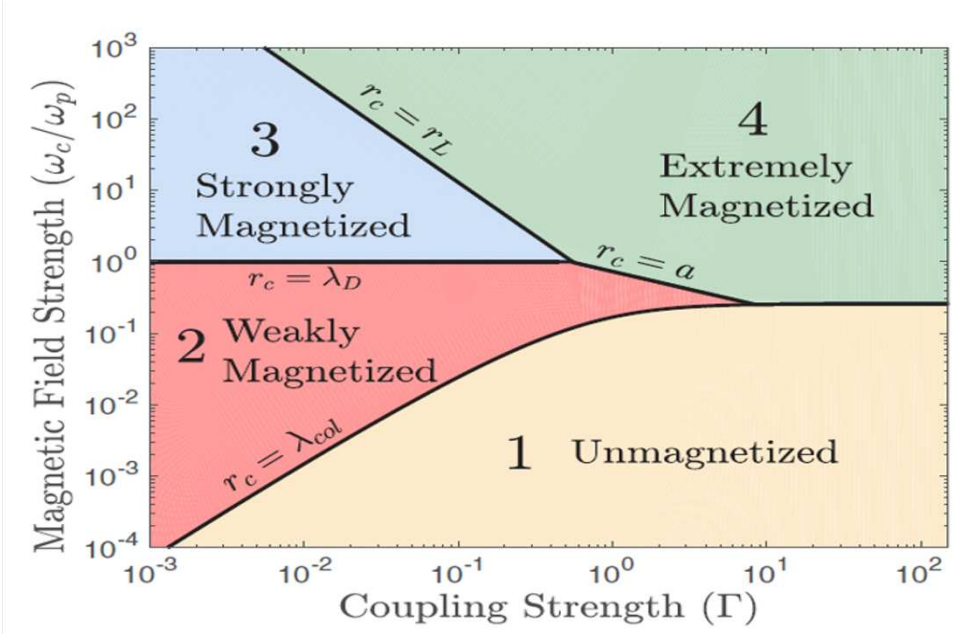

Figure 2.3: Plasma different magnetized regime [11]

tering pattern, as depicted in Figure 2.4. [25] Complicating matters further, the relation between impact parameter and deflection angle exhibits chaotic and fractal behavior within certain parameter ranges [25]. This will lead to mathematical difficulties calculating an average momentum transfer through the binary collision picture when studying electron-ion collision rates in magnetized UNPs. For sufficiently weakly-coupled plasmas where binary collisions can be treated pertubatively, these issues are not expected to be as important [26]. There are alternative theories that approach the issue from a macroscopic perspective – treating the electron component as a fluid and attempting to calculate its associated dielectric function [27]– mathematical challenges arise during these calculations and approximations are necessary. Given these complexities, the exploration of electron-ion collisions benefits from experimental and simulation methods. These approaches offer practical ways to explore this challenging yet crucial plasma regime.

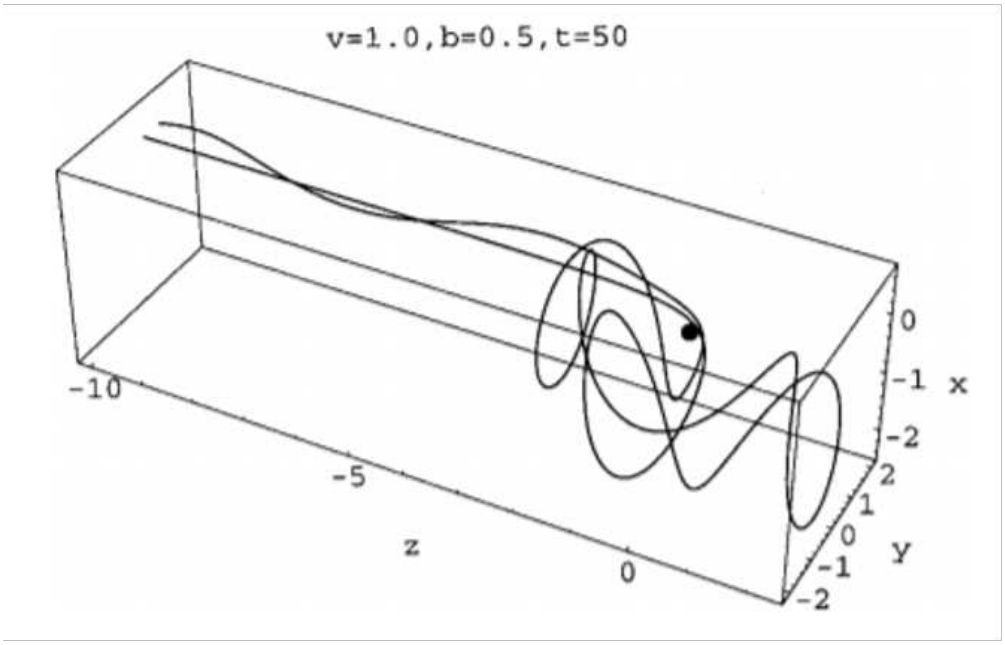

Figure 2.4: An example of electron trajectory under the influence of a magnetic field [25]

2.6 UNP Formation and Overview of Experimental Apparatus and Simulation Methods

Measuring the electron-ion collision rate experimentally requires a signal that is dependent or at least sensitive to that collision rate. For instance, a method developed by former graduate student Wei-Ting Chen [4] measures the plasma oscillation damping rate through using an electron escape signal. This damping rate shares a close correlation with the electron-ion collision rate.

While useful, that method was found to have two drawbacks when we considered using it for measuring electron-ion collision rates in magnetized plasmas. The first is that sensitive tuning of the electric field environment was needed to ensure that the electron escape signal used in the oscillation damping measurement was primarily associated with the damping. When we updated the electrodes in our experimental apparatus, we found that there were parameters where contaminating electron signals were present. These could be tuned away, but they did add complications to the experiment.

More significantly, simulation was required to link the observed oscillation damping to the experimental quantities of interest. For unmagnetized or weakly magnetized plasmas, the simulations

had good convergence and applicability to the experiments. As discussed in chapter 3 below, for magnetized plasmas the situation is more challenging and the applicability of the simulations an open question.

In the research in this thesis (which builds on the work described in John Guthrie's thesis [24]), we use a different approach to study electron-ion collisions. We applied an off-resonance radio frequency (RF) electric field pulse to induce heating in the UNP, focusing on the measurement of its RF heating rate. The application of this off-resonance RF field triggers electron oscillations. While the electrons oscillate with respect to the ions, momentum and energy transfer occurs via electron-ion collisions. Electrons will eventually gain energy and heat up. Thus, our primary focus centers on measuring the RF heating rate, a parameter also closely related to the electron-ion collision rate.

Several improvements were made beyond the work described in John Guthrie's thesis [24] as part of the work in this thesis. The number and range of magnetic fields where measurements were made were increased substantially. New simulation techniques were developed and tested. A systematic effect associated with insufficient thermal equilibration of the electrons after heating was identified, characterized, and minimized. A new technique for calibrating stray electric fields and calibrating the electrons' photoionization energy was developed. The simulation techniques are described in chapter 3 and the other improvements in chapter 6.

The experimental sequence and apparatus, however, is largely unchanged from the work in that thesis. Rather than repeating the material from that work, a general description is presented with details for new contributions. In this basic plasma physics chapter, UNP formation and the experimental apparatus are described. The RF measurement details are contained in chapter 6.

UNPs in our apparatus are initially made from preparing an ultracold neutral gas. We first laser cool ^{85}Rb to as low as 100 μK. These ultracold atoms are spatially confined using a magneto-optical trap (MOT): a standard laser cooling and trapping technique. [28] At the end of the MOT sequence, the spatial extent of the atom cloud in the MOT is approximately 1mm and there are about 40x10^6 atoms in the MOT. The ultracold atoms are then transferred to the plasma region

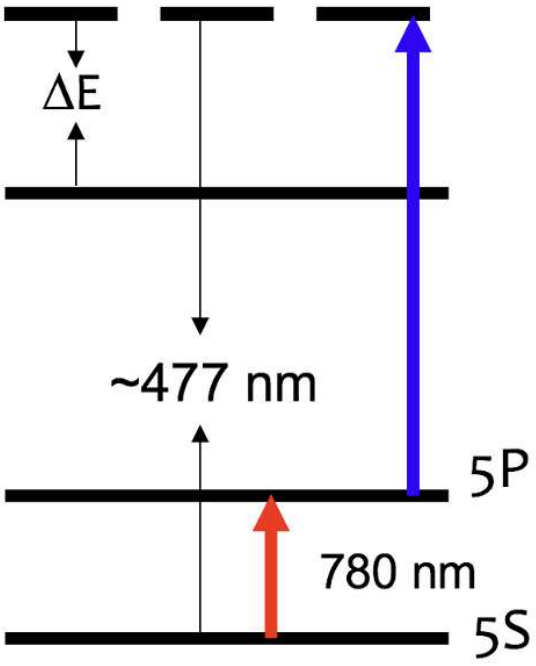

Figure 2.5: This figure shows the two stage photoionization process of an rubidium atom. The red laser with a 780nm wavelength excites the electrons from the ground state to the excited state. Then the tunable blue laser ionizes the electron. The electron initial energy is denoted as ΔE

within the vacuum system. This is accomplished by loading the atoms into a purely magnetic trap formed by increasing the current through the anti-Helmholz (AH) coils that are used for the MOT, from 30A to 120A [29]. This forms an AH magnetic trap with a magnetic field gradient in the strong direction of 66 $\frac{G}{cm}$. The strong direction is oriented vertically. The AH coils are then physically transported by a motorized linear translation stage approximately one meter to what we call the plasma science region of the apparatus.

In this region, we have the capability to illuminate the atoms with laser beams to ionize the atoms. First, we turn off the AH coils to release the atoms from the magnetic trap. At the same time, we apply an external magnetic field with a selected amplitude between 10G and 140G. The atoms are subjected to laser light at 780nm tuned to the $5S_{\frac{1}{2}}$ F=2 to $5P_{\frac{3}{2}}$ F'=3 transition to optically pump all the atoms into the upper hyperfine state. We ionize the atoms via a two-step photoionization process. In the first step, a 780nm photon from a diode laser excites the atoms from the $5S_{\frac{1}{2}}$ F=3 state to the $5P_{\frac{3}{2}}$ F'=4 state. At high magnetic fields the different Zeeman transitions are resolved. This 780nm laser is tuned to the $m_F = -3$ to $m_F = -4$ magnetic sublevels of the two states. Since only atoms in the $m_F = -3$ sublevel will be excited, the ultimate number of ions and electrons in the UNP is reduced, but the number is sufficient for our purposes. The intensity of the 780nm is adjusted to control the number and therefore density of electrons and ions in the UNP. Following the 780nm excitation, a $1ns$ blue laser pulse (478nm) goes through the atom cloud and ionizes the electrons. Notably, the initial temperature of the electrons can be adjusted by modifying the wavelength of the blue laser.

Right after ionization, electrons lack confinement since the average space charge in the UNP region is initially neutral. Due to their initial kinetic energy, electrons can escape and leave the ion cloud. Subsequently, the remaining ion cloud creates a trapping potential, which in turn captures the remaining electrons, thus forming an UNP. The ions are not confined and eventually expand [2], but all measurements and simulations presented in this thesis occur before that expansion is significant. The expansion limits the UNP lifetime to about 100 μs for our conditions. The

measurements we make are completed with 20 μs after UNP formation, and the UNP will have expanded less than 10% at that time.

As electrons escape from the UNP, electric and magnetic fields guide them to a microchannel plate (MCP) where they are detected. The MCP signal is the main experimental diagnostic that we use. Experiments are designed to create a change in the UNP that leads to a change in the electron escape rate. Observed changes to the electron escape rate are related back to the plasma properties of interest that are being measured. The details of the experimental method used for RF heating measurements is presented in chapter 6.

Surrounding the UNP region are coils outside the vacuum chamber and conducting surfaces inside the vacuum chamber that allow the application of diverse forms of electric and magnetic fields. For clarity and consistency throughout this thesis, it's important to define our directional references. In this thesis, I will use the term 'upstream' to refer to the side of the system facing the MOT, while 'downstream' indicates the side oriented toward the MCP. Outside the chamber right at the plasma region, the stainless steel chamber is wrapped around by 120 turns of wire. This coil is providing the necessary magnetic field for the magnetization of the plasma, as illustrated in Figure 2.6(a). Within the chamber, there is a copper disk with a central hole. This disk is connected to a Tektronix AFG3012 100MHz function generator, capable of providing both RF and delta function like 'kick' electric fields. The disk is positioned several millimeters away from the plasma region in the upstream direction. A photograph of the copper disk is shown in Figure 2.6(b). Located on the downstream side of the plasma region, there is a wire grid connected to an Agilent 33250A 80MHz function generator. This grid is designed to generate DC electric fields, help the extraction of electrons and guide them towards the MCP (Figure 2.6(c)).

On the simulation side, we use molecular dynamic (MD) and Monte Carlo(MC) simulations to study the electron-ion collision rate. MD simulations simulate each particle trajectory based on the forces from all other particles and external fields and it includes all classical particle collision physics. In contrast MC simulation use a collision operator to simulate collisions happening between electrons and ions and does not treat the ions as point particles but rather uses a smoothed

Figure 2.6: pictures of magnetic coil(a), copper disk(b) and extraction grid(c) [24]

ion density for the average forces from the ion component. As previously discussed, collisional damping is related to electron-ion collisions. Consequently, we undertake simulations of the collisional damping process employing both MD and MC methods, comparing the two techniques for both the overall collisional damping rate and individual collision characteristics. Furthermore, we performed MD simulations to replicate the application of an off-resonance RF field to the UNP. In principle, this enables us to measure the resulting RF heating rate and make comparisons to our experimental results. In practice, getting sufficient convergence in these simulations in a reasonable amount of time for magnetized plasmas proved impractical and so the information that we could obtain was limited, although still useful. More details about the simulations are supplied in the following chapter.

Chapter 3

Monte Carlo and Molecular Dynamics Simulation Studies of UNPs

3.1 Chapter introduction

Plasma evolution studies have to deal with numerous pairwise Coulomb interactions between particles along with any applied external fields. Although the interactions are electric and magnetic forces which have simple expressions, the long-range nature of the Coulomb force leads to complicated physics that often defies simple description. The purpose of our simulations is to solve for each individual plasma particle's position and velocity numerically as a function of time given initial conditions and the fields applied. Plasma properties such as heating rates, damping rates, and collision rates can be obtained from these simulations.

The two types of simulations, Monte Carlo (MC) and molecular dynamics (MD) are presented at the end of the previous chapter. Each simulation type has its own advantages and disadvantages and usefulness in deriving plasma properties of interest.

At the beginning of this chapter, I would like to start with a description of the computing algorithm for MD simulations. The i^{th} particle's position vector $\vec{r}_i$ at time t can be written as:

$$\vec{r}_i = \int \vec{v}_i dt + \vec{r}_{i0} \tag{3.1}$$

Where $\vec{r}_{i0}$ is the i^{th} particle initial position, $\vec{v}_i$ is the particle velocity vector, and it can be written as:

$$\vec{v}_i = \int \vec{a}_i dt + \vec{a}_{i0} \tag{3.2}$$

$\vec{v}_{i0}$ is the i^{th} particle initial velocity, $\vec{a}_i$ is the particle acceleration vector. It can be derived from calculating the total force exerting on this particle:

$$\vec{F}_i = m_i\vec{a}_i = \sum_{j,i\neq j}^{n} \frac{kq_iq_j\vec{r}_{ij}}{|\vec{r}_{ij}|^3} + q_i\vec{E} + q_i\vec{v}_i \times \vec{B} \tag{3.3}$$

Where $\sum_{j,i\neq j}^{n} \frac{kq_iq_j\vec{r}_{ij}}{|\vec{r}_{ij}|^3}$ is the Coulomb force from all the other particles in the plasma and the $q_i\vec{E} + q_i\vec{v}_i \times \vec{B}$ term is the Lorentz force. $\vec{r}_{ij} = \vec{r}_i - \vec{r}_j$ is the position vector pointing from particle j to particle i. $k = \frac{1}{4\pi\epsilon_0}$ is the Coulomb constant

To solve these equations numerically, the integration is performed using a standard technique: either Leapfrog integration [30] or Runge-Kutta integration [31] was used. Given the initial conditions $\vec{r}_{i0}$ and $\vec{v}_{i0}$, we can solve for $\vec{r}_{i1}$ and $\vec{v}_{i1}$ at the next time increment dt. dt and the integration method used determine the accuracy of the results. UNPs' lifetime is on the order of 100 μS. However, in our work we care about the plasma on shorter timescales, which are usually on the order of a few μs. For our conditions, dt is set between 10^{-14} to 10^{-10} seconds.

With this timestep, we can estimate how many operations need to be done in order to finish a 2 μs simulation with 10^4 electrons and 10^4ions. Suppose for simplicity that the Euler method is used: $\vec{r}_{i(n+1)} = \vec{v}_{in}dt + \vec{r}_i$, and the time step dt is $10^{-14}s$. In each time step, the most time-consuming operation is to calculate the pair-pair forces between particles. It has $20000^2/2 = 2 \times 10^8$ pair in total. Each has three direction x, y, and z. So, to finish a 2 microsecond simulation, it needs at least $2 \times 10^8 \times 3 \times 2 \times 10^{-6}/1 \times 10^{-14} \approx 10^{17}$operations. A modern CPU can do a binary add operation at the speed of 0.3 ns per operation and these operations are done in series in a CPU. Leaving out the data copying time for each operation between cache and memory, and assuming the CPU has 8 cores, to finish this computation will cost $5x10^6$ seconds, which is almost 2 months. In fact, the real computation time will be far more than 2 months because of the data transfer latency in each operation. In contrast, GPU (graphics processing unit) computation enables parallel computation that has a huge advantages when simulating this scenario. First, pair-pair force calculation can be done in parallel: the outcome of one force won't affect the results

of other forces. One GPU contains thousands of cores while most CPUs have less than 10 cores. Second the force computation is almost algebraic. It doesn't have transcendental or complex logic computation for which CPUs are much faster. For algebraic operations, single core performance for GPUs is just slightly slower than CPUs these days. A reduction in computing time of a factor of 1000 is achievable through using the proper hardware.

There are numerical techniques that reduce the $O(N^2)$ scaling of the problem to an $O(N)$ scaling such as fast-multipole methods [32] or FFT-based mesh methods [33]. These techniques carry a lot of computational overhead and so only gain advantage for a large number of particles (>10^4) and create complications when modeling plasmas that aren't approximated as infinite uniform density plasmas and/or have a large variation in average density. Convergence considerations are harder to evaluate and choices need to be made about numerical factors that define e.g. what forces should be calculated using short-range techniques and what forces should not be calculated that way. In principle these $O(N)$ techniques are superior to our hardware solultion, but we are willing to sacrifice some performance for ease-of-use.

An Nvidia graphics card with its parallel computing platform called CUDA is a very common choice for parallel computation simulations. CUDA has been developed for decades and become the most mature and convenient platform when facing a MD simulation problem. Kernel function is the key of realizing parallel computation in CUDA C++. Below is a simple example of how to write a kernel function in CUDA C++.

```
1  #include <iostream>
2  using namespace std;
3
4  __global__ void drfull(double *x,double *y,double *z,double *vx,double
   ↪  *vy,double *vz,double dt,int N){
5      int i = (blockIdx.x * blockDim.x) + threadIdx.x;  //thread indices,
   ↪  don't need to change this line
6      while(i<N){
7          x[i]=vx[i]*dt;
```

```
8           y[i]=vy[i]*dt;
9           z[i]=vz[i]*dt;
10          i += blockDim.x * gridDim.x; //while loop make sure all indices
    ↪  is distributed to GPU threads
11      }
12  }  //a kernel that update the x,y,z vector
13
14  int main(void){
15      double N=10000;
16      double dt=1.e-14;
17
18      double vx[N];
19      double vy[N];
20      double vz[N];
21      for(int i=0;i<N;i++){
22          vx[i]=1;
23          vy[i]=1;
24          vz[i]=1;
25      }
26
27      double *vxgpu;
28      double *vygpu;
29      double *vzgpu;
30
31      cudaMalloc((void**)&vxgpu,sizeof(double)*N);          //allocate GPU
    ↪  memory
32      cudaMalloc((void**)&vygpu,sizeof(double)*N);
33      cudaMalloc((void**)&vzgpu,sizeof(double)*N);
34      cudaMemcpy(vxgpu,vx,sizeof(double)*N,cudaMemcpyHostToDevice);
    ↪  //copy vectors to GPU
35      cudaMemcpy(vygpu,vy,sizeof(double)*N,cudaMemcpyHostToDevice);
36      cudaMemcpy(vzgpu,vz,sizeof(double)*N,cudaMemcpyHostToDevice);
```

```
37
38      double *dx0;
39      double *dy0;
40      double *dz0;
41      cudaMalloc((void**)&dx0,sizeof(double)*N);
42      cudaMalloc((void**)&dy0,sizeof(double)*N);
43      cudaMalloc((void**)&dz0,sizeof(double)*N);
44
45      int threadperblock=512;
46      int blockpergrid1D=64;
47
48      drfull<<<blockpergrid1D,threadperblock>>>(
    ↪   dx0,dy0,dz0,vxgpu,vygpu,vzgpu,dt,N);
49
50      //The drfull kernel is launched with the specified number of blocks
    ↪   ('blockpergrid1D') and threads per block ('threadperblock').
51
52      cudaDeviceSynchronize();   //make sure all GPU computation is
    ↪   completed before proceeding
53
54      cudaFree(dx0);  //Memory on the GPU is freed using cudaFree.
55      cudaFree(dy0);
56      cudaFree(dz0);
57      cudaFree(vxgpu);
58      cudaFree(vygpu);
59      cudaFree(vzgpu);
60
61      return 0;
62  }
```

This simple code calculates the position array dx0, dy0, dz0, based on the given velocities (vx, vy, vz) and the time dt in parallel. Similar to how a 'for' loop operates by CPU, a kernel is the

GPU way of manipulating all variables at once in vectors. A basic CUDA parallel computation program usually contains four parts. In the above code as an example, line 4 to line 10 is the kernel function. Line 15 to line 43 defines variables, allocates GPU memory and copies variables from CPU to GPU RAM. Line 48 is the kernel execution and line 54 to 59 is the memory clean up.

The drfull kernel function is defined to update the x, y, and z vectors. It takes several arrays (x, y, z, vx, vy, vz) and a time step dt as input. The kernel uses the blockIdx.x, blockDim.x, threadIdx.x, and gridDim.x variables to determine the index of the element to be processed by each thread. Each thread updates the corresponding element of x, y, and z by multiplying the corresponding elements of vx, vy, and vz by dt. Each kernel has a fixed form staring with __global__void kernalname (variables); Unlike functions, kernels can not return anything. Computation completes when the correct variables are passed to the kernels.

Three pointers (vxgpu, vygpu, vzgpu) are declared to store the GPU memory addresses for the corresponding arrays. Memory is allocated on the GPU for the arrays using cudaMalloc, and the data is copied from the host (CPU) to the GPU using cudaMemcpy.

3.2 Pair force computing kernel

The key part of the MD simulation is to find an efficient way to compute the pair forces, not only computationally efficient but also but also in a manner that is RAM-saving. The most intuitive way is to calculate the pair force matrix , the element $r_{ij} = |\vec{r_i} - \vec{r_j}|$ represents the distance between the i^{th} and the j^{th} particle, and the force is a function of r_{ij}. However, when particle numbers bumped up to above 20000, the pair distance data need more than 20 GB GPU RAM to save and memory usage is O(N^2) in this problem. To solve this memory issue, the force F_{ij} is computed in parallel for i but in series for j. Specifically, for a given j, F_{0j},F_{1j}, ..., F_{Nj} are computed simultaneously by different CUDA cores. For a specific ith CUDA core, F_{i0}, F_{i1}, ..., F_{iN} are computed sequentially. During this process, each force F_{ij} is added to the total force exerted on the ith particle, denoted as F_i, using the operation $F_i+ = F_{ij}$. As a result, the value of F_{ij} overwrites the previous force

values, effectively conserving a significant amount of memory space. Below is the pair force compute kernel with some notations.

```
__global__ void dv(double *dvx,double *dvy,double *dvz,double *x,double *y,double *z,double *vx,double *vy,int Ne,int N,double alphasquare,double Ez,double Bz,double dt){
    int i = (blockIdx.x * blockDim.x) + threadIdx.x;
    while(i<N) {
        double xi;
        double yi;
        double zi;
        double Fxi;
        double Fyi;
        double Fzi;
        double dr;
        double dx;
        double dy;
        double dz;
        double tempFxi;
        double tempFyi;
        double tempFzi;
        xi=x[i];
        yi=y[i];
        zi=z[i];
        tempFxi=0;
        tempFyi=0;
        tempFzi=0;

        for (int j = 0; j < N; j++){
```

```
25              dx=xi-x[j];
26              dy=yi-y[j];
27              dz=zi-z[j];
28              dr=dx*dx+dy*dy+dz*dz+alphasquare;
29              dr=1/sqrt(dr);
30              dr=dr*dr*dr; // calculates 1/r^3 alphasquare is the
    ↪  softening parameter, other forms of potential can be
    ↪  replaced here
31              Fxi=dx*dr;    //(xi-xj)/r^3
32              Fyi=dy*dr;
33              Fzi=dz*dr;
34              if(j<Ne){
35                  tempFxi+=Fxi;
36                  tempFyi+=Fyi;
37                  tempFzi+=Fzi;
38              }  //sum (ri-rj)/r^3 ignore the ith particle charge
    ↪  sign now
39              else{
40                  tempFxi-=Fxi;
41                  tempFyi-=Fyi;
42                  tempFzi-=Fzi;
43              }  //sign change when j>Ne
44          }
45          if(i<Ne){
46
    ↪  dvx[i]=(tempFxi*253.26384634-vy[i]*Bz*1.7588200878472e11)*dt;
47
    ↪  dvy[i]=(tempFyi*253.26384634+vx[i]*Bz*1.7588200878472e11)*dt;
```

```
48
    dvz[i]=(tempFzi*253.26384634726-Ez*1.7588200878472e11)*dt;
49          }
50          //253.26384634726=k*q*q/me,1.7588200878472e11=q/me
51          else{
52
    dvx[i]=(-tempFxi*1.6240456041e-3+vy[i]*Bz*1.1278372627e6)*dt;
53
    dvy[i]=(-tempFyi*1.6240456041e-3-vx[i]*Bz*1.1278372627e6)*dt;
54
    dvz[i]=(-tempFzi*1.6240456041735e-3+Ez*1.1278372627587e6)*dt;
55          }
56          //1.6240456041735e-3=k*q*q/mi,1.1278372627587e6=q/mi
57          i += blockDim.x * gridDim.x;
58      }
59  }
```

3.3 Discussions on the precision of MD simulation

When an electron approaches an ion the electron velocity becomes high and as a result the accuracy of each numerical integration timestep decreases and errors accumulate. Consequently, the Coulomb potential is modified to $\frac{k}{\sqrt{r^2+\alpha^2}}$ where $k = \frac{1}{4\pi\epsilon_0}$ is the coulomb constant. A softening parameter α is implemented to prevent division by zero in the $1/r^3$ term of the Coulomb potential as well as to mitigate numerical errors that arise due to electrons that become deeply bound to ions (i.e. Rydberg atoms that are sufficiently tighlty bound) [34]. The choice of α depends on the integration timestep. The lower the timestep the lower the α, as timestep for an infinitely small α would become zero. In practice, α is selected to be around 1% of interparticle spacing. While changing α influences small-impact-parameter collisions and potentially Rydberg atom energy

distributions, for many of our plasma conditions the distortions from adding this α parameter are expected to be small enough to be ignorable and so α is safe to implement. When checking, we didn't find influences on the results of interest when altering α for unmagnetized electrons. When magnetic fields were added, gaining convergence as a function of α for parameters of interest was not achieved beyond the $\sim$10% level.

In addition to the softening parameter, the precision of the numerical values used in the molecular dynamics (MD) simulation also affects the accuracy of the results. To investigate this, we conducted a simulation with a plasma cloud consisting of $0.75x10^4$ electrons and 10^4ions. The initial conditions were kept consistent, and the simulation was run using variables in both single precision and double precision. We monitored the position of a specific electron and plotted the position (x) versus time in Figure 3.1. With an integration timestep of 0.01 ns, the data presented in the plot clearly demonstrate that small deviations begin to accumulate when the evolution time exceeds 0.2 μs. These results were consistent across other electron trajectories as well. When looking at macroscopic quantities (such as the total energy in the system or the velocity distribution function) or making comparisons, these deviations often will average out and make no contribution to the final results. Even so, it indicates more careful treatment needs to be considered if the simulation is long enough and the "microphysics" of properties of things such as collisions may not average out for the quantities of interest.

The choice of timestep and numerical method plays a crucial role in balancing computation time, memory usage, and precision in molecular dynamics (MD) simulations. While a shorter timestep can increase precision, it cannot be arbitrarily small due to finite digit representation and the limitations of computational resources. We performed another simulation with $0.75x10^4$ electrons and 10^4 ions evolving for 2 μs. When using a timestep of 1 ps, the computation time is approximately 3 days. Therefore, it becomes necessary to find an efficient approach that maintains precision without costing too much computation time. To address this, we kept the initial conditions consistent and explored different combinations of timestep and numerical methods. Specifically, we perform the simulation with a timestep of 0.1 picoseconds using the Boris algorithm.

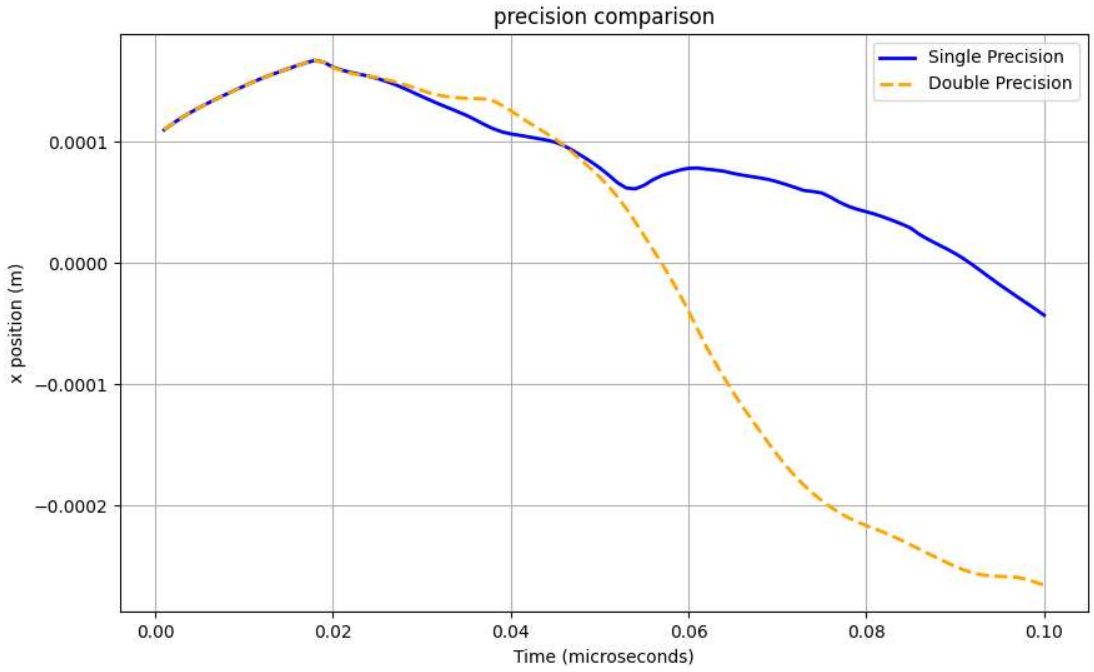

Figure 3.1: An example illustrating the precision comparison results of MD simulations. The blue solid line represents a simulation conducted with all variables in the MD code being in single precision (8 digits), while the orange dashed line corresponds to a simulation using the exact same initial conditions but with all variables in double precision (16 digits). In both simulations, the time step used is 0.01 ns.

Figure Figure 3.2 displays an electron position in the x direction over time under the influence of magnetic and electric fields. The figure reveals that the fourth-order Runge-Kutta integrator consistently provides consistent results, regardless of the chosen timestep. On the other hand, the second-order Boris algorithm starts to deviate before reaching 0.01 μs. More importantly, the fourth-order Runge-Kutta method performs better with a timestep of 0.1 ps compared to the Boris algorithm with a timestep of 0.01 ps, despite the latter requiring five times more computation time.

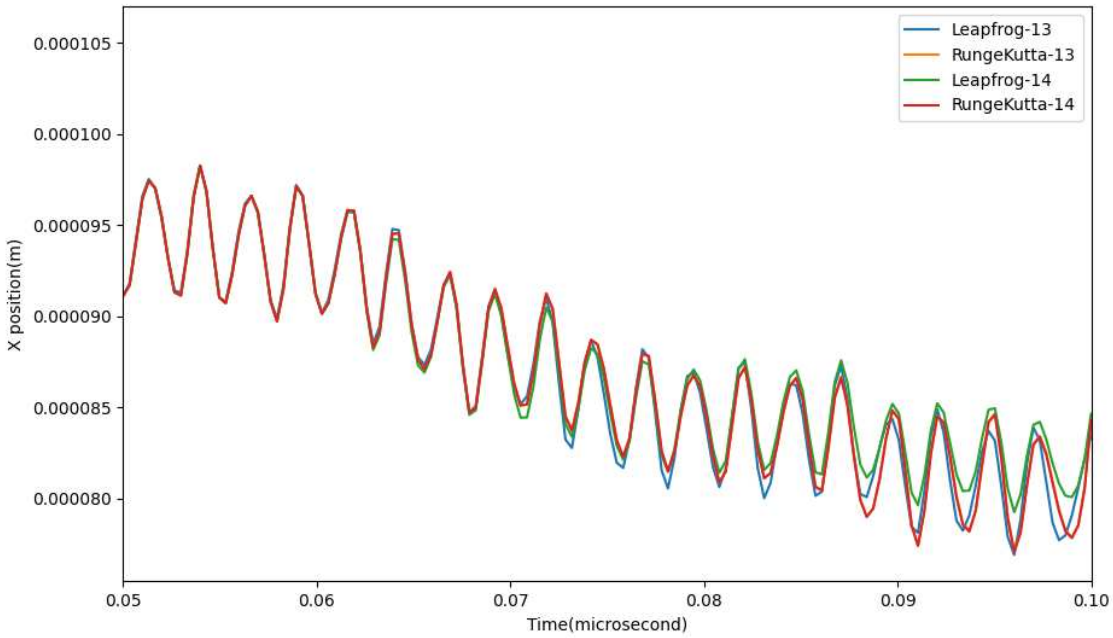

Figure 3.2: This is an example of an MD simulation that compares the evolution of one electron's x-coordinate over time using different integration methods under the influence of a magnetic field. In the plot, Leapfrog/RungeKutta is the name of the integrator. The Boris method is the Leapfrog method with an adaptation to account for external magnetic fields. 13 or 14 represents the time step, which is either 10^{-13} or 10^{-14} seconds. All four conditions start with the same initial conditions, and the plot displays the trajectory starting from t=0.05 microseconds. The orange trace (RungeKutta-13) closely aligns with the red trace (RungeKutta-14), while the Leapfrog method gradually deviates.

MD modeling of RF heating in UNPs will be discussed in chapter 6 in the context of the measurements that are described there. Satisfactory convergence was not obtained for the week-long runtimes that we were willing to use.

3.4 Monte Carlo(MC) simulation

Electron dynamics happen much faster than ion because of electrons' smaller mass, and so when studying electron dynamics in a shorter time scale, ions barely move. MC simulation includes the space charge of the ions as a smooth, steady-state background potential. Electron-electron collisions are preserved, and electron-ion collisions are modeled by a random collision operator: electrons are randomly deflected based on a probability which relates to velocity and the Debye screening length (λ_D). MC simulation significantly shortens the computation time compared to the MD as usually electrons are less than half of the total particle number. Because the artificial collision operator was used, MC simulation is useful for studying electron-ion collisions in a macroscopic way that can test different theory predictions. It can also be used to test assumptions made in our measurements. For instance, if there is a quantity that we think should or should not be affected by the electron-ion collision rate, that expectation can be tested in the MC code by turning the electron-ion collisions off in the simulation.

More subtly, the MD simulations contain all of the expected relevant physics of the UNPs and that can make it hard to isolate particular effects. The MC code allows for deliberate changes in electron-ion interactions that makes determining the impact of different plasma properties easier to characterize.

We have used different types of collision operators as described in chapter 5. The most common is to treat all electron-ion collisions as scattering via Rutherford scattering. A maximum classical impact parameter $b_{\max}$that scales with λ_D is set and a collision probability, $n\pi b_{\max}^2 v$ for each electron is calculated for each timestep and compared to a random number. If the collision occurs, a random impact parameter is selected and the electron velocity deflected an amount determined

via Rutherford scattering. This is suitable for unmagnetized plasmas. If used with magnetizied plasmas, only an approximate treatment of collisions is reasonable to expect.

These types of collision operator is developed under the assumption that all collisions are binary. In reality, for UNPs that are moderately and strongly coupled, the presence of many-body collision physics becomes significant. By comparing details of MD simulation and MC simulation results we are able to draw the conclusion that the binary collision picture and MC simulation fail to characterize the many body physics, which will be discussed in chapter 5.

The use of MC and MD simulations will be noted in the following chapters where relevant.

Chapter 4

DC electric field heating

The material in this chapter closely follows my first-author publication on this topic [12]. I have made modifications between that publication and the material published here.

Some of the most potentially interesting UNP experiments require as low an electron temperature as can be achieved. For instance, plasma strong coupling effects [19] and three-body recombination in plasmas [9, 10] require low electron temperatures. Further, the importance and size of these effects increase with decreasing temperature. So, to explore the most interesting parameters, it is crucial to reach extremely low temperatures. Also, knowing what the cold temperature limit is useful, as that limitation determines the extent to which low-temperature-dependent effects can be studied. To determine the lower boundary of the electron temperature, it is important to investigate the mechanisms responsible for both heating and cooling in UNPs. Various heating and cooling mechanisms have been reported including: three-body recombination [9, 10], continuum lowering [35], disorder-induced heating [20, 36, 37], UNP expansion [8], and electron evaporation [38]. In this chapter, we use MD simulations to study an additional heating mechanism that affects UNP electrons. All of these studies are for unmagnetized plasmas. This heating phenomenon occurs when a DC electric field is applied during the formation of the UNP. This electric-field induced heating can easily be the primary mechanism responsible for heating electrons in low-density UNPs, even when mild electric fields are applied.

4.1 Heating mechanism and theory estimate

The reason behind the heating of electrons by a DC electric field is as follows: Right after photoionization, the plasma possesses a neutral overall space charge. When a DC electric field is present, it accelerates the electrons, causing an increase in their kinetic energy. This acceleration process eventually stops due to the development of an internal electric field, which opposes the applied field, when the electrons are displaced. Depending on the strength of the applied electric

field, oscillations may occur. In any case, the final equilibrium center-of-mass position of the electrons differs from their initial configuration. This leads to a change in potential energy for the electrons. The kinetic energy that compensates for this potential energy change ultimately transforms into heat, resulting in an increase in electron temperature compared to when no applied electric field is present.

The heat imparted by the electric field can be estimated using energy conservation. Several simplifying approximations can be made as part of a straightforward estimation: no electrons are lost from the UNP, the UNP has uniform density, and the UNP is spherically symmetric. Under these conditions, the change in potential energy equals the displacement of the electrons caused by the external field multiplied by the force due to the electric field. The resulting temperature increase can be calculated using the fact the average kinetic energy is equal to $\frac{3}{2}\ k_B T$ where k_B is the Boltzmann's constant and T is the electron temperature. For a plasma with a density of n and an applied external field of F, the temperature rise imparted can be expressed as $\frac{2\epsilon_0 F^2}{n k_B}$ [12]. This estimate indicates that the heating caused by the DC electric field is proportional to the square of the applied electric field magnitude and inversely proportional to the electron density.

In practice, UNPs often exhibit a Gaussian distribution rather than uniform density. Additionally, electrons can escape from the plasma under the influence of electric fields, carrying kinetic energy away. This complicates the UNP internal electric field environment and leads to deviations from the idealized heating rate relationship described earlier. Furthermore, various heating and cooling mechanisms may occur simultaneously at the same time, complicating the heating rate analysis even further. To quantify the heating induced by an applied DC electric field in an UNP, we employ MD simulations in order to theoretically model the UNP. MD simulations include all classical particle dynamics, allowing us to account for various heating and cooling mechanisms. Additionally, MD simulations enable us to establish initial conditions consisting of Gaussian distributions, track electron loss from the system, and straightforwardly introduce a DC field into the model.

4.2 Methodology

Our simulation consists of two separate stages. During the first stage, we model the ionization of ultracold atoms, resulting in the formation of free electrons and ions. In the second stage, we let UNP evolve toward an equilibrium state. The ultracold atoms that undergo ionization are initially distributed randomly within a Gaussian density distribution with density $n(r) = n_0 e^{-\frac{r^2}{2\sigma^2}}$ at distance r from the center of the UNP and n_0 being the peak density and σ the characteristic spatial size. Then the atoms are ionized: an ion is generated at the atom location and an electron is created $500nm$ away from the ion. This distance is close enough to mimic the electron being ionized while not so close as to introduce numerical problems. Velocities are determined by the photoionization energy through which the initial kinetic energy can be tuned along with energy and momentum conservation laws.

After the ionization, UNP is evolved under a DC electric field throughout the time window we are interested in. The simulation step size in time, dt, is chosen to be small enough so that energy is conserved. Electron temperature are calculated by

$$\sum_{i=1}^{N} \frac{1}{2} m v_i^2 = \frac{3N}{2} k_B T \tag{4.1}$$

where N is the number of free electrons within the UNP. We define electrons as being within the UNP if they are within 4σ of UNP center. Any electrons farther than that are deemed to have escaped and these electrons are not counted in the electron temperature determination. Also, if the potential energy between an electron and its nearest ion energy is below -3.8$k_B T$, [10] these electrons are considered to be part of a deeply bound Rydberg atom and also are not counted when calculating the temperature.

It is worth noting that while the definition of electron temperature provided in the previous paragraph is straightforward when the electrons are in thermal equilibrium, there are some subtleties to consider during the establishment of equilibrium. For instance, this definition includes contributions from electron center-of-mass motion and macroscopic flows as components of the

temperature. Furthermore, defining temperature in a nonequilibrium system is inherently problematic. Once equilibrium is achieved, these concerns are no longer significant, however.

In order to make comparisons between our simulations and experimental conditions relevant to low-density UNPs, we have configured our simulations to match the densities used in prior experimental setups [4]. In our simulations, atom numbers within the range of $3.5\ 7 \times 10^4$ are used, with values of σ that vary from 350 μm to 650 μm. We have chosen initial ionization energies that correspond to initial temperatures spanning from 0.01 K to 20 K. Additionally, we have applied DC electric fields within the range of 0 to 7 V/m. Throughout the evolution of the UNP in our simulations, each electron position and velocity can be extracted at any time and so the temperature and energy can be calculated at any time as well.

During our simulations across various parameters of interest, we conducted multiple runs for each set of conditions. This approach allowed us to study the fluctuations in electron temperature resulting from the random initial placement of atoms.

4.3 Simulation results

Figure 4.1 presents the electron temperature versus time, as calculated for selected initial conditions. In Figure 4.1 (a) and (c), it shows when an external electric field is applied, the electron temperature reaches a near-equilibrium state after a few hundred nanoseconds, following an immediate change upon ionization. This behavior is consistent in all UNPs with the same density but different electric fields, and it is more evident as the field strength increases. Calculations for conditions that include no electric field and 0.01K starting temperature as shown in Figure 4.1 (d) have a less distinct boundary between changing and stable temperature periods when comparing with (b). There is disorder-induced heating at early times in both (b) and (d), but the three-body recombination heating rate is different. In the early stage, the steep rise in temperature presented in case (d) is due to the combined influence of disorder-induced heating and three-body recombination heating. As the temperature increases, the rate of temperature increase stabilizes after the initial rapid changes. The longer-term temperature increase is primarily due to three-body recom-

bination heating. The higher rate of temperature increase at a later time in case (d) compared to case (b) is due to the reduced significance of three-body recombination heating at higher temperature. [8]. In addition, the figures show that the electron temperature after the equilibrium does not stay constant.This is due to the other heating and cooling effects. Data at different initial electron temperature T_i, defined by the value of 2/3 of the excess energy of the simulated ionization photon over threshold, are compared to one another. We choose the time that electron temperature starts to increase steadily and use that corresponding temperature value T_e to compare the initial temperature equilibrium state across different initial conditions. In Figure 4.1 we choose 500 ns as the equilibrium time. For different densities we scale this time inversely with the electron plasma frequency. T_e is a function of T_i, N, σ, and DC electric field amplitude F. For each simulation, we can explore and compare T_e by changing or fixing one or more of these simulation variables.

First, we studied $T_e(T_i, F, N, \sigma)$ as a function of F at two different values of T_i while keeping N and σ constant. The results of these simulations are shown in Figure 4.2. The overall trend of increasing electron temperature with a rise in the applied electric field is apparent from this dataset. In the case of near-threshold conditions for photoionization ($T_i = 0.01K$), an electric field of just a few V/m is sufficient to approximately double the electron temperature compared to the case without an electric field. Therefore, a moderate applied electric field will set limitations on the lowest achievable temperatures, particularly under these low-density conditions.

We can also plot the difference of T_e with or without the DC electric field, i.e. $T_e(T_i, F, N, \sigma) - T_e(T_i, 0, N, \sigma)$ and Figure 4.2 (b) plot the data in this way. The two sets with different T_i show a similar trend, which indicate that the initial ionization energy and the temperature increase resulting from the applied electric field act as additive quantities. We test other sets with different range of densities, initial temperatures and this conclusion also holds true.

In Figure 4.3 the heating due to the applied electric field (i.e. $T_e(T_i, F, N, \sigma) - T_e(T_i, 0, N, \sigma)$) is compared to amount of heating predicted from the simple estimate above, $\frac{2\epsilon_0 F^2}{nk_B}$. The density used in this estimate is the average density, since the density in the Gaussian density distribution is not uniform. The amount of heating is either about the same as or less than the simple estimate.

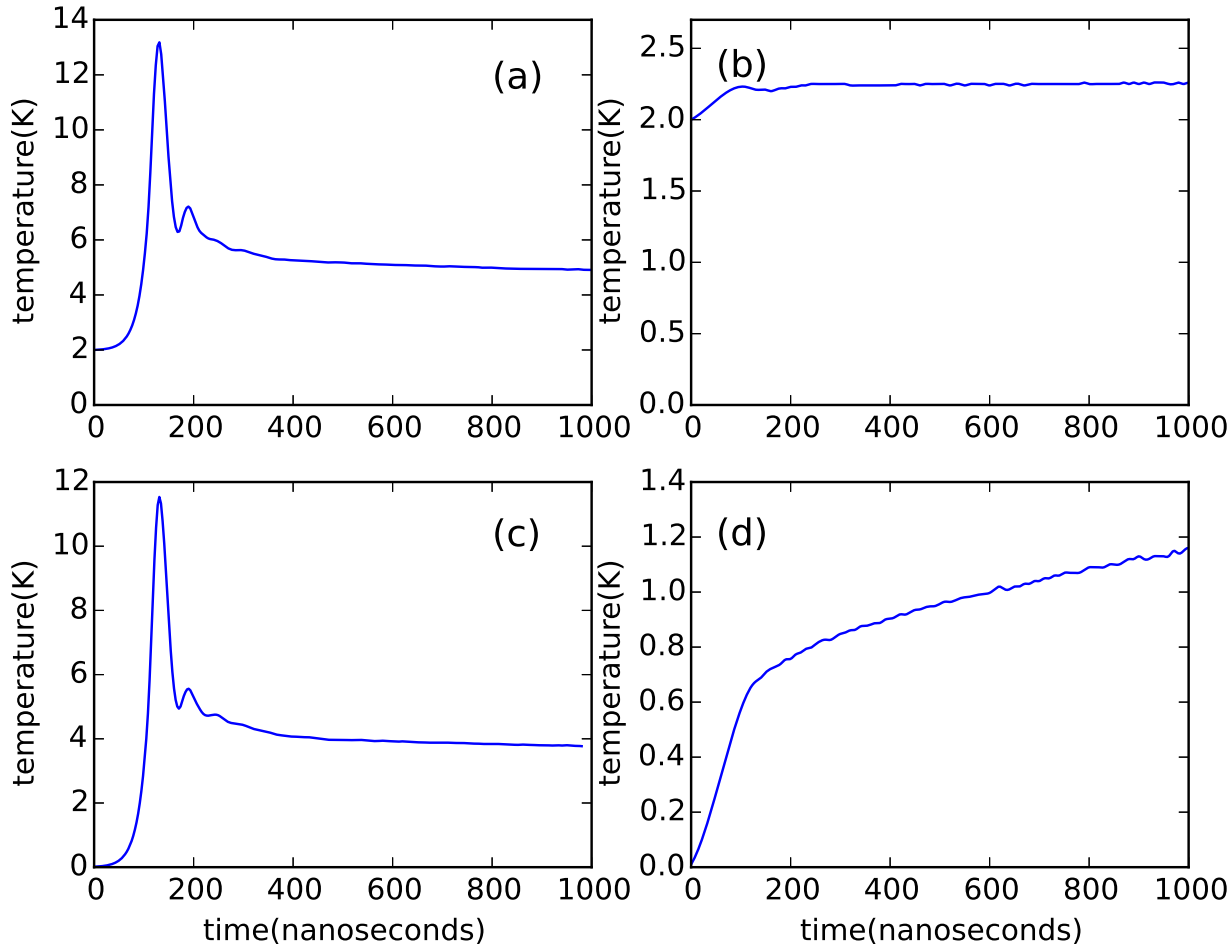

Figure 4.1: Electron equivalent temperature as a function of time after UNP formation. In all cases, the initial atom number N= 70 000 and the plasma σ is 650 μm. The initial electron temperature in (a) is 2 K and a 7 V/m electric field is present. The damped oscillations are due to center-of-mass motion of the electrons in response to the electric field. Figure (b) is the same as (a) without the electric field present. (c) has a 7 V/m electric field but an initial temperature of 0.01 K, while (d) is the same as (c), but with no electric field present.

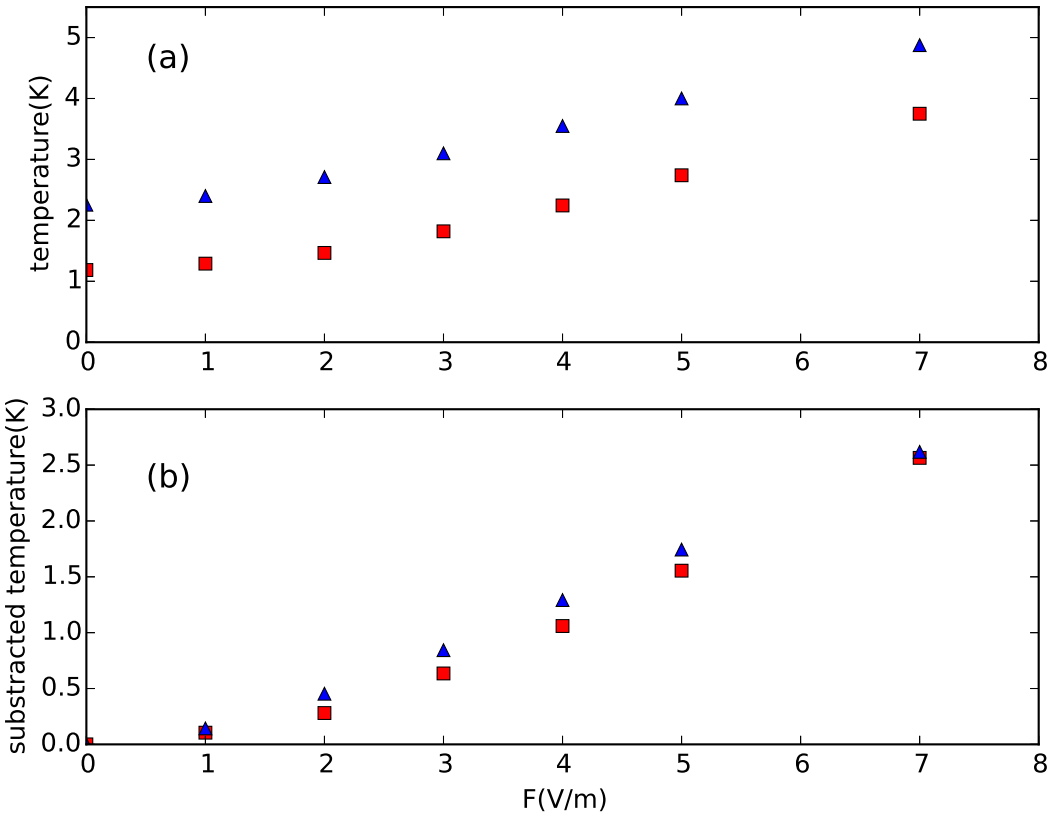

Figure 4.2: Relationship between electron temperature T_e and applied electric field F. Figure (a) shows this relationship for two different initial temperatures T_i for UNPs of the same density. For the blue triangles T_i=2K and for the red squares T_i=0.01K. It is clear that increasing the electric field increases the electron temperature for these parameters. Figure (b) shows the same set of conditions in (a), but with the temperature at F=0 subtracted from all the data points. As that plot illustrates, the amount of temperature change attributable to the applied electric field is very similar for the two conditions shown. This latter fact is a general feature of electric field heating.

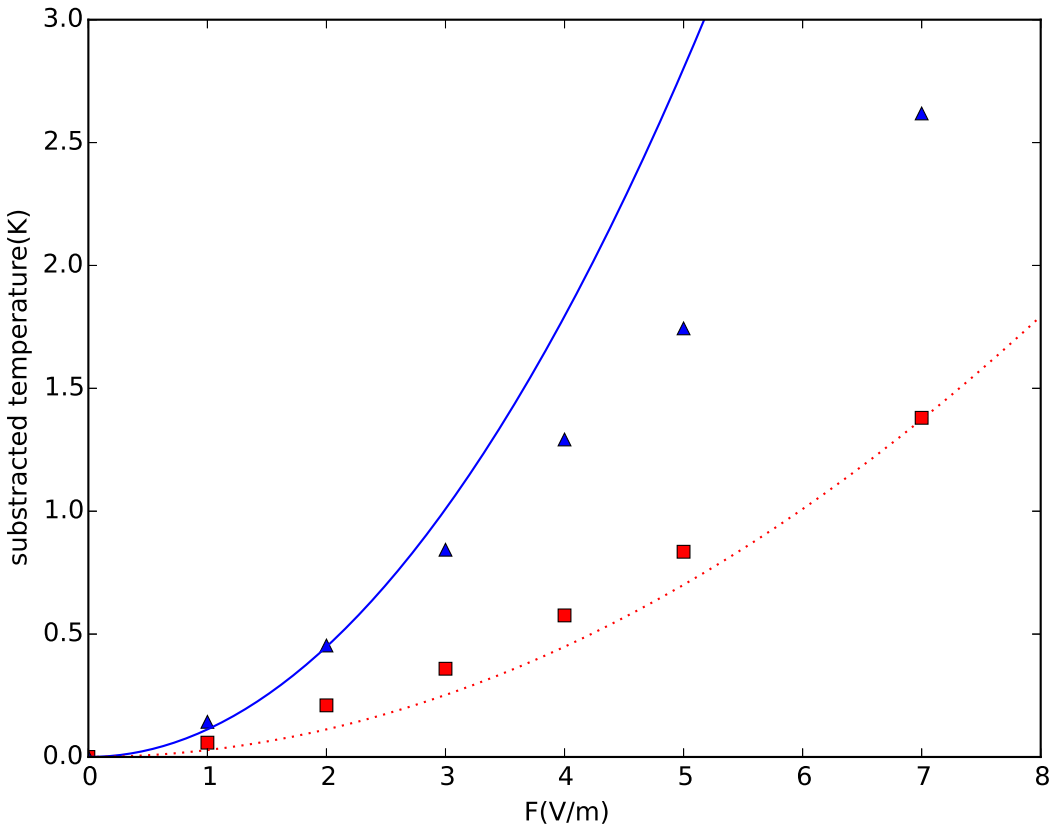

Figure 4.3: The plot shows the temperature change caused by electric field heating under different plasma densities. We keep the initial temperature $T_i = 2K$. The red squares represent 4 times the density as compared with the blue triangle set. The blue solid line represents the trend line based on the simple model prediction with $\sigma = 516\mu m$ and the red dotted line is $\sigma = 325\mu m$. In all cases the initial electron and ion number is 35000.

This is in line with expectations and demonstrates that the simple expression is indeed useful as an estimate.

We performed additional measurements to further explore the UNP parameter space in this general region to investigate trends in the amount of electric field heating. By simultaneously varying N and σ, we observed that the amount of heating was solely a function of the density of the UNP over a range of a factor of 2 in N. In other words, equal density UNPs with different N showed the same amount of heating due to the electric field.

To investigate the dependence on T_i away from the coldest possible temperatures, we ran simulations where we fixed F at 3V/m, N at 35000 and $\sigma = 516\mu m$, while altering T_i over the range of $0.01K$ to $20K$. As Figure 4.4 shows, below about $10K$ there is no clear influence of T_i on

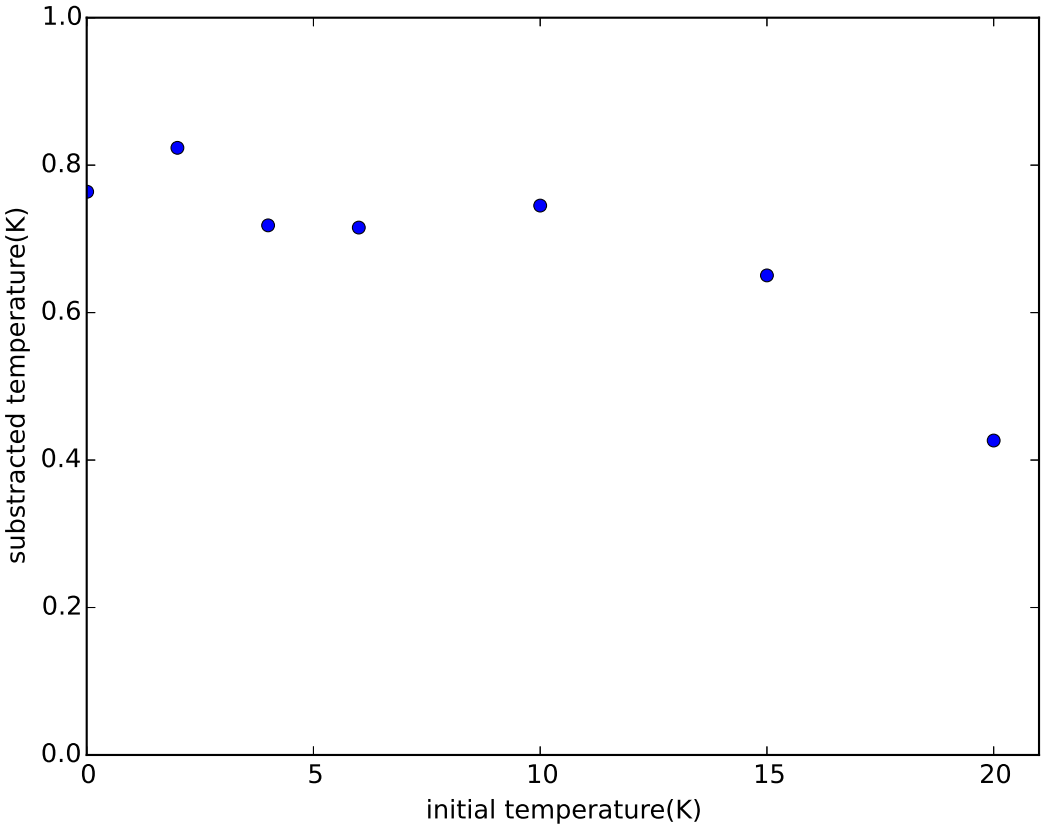

Figure 4.4: The plot shows the temperature change caused by electric field heating under different initial temperature T_i. We keep the electric field at $F = 3V/m$ and density the same for all points shown. As the figure illustrates, in the temperature range we are most interested in(0-5K), the initial ionization energy doesn't affect the electric field heating.

the amount electric field heating, although there is some non-statistical fluctuation in the precise amount of heating under these conditions. From $10K$ to $20K$, the influence of the electric field heating diminishes. Increasing electron kinetic energy increases the electron escape rate, reducing the electric field induced heating in a manner similar to the reduction at higher values of F presented above. For experiments designed to examine strong coupling influences (that therefore operate at the lowest possible temperatures), the heating due to the applied electric field can be identified as independent of initial temperature in that region of interest.

4.4 Conclusion

Using molecular dynamics simulations, we characterize the amount of heating imparted to the electrons in ultracold plasmas by a DC electric field present during the formation of the plasma. We find that for electric fields of a few V/m, significant heating is imparted in lower-density UNPs. This electric field heating is thus relevant to the lowest possible temperatures that can be achieved in ultracold plasmas. An approximate model predicts the heating effect will be proportion to the applied electric field squared and inversely proportional to the UNP density. Our more realistic theoretical description using molecular dynamics simulations at low electron temperatures produces results qualitatively consistent with the simple expression

Taking into account other heating and cooling effects, our simulation results also indicate which effects will have the leading contribution to the electron temperature limitations during the early time of the UNP evolution. This guides considerations for achieving the lowest possible electron temperatures at early times in ultracold plasmas.

Chapter 5

Many body collision study by MD/MC simulation

The material in this chapter closely follows my first-author publication on this topic [13]. I have made modifications between that publication and the material published here.

Experimental studies of electron-ion collision rates in an ultracold neutral plasma (UNP) can be conducted through measuring the rate of electron plasma oscillation damping. For sufficiently cold and dense conditions where strong coupling influences are important, the measured damping rate was faster by over 30% as compared to theoretical expectations [4]. We have conducted a series of numerical simulations to isolate the primary source of this difference. By analyzing the distribution of electron velocity changes due to collisions in an MD simulation, examining the trajectory of electrons with high deflection angle in such simulations, and examining the oscillation damping rate while varying the ratio of two-body to three-body electron-ion collision rates, we have found that the difference is consistent with the effect of many-body collisions that lead to bound electrons. This has implications for other electron-ion collision related transport properties in addition to electron oscillation damping.

5.1 Chapter introduction

In strongly coupled plasmas, the average nearest-neighbor Coulomb potential energy for one or more types of particles is comparable to or exceeds the average kinetic energy of that type of particle. As a result, spatial correlations between plasma particles become significant and many common assumptions used in plasma theory break down. [4, 19, 36, 39, 39–42] In contrast to weakly-coupled plasmas where collisions can be treated as long-range binary scattering events, in strongly-coupled plasmas, many-body effects become increasingly significant. These many-body effects can be treated theoretically through, for instance, using simulations to create phenomenological extensions of binary collision theory into the strongly-coupled regime, [43] or through

creating an effective potential that incorporates many-body effects into inter-particle effective potentials. [44]

However, in strongly-coupled plasmas with electrons and ions (as opposed to one-component plasmas), three- and more-body collisions can result in electrons becoming bound to one or more ions in the plasma, forming a Rydberg atom or an electron bound to a small number of ions. [8, 10, 45, 46] In this chapter, we show that such many-body collisions provide a substantial contribution to the electron average momentum damping rate in plasmas where electron strong coupling is significant. For such strongly coupled plasmas, these many-body-to-bound-state (MBTBS) collisions would be expected to be relevant for other collision-related properties as well, such as stopping power [15, 47], thermalization rates [21], and other transport properties [48].

This investigation of MBTBS collision contributions to the average electron momentum damping rate was motivated by studies of electron oscillation damping in an ultracold neutral plasma (UNP). [4] In that work, electron center-of-mass oscillations were induced by imparting an impulse acceleration to the electrons' velocities. The electrons' center-of-mass then oscillated with respect to the ions until that oscillation damped out due to electron-ion collisions. At the highest electron strong coupling condition measured, there was a gap between the predicted damping rate obtained from multiple theories and the observed damping rate. This gap was also present between a theoretically predicted damping rate and the rate obtained in a molecular dynamics (MD) simulation that agreed with the experimentally measured rate. [4] The ratio of the simulated to predicted damping rate was over 1.3 at the coldest electron temperatures that were considered. To identify the source of the gap, we conducted additional simulation and theoretical numerical studies. The result of those studies is described here.

UNPs are formed through photoionizing cold atoms or molecules from a laser-cooled gas [2] or supersonic beam [49] in a finite-spatial-extent volume. Once the atoms or molecules are photoionized, some electrons escape from the UNP formation region as the average space charge is initially neutral. The more massive ions remain, however, and so a positive space charge develops that is eventually sufficient to confine the remaining electrons, forming the UNP. [2] Both the

ion and electron components quickly come to thermal equilibrium individually, but not with each other. The UNP thus consists of a finite-spatial-extent plasma of electrons and singly-charged ions where the electrons and ions are individually in thermal equilibrium. The electron temperature can be controlled via the photoionization laser wavelength. [2] Eventually, the UNP expands since the ions are not confined, [3] but the timescale of this expansion is long enough that it is insignificant for the work described in this chapter.

Three-body recombination (TBR) to Rydberg atoms plays an important role in UNPs with sufficiently high electron strong coupling parameter Γ. [8, 10] The electron strong coupling parameter is defined as the ratio of the nearest-neighbor Coulomb potential energy to thermal energy such that $\Gamma = \frac{e^2}{4\pi\epsilon_0 a_{\mathrm{WS}}}/k_{\mathrm{B}}T_e$ where e is the fundamental electron charge, ϵ_0 is the dielectric constant of the vacuum, k_{B} is Boltzmann's constant, T_e is the electron temperature, and a_{WS} is the Wigner-Seitz radius equal to $(\frac{3}{4\pi n})^{1/3}$ where n is the electron density. TBR occurs when two electrons collide near an ion and one of the electrons becomes bound, forming an atom that is overwhelmingly likely to be in a highly excited state — a Rydberg atom. Not only are a free ion and free electron lost from the plasma, but the binding energy of the atom is imparted to the non-bound electron involved in the collision and that ultimately results in heating of the electron component of the plasma. [8, 10] In the weakly-coupled limit, the three-body recombination rate scales strongly with electron temperature as $T_e^{-9/2}$. This Rydberg atom formation heating mechanism is predicted to limit the highest achievable values of electron Γ in UNPs [8]. Although these prediction were performed without taking into account the electric field heating mechanism described in the previous chapter.

Rydberg atoms formed in this way, however, do not remain at a fixed binding energy. Electron-Rydberg atom collisions can change the Rydberg atom energy. These collisions can also ionize the Rydberg atom. [10] Electrons thus move in and out of being bound. Moreover, it is possible for electrons to be bound not only to a single ion, but to multiple ions. We found that weakly-bound Rydberg electrons and electrons bound to multiple ions (which are necessarily weakly bound) made the largest many-body contributions to the collision and damping effects described here.

If electrons are moving with an average velocity relative to ions, then electron-ion collisions will result in a damping of that velocity. This occurs because the electron velocities are deflected as a result of the electron-ion collision, reducing the electron center-of-mass speed.

For a bound state electron, the electron's velocity direction changes rapidly as compared to the rate of change of a free electron colliding with other electrons and with ions as it moves around the ion that it is bound to. An electron that becomes bound and then re-ionizes after a sufficiently short period of time will undergo a much larger velocity deflection on average than if it had remained as a free electron. These electrons have a disproportionate impact on the damping of any average electron velocity with respect to the ions. Even if they are only a small fraction of the number of electrons in the plasma, because of comparatively large velocity deflections they can play a significant role in the damping rate.

While the above considerations indicate that MBTBS collisions will have some effect on the average electron momentum damping rate, they do not quantify its contribution. In the rest of this article, numerical simulations are described that demonstrate that for the UNP plasma conditions of Ref. [4], the MBTBS collisions are primarily responsible for the gap between predicted and observed/simulated electron oscillation damping rates.

5.2 Numerical Simulation of Electron Center-of-mass Oscillation Damping in a UNP

Through simulations we calculate the UNP electron center-of-mass oscillation damping rate and other electron properties using two separate techniques to investigate relative contributions from binary and MBTBS electron-ion collisions. In the first, we perform what we term a full molecular dynamics (MD) simulation as described in chapter 3. The full MD simulation has been shown to agree with experimental measurements and should contain all the relevant physics. We call the second technique the Monte Carlo (MC) simulation, again as described in chapter 3. The MC simulation eliminates explicit electron-ion collisions by not representing the ions as point particles. The electron-ion collisions are instead modeled via a random binary collision operator.

Given a theory for electron-ion collisions, the collision operator can be constructed. This allows for a translation of any electron-ion collision theory to any UNP quantity of interest, calculated via the MC simulation. These two techniques will be described in more detail in turn below.

As discussed in section 3.3, the addition of the constant α is necessary to prevent numerical problems that arise from deeply-bound Rydberg atoms that can form in the UNP. The velocity of the electrons in such Rydberg atoms is high, and so for practical timesteps numerical errors accumulate and energy is no longer conserved. "Softening" the Coulomb potential with the α term mitigates this problem. [34] Given the importance of Rydberg atoms in this investigation, the possible distortion of Rydberg populations through the addition of the α term is a concern. Since the simulation step size in time needs to be decreased as α decreases in order to still maintain convergence and energy conservation, our general goal was to use the largest value of α that did not have an effect on the results of the simulations. Investigations into properties such as oscillation damping rates indicated that setting α to be equal to just under 2% of a_{WS} did not distort the simulation quantities of interest. We made sure that we could vary α around this value in a range that spanned about a factor of two without affecting any of the calculated quantities of interest in any detectable way. While the most deeply bound Rydberg population number and binding energy will not be correct with a finite α, those Rydbergs were found not to have a significant contribution to the MBTBS-related effects.

This insensitivity of collision rates to a small enough α value is reasonable given the fact that for our conditions the smallest impact parameter collisions that are most strongly affected by non-zero value of α are still a small fraction of the total collisions that occur and are responsible for only a small fraction of the momentum deflection rate. Thus, the distortions introduced by α do not significantly impact collision-related rates overall.

In the second type of simulation, the MC simulation, the electrons are still treated as point particles, acting through the same modified Coulomb potential for consistency (with α again having no measurable impact). The ions, however, are not represented as point particles. Instead, a continuous charge distribution equal to the average ion density as a function of position is used. This

provides the confining potential for the electrons. Electron-ion collisions are modeled through a random collision operator.

In each timestep, a collision probability is calculated for each electron based on the ion density at the electron's position, the electron's velocity, and the total cross section associated with the collision operator. A random number is generated and compared to the collision probability to determine if a collision has occurred. If one does occur, then the electrons' velocity is deflected randomly according to a distribution function that is generated from the underlying theory of electron-ion collisions that is being used.

A few simplifying assumptions were made in both the full MD and MC simulations. A uniform ion density distribution was used so that the ion density was constant. Aside from convenience, the uniform ion density eliminated collisionless oscillation damping that can occur in non-uniform-density UNPs. [50] The electron number was kept smaller than the ion number to generate confinement. In the full MD simulation, the ion mass was increased to be effectively infinite, as this removed any possible expansion or ion-ion correlation effects. Simulations with the actual ^{85}Rb mass used in the experiment [4] showed these effects to have effects smaller than a few percent, at most, justifying the infinite mass approximation that was made.

Before any properties were extracted from the simulations, they were initialized. For the full MD case, electrons and ions were placed in random locations consistent with a density distribution that was uniform within the plasma. Typically, 16,000 electrons and 30,000 ions were used with an average density of $1 \times 10^{13}\,\mathrm{m}^{-3}$. The simulation was then allowed to run for $0.5\,\mu\mathrm{s}$ in order to let the electrons come to equilibrium. The electron temperature is calculated by assuming $\frac{3}{2}N_e k_\mathrm{B} T_e = \sum_{i=1}^{N_e} \frac{1}{2} m v_i^2$ where m is the electron mass, N_e is the electron number, and v_i is the speed of the i^{th} electron. The electron temperature would increase during the equilibration period owing to disorder-induced-heating [20, 36, 37, 51] and TBR [8–10]. To tune the temperature to our desired value, midway through the equilibration we would rescale all electron velocities to produce the desired total kinetic energy and then we would let the system equilibrate the rest of the time. The MC initialization proceeded in the same way, only without the need to include point charge ions.

Once equilibrium had been established, we would generally perform one of two types of simulation runs. In the first type, we would simulate the oscillation damping. To do so, we would instantaneously increase all of the electrons' velocities by $4.00\,\mathrm{km/s}$ in the z direction. The electron center-of-mass would then oscillate. To measure the oscillation damping time, we would fit a damped sine curve to the oscillation data to extract the damping time constant. See 5.1 for an example of the results obtained from this type of simulation run. Results could be obtained from either the full MD or MC simulations. In the case of the MC simulations, the electron temperature would increase with time as the center-of-mass velocity was converted by electron-ion collisions into random electron motion. To account for this, we periodically calculated the electron temperature using $\frac{3}{2}N_e k_{\mathrm{B}} T_e = \sum_{i=1}^{i=N_e} \frac{1}{2} m_e |\vec{v}_i - \vec{v}_{cm}|^2$ and then used this temperature in collision operator and probability calculations, where $\vec{v}_{cm}$ is the center-of-mass velocity of the electrons.

In the second type of simulation run, we would not alter the electron velocities after equilibration, but would just record them at evenly-spaced time intervals to measure their individual velocity deflections. The motivation for doing this is that the practical effect of electron-ion collisions is to increase the rate that electrons deflect from their initial velocity direction. To characterize the amount of deflection over a chosen time period, the deflection angle $\Delta\theta$ for each individual electron was calculated. The distribution of these deflection angles could be compiled and compared. If the collision operator in the MC simulation did a perfect job of modeling electron-ion collisions, then the distribution of deflection angles between the MC and full MD simulations would be the same and the oscillation damping rate would be identical, too. Any differences in deflection angle distributions would indicate that the full MD includes physics that is not being captured by the MC simulation.

We measured deflection angle distributions over a wide range of time periods, but concentrated our studies on the deflections over 5, 10, and 20 ns. The 5 ns time period is approximately equal to the time for an electron to move a_{WS}. We note that electron-electron collisions will cause deflections, too, and so even in the absence of electron-ion collisions there will be a range of

electron deflection angles. In fact, electron-electron collisions not only deflect but also alter the speed of electrons.

A natural way to plot distributions of deflection angles $\Delta\theta$ is through using a histogram, as shown in Fig. 5.2(a). However, we found that an alternative way of displaying the same results was useful. Such a plot is shown in Fig. 5.2(b). In this plot, the x-axis runs through all possible deflection angles. The y-axis plots the number of electrons with a deflection angle equal to or less than the associated deflection angle. In Fig. 5.2(b), the full MD curve has a smaller number of electrons through moderate deflection angles, indicating that there are more high-angle deflections in the full MD results than the MC results. This fact is also apparent in Fig. 5.2(a).

We also examined individual electron trajectories through space. Such an example electron trajectory is shown in Fig.5.3.

Because of the random initialization of particle positions, the oscillation damping rate and electron deflection distributions varied from simulation run to simulation run. We averaged over these variations through conducting multiple runs, usually having 6-10 runs per condition of interest with a run time of a few hours for each simulation.

5.3 Many-body collisions and electron oscillation damping

For the first part of our analysis, we used a binary collision operator in the MC simulation that was derived from Rutherford binary Coulomb scattering. [43] This type of collision operator involves a commonly-used approximate treatment of Coulomb collisions. While it is straightforward to implement and, as described below, provides a good match to for our plasma conditions in many respects, it has some conceptual and fundamental difficulties. Those limitations will be discussed in the latter part of this article.

For this collision operator, a maximum impact parameter, $b_{\max}$ is set for all electron-ion collisions, regardless of the electron velocity. The total cross section for a collision becomes $\pi b_{\max}^2$. The deflection angle is an analytic function of the impact parameter $b < b_{\max}$ and the electron velocity. In our MC code, if a collision occurs then an impact parameter between 0 and $b_{\max}$ is

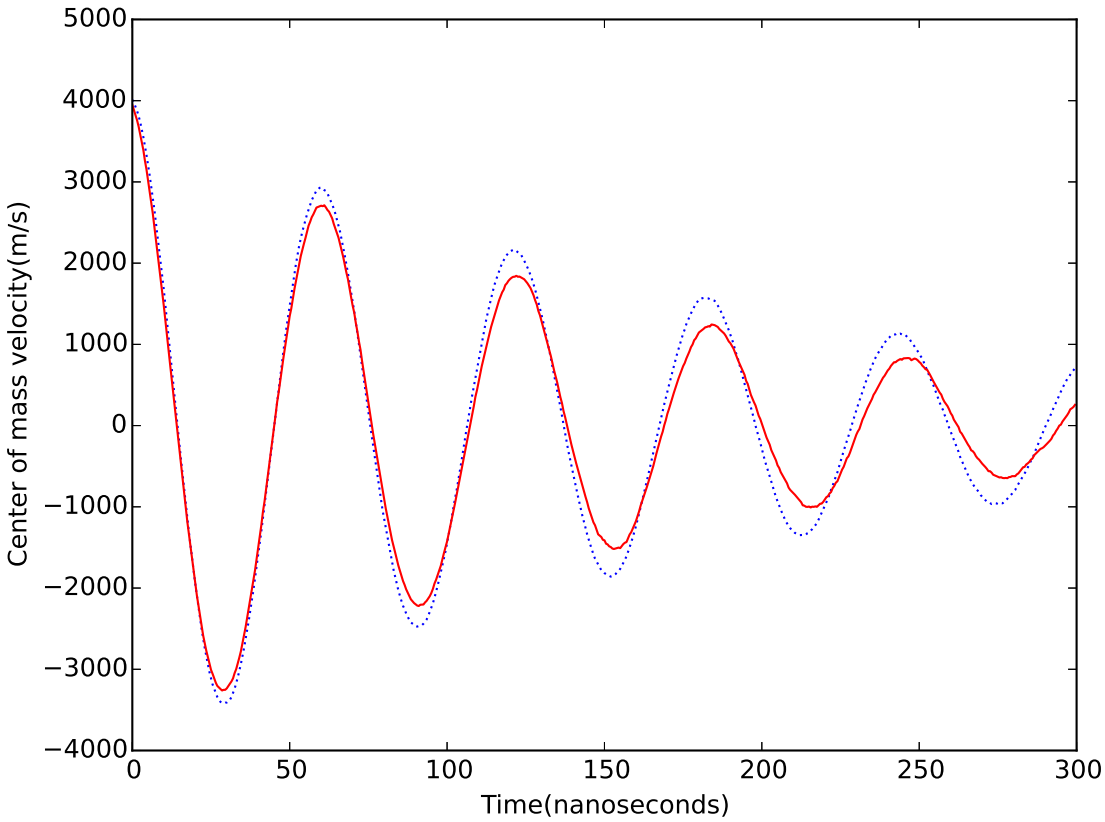

Figure 5.1: Center-of-mass oscillation damping numerical results. The electrons' center-of-mass velocity as a function of time is plotted, showing the oscillation decay. The red solid line is obtained from the full MD simulation while the blue dotted line is from the MC simulation. For this simulation, the electron initial temperature was $T_e = 1.65\,\mathrm{K}$ with the other relevant conditions described in the main text.

randomly selected. The electron deflection angle χ is then equal to $2\tan^{-1}(e^2/4\pi\epsilon_0 m v^2 b)$, where v is the electron speed.

We set the value of $b_{\max} = C\lambda_D$, where $\lambda_D = \sqrt{\epsilon_0 k_{\rm B} T_e/ne^2}$ is the electron Debye screening length and C is a constant. The value of was chosen to be 0.765 to match that which would be derived from the electron-ion thermalization rate reported in Ref. [21], which was consistent with the effective potential treatment in Ref. [22] . This value of C was also consistent with classical stopping power predictions in Ref [23] . Note that all of these references involve calculations that include strong coupling effects. These strong coupling effects result in an increase in the b_{max} parameter for sufficiently strong coupling, which is expected as the number of electrons in a Debye sphere in the plasma is decreasing as the strong coupling increases, impacting the electron screening. In the limit of weak coupling, C was set to be 0.765.

The ratio between the full MD and MC oscillation damping rates tends toward unity as the initial electron temperature is increased (i.e. as Γ is reduced). Fig. 5.4 shows this ratio as a function of T_e, which is proportional to $\frac{1}{\Gamma}$ at fixed electron density. This indicates that while the truncated Rutherford scattering collision operator does not do well at higher values of Γ, it works well when the electrons are sufficiently weakly coupled. It would of course be possible for the ratio to be made to be equal to one at lower electron temperatures through adjusting $b_{\max}$. Doing so, however, would produce collision operators that did not match the results of Refs. [21–23] and so would be in contradiction with those works.

The comparison between full MD and MC deflection angle distributions shown in Figs. 5.2(a) and 5.2(b) was obtained for conditions where Γ is higher (Γ=0.35). In these figures, it is evident that the MC simulation results in too high a ratio of small angle to large angle electron deflections as compared to the full MD. In principle, this could simply be due to an inaccurate collision operator. Through altering the value of $b_{\max}$ and artificially altering the value of e in the collision operator calculation, it was possible to get good agreement between the angle distributions in both the MC and full MD simulations (i.e. to match curves of the type shown in Fig. 5.2(b)). Once this was accomplished, however, the MC-derived damping rate became larger than the full MD-

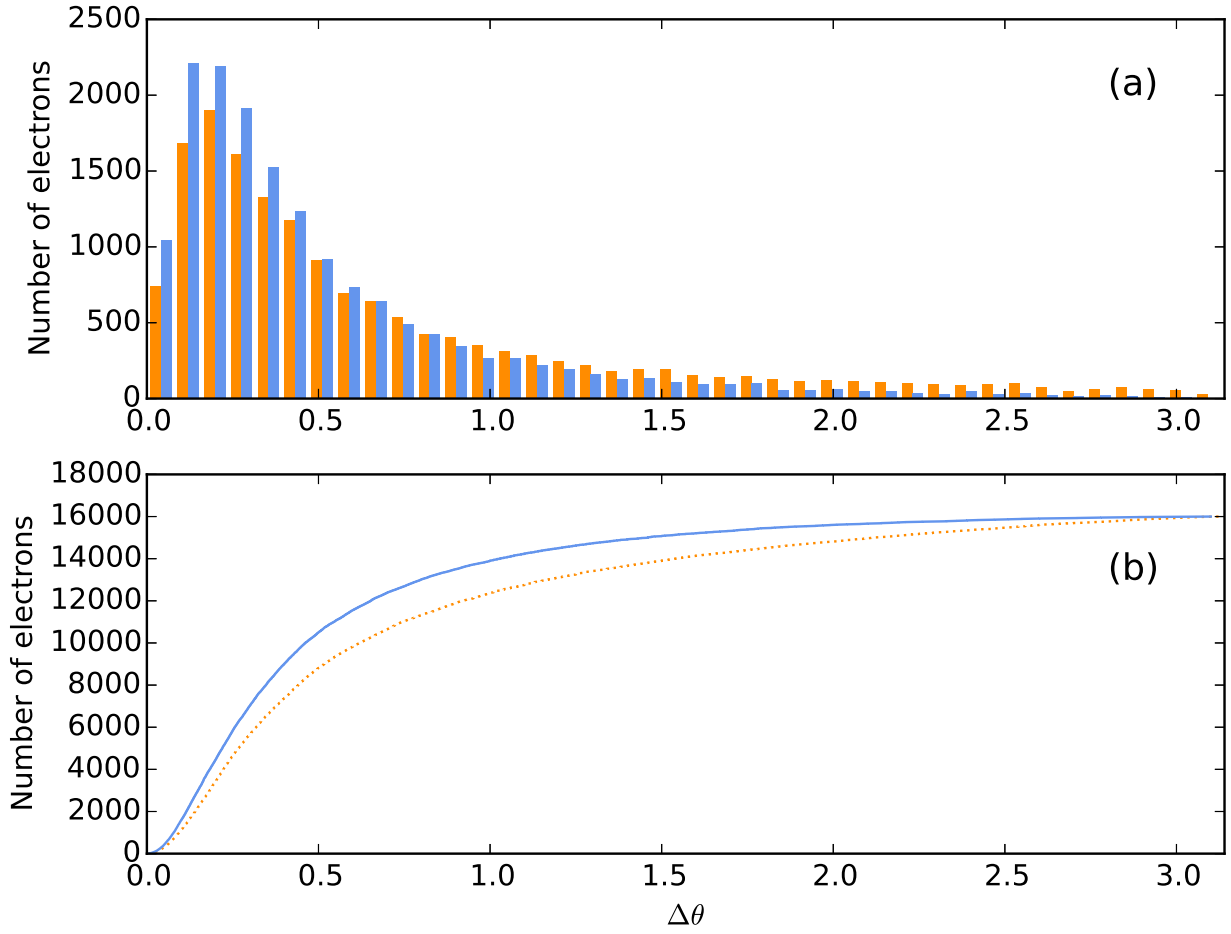

Figure 5.2: Comparison of the distribution of electron velocity deflection angles over a time period of 5 ns. The x-axis is measured in radians. For reference, $\omega_p^{-1} = \sqrt{\epsilon_0 m/e^2 n} = 5.60\,\mathrm{ns}$. In Fig. 5.2(a), The orange bars correspond to full MD simulation results, while the blue bars are obtained from MC simulations. In Fig. 5.2(b) the orange dotted line represents MD simulation while blue solid line represents MC simulation results. For these simulations, $T_e = 1.65\,\mathrm{K}$, corresponding to $\Gamma = 0.35$. Similar trends were observed for deflections computed over longer time periods than 5.0 ns. The MC collision operator used is described in the main text.

derived one by a factor of 3, meaning that matching the deflection angle distributions in this way produced a radical increase in the disagreement in the oscillation damping rate obtained from the two simulations. We also altered the $b_{\max}$ parameter alone to adjust the MC oscillation damping to match the full MD case. In that instance, the angle distribution curves still did not match, again indicating the insufficiency of such alterations of the binary collision operator to simultaneously match the angle distributions and oscillation damping rates.

In principle, such a disagreement between oscillation damping rate and deflection angle distribution could occur if there were sufficiently deeply-bound Rydberg atoms that were present before the oscillation was initiated and remained throughout the time that the oscillation damped. We confirmed that was not the cause of the discrepancy by performing auxiliary simulations where deeply-bound Rydberg atoms' ions and electrons were removed. Removing these deeply-bound Rydberg atoms did not substantially impact the oscillation damping rate. Additionally, such Rydberg atoms would be expected to decrease the amplitude but not the decay time constant of the oscillation curves, further indicating that deeply bound Rydberg atoms were not the source of the observed discrepancies.

To investigate the role of MBTBS contributions to the oscillation damping rate, we performed a series of simulations where we altered the ratio between the binary electron-ion collision rate and the MBTBS rate. This was accomplished by artificially decreasing the ion charge while increasing the ion number to keep the charge density of the ions constant. The ratio of binary electron-ion collision rate to MBTBS rate changes because the MBTBS rate scales more steeply with the ion charge. This can be inferred from expressions for the three-body recombination rate [52] as well as noting that many-body collisions involve volume considerations while binary collisions scale as a cross-sectional area, and so changes in fundamental length scale via altering the ion charge impact many-body more than binary collisions. This was confirmed in the full MD simulations through the observation of a reduced TBR heating rate for smaller ion charges. This, by the way, is why we did not conduct this test with higher ion charge values. Increasing the charge led to more TBR heating such that the desired values of electron Γ could not be obtained. The results of these

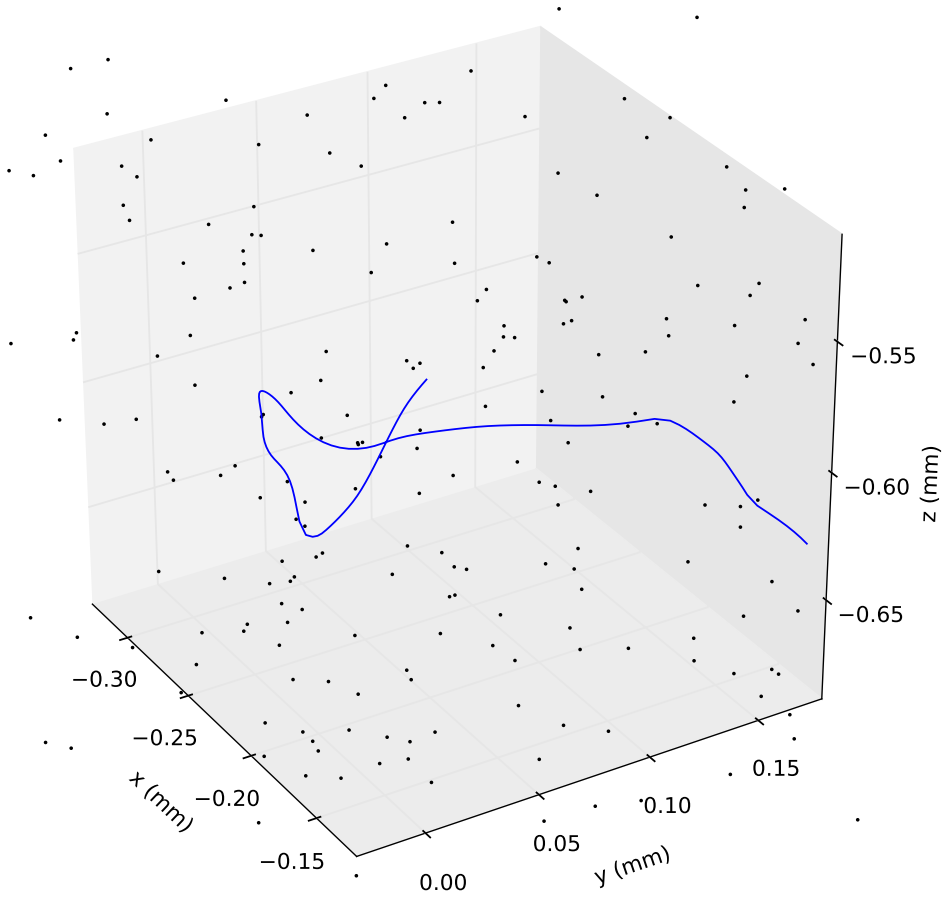

Figure 5.3: Sample electron trajectory. This 3D plot shows an electron trajectory over a period of 60.0 ns in a small region of the plasma. This electron trajectory was chosen to illustrate an electron that is initially free, but then becomes bound to a cluster of ions through a collision with another electron. The electron trajectory is shown as a solid blue line, while ions are represented as black dots. The other electrons in the region are not shown.

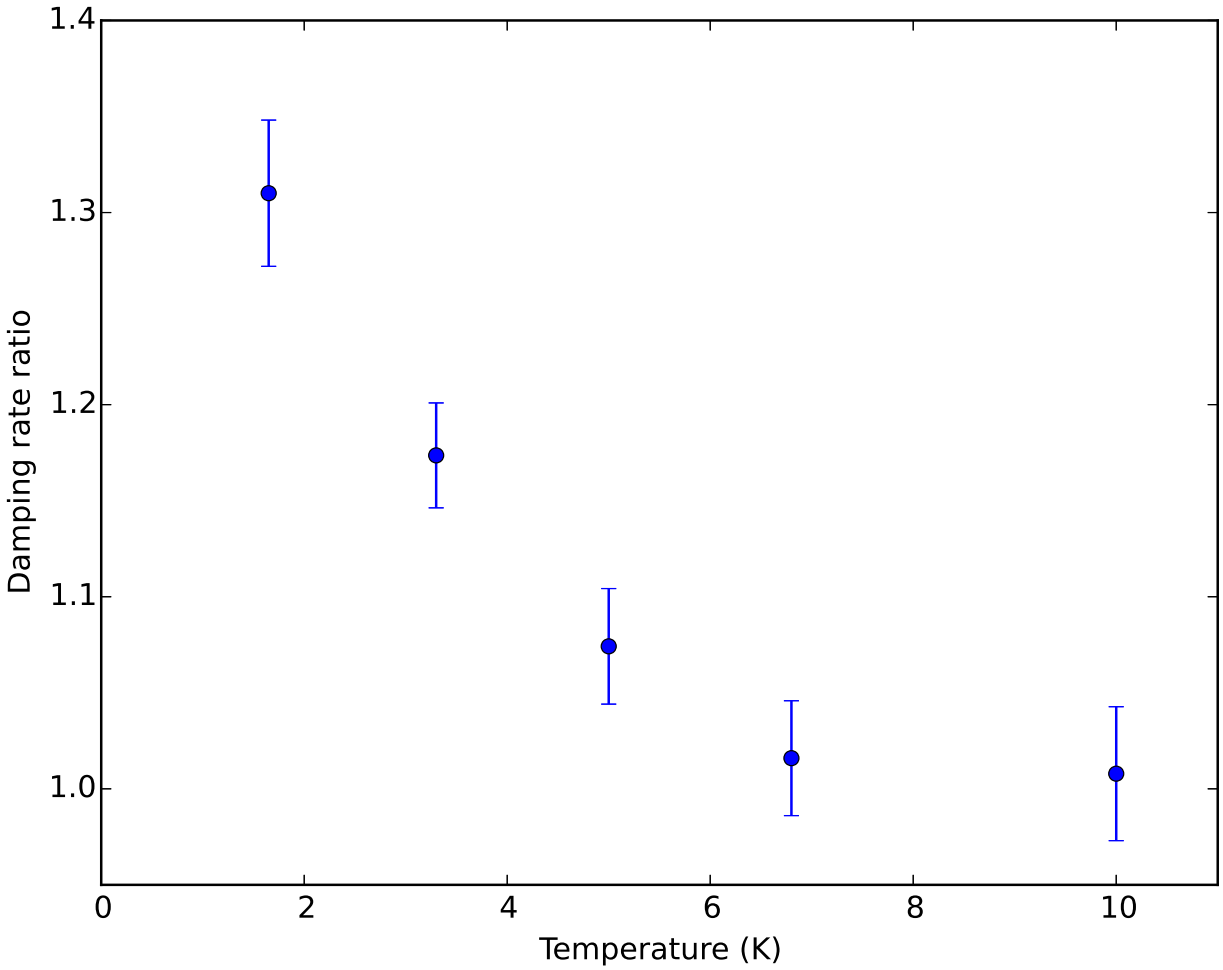

Figure 5.4: Ratio of full MD-derived oscillation damping rate to the MC-derived oscillation damping rate for the truncated Rutherford collision operator described in the main text as a function of initial electron temperature. As the initial electron temperature increases (i.e. for weaker coupling), the agreement between the two different simulation techniques improves. For reference, $\Gamma = 0.1$ corresponds to $T_e = 5.80\,\mathrm{K}$.

simulations are shown in Fig. 5.5. Note that as the ion charge is decreased, the ion number has to increase and the simulations become more computationally expensive. Similar to the case of weak-coupling, as the individual ion charge is decreased over the sampled range the discrepancy between the full MD and MC results diminishes. This suggests that decreasing the ratio of many-body to binary collisions reduces the disagreement between the full MD and MC results. We note that in these simulations nothing changes about the electron Γ or electron density — only the ion parameters change.

Beyond the sampled range, it is apparent that an extrapolation to zero ion charge is most consistent with a ratio of a few to several percent less than one. This is reasonable given the trend arising from a more theoretically-justified calculation of the electron-ion collision operator based on an effective potential theory that includes Barkas-like effects for opposite-signed charged particle collisions [53] as described in section 5.4 below. The Barkas effect refers to difference in stopping power for like-sign charge collisions vs. opposite-sign charge collisions.

We performed an additional analysis to characterize the number of electrons in bound states in the simulations. We defined a "localization" parameter for each electron over a chosen time period Δt. The localization parameter for an individual electron, which is a purely classical quantity, is defined as the ratio of the net spatial displacement of the electron ΔS to the average speed of the electron in the time period, $\bar{v}$, times Δt. In the absence of any collisions, this ratio would be one. Electron-electron collisions cause velocity changes and deflections and so those collisions produce a distribution of localization parameters. Binary electron-ion collisions cause further deflections. Bound state electrons, however, have much smaller displacements than free electrons in general and so for those electrons their localization parameters are much smaller.

Fig. 5.6 shows the distribution of localization parameters for electrons in the full MD and MC simulations. There are a far larger number of highly localized electrons in the full MD case. A few of these represent relatively deeply bound Rydberg atoms, but many more represent electrons that spend some time in a weakly bound state where they acquire large velocity angle deflections in a relatively short period of time. 5% of the electrons have a localization parameter of about 0.1 or

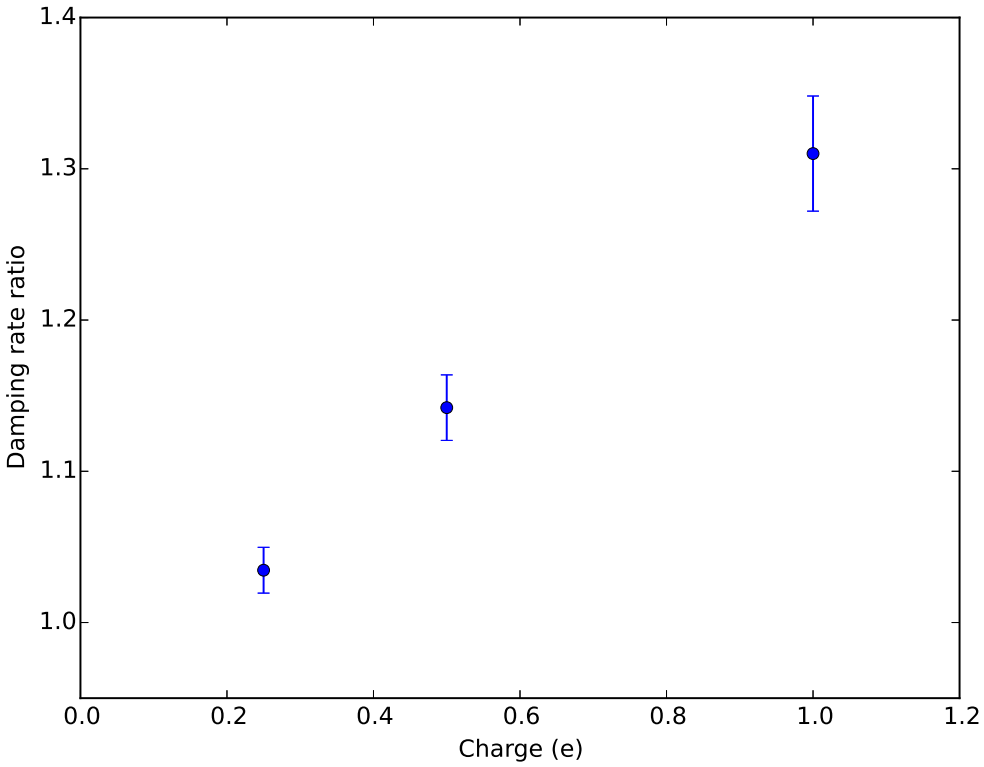

Figure 5.5: Ratio of oscillation damping rates determined from the full MD simulation to the MC simulation as a function of individual ion charge. For all simulations, as the charge of the individual ions were altered, the ion number density was adjusted to keep the charge density fixed. Over the range of ion charges investigated, as the ion charge tended toward zero the ratio between the full MD and MC oscillation damping rates becomes closer to unity.

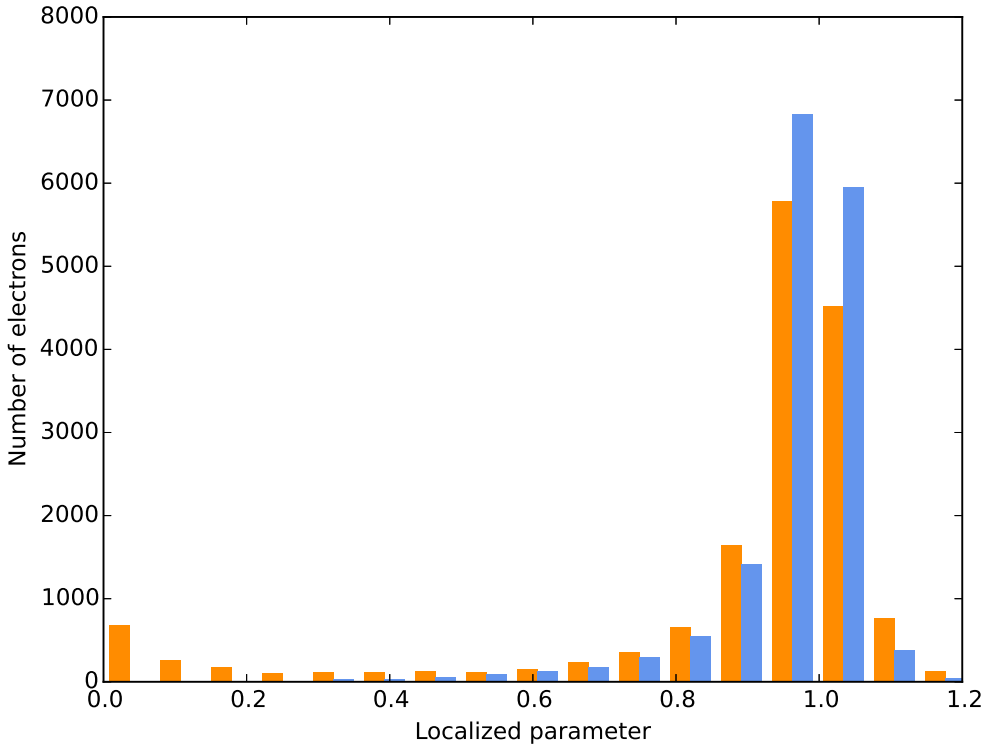

Figure 5.6: Histogram plot of the localization parameter. Blue bars represent the MC simulation results and the orange bars represent MD results. The MD results show a much higher fraction of electrons with localization parameters indicating a high degree of localization (i.e. small values as defined in the main text). The time period used for the data in this plot was 5 ns.

less, indicating that a substantial fraction of the electrons are significantly localized in the plasma. At this degree of localization, an electron's velocity direction would be nearly completely randomized in a plasma oscillation period. The localization parameter distribution and the observed gap in the oscillation damping rate between the full MD and MC simulations are thus in general agreement with one another.

5.4 Discussion

The fraction of electrons that have small localization parameters combined with the fact that electrons can be scattered into bound states and then scattered out of them in timescales on the order of a few plasma oscillation periods [10] suggests that MBTBS collisions are largely responsible for

the additional observed damping rate in the full MD simulation as compared to the MC simulations at higher electron Γ.

There are other possibilities, however, that were considered. We examined finite ion mass effects, non-spherical symmetry, and finite spatial extent effects and found them to have no more than a few percent effect on the oscillation damping rate. Ion correlations were found to have up to a several percent impact on the oscillation damping rate, presumably through ion screening effects. However, for the infinite mass and randomly placed ions in the current set of simulations such considerations are not relevant.

Perhaps the most important consideration, however, concerns the use of the truncated Rutherford collision operator. Such a collision operator is easy to treat analytically and easy to implement. It is, however, unphysical in two respects. First, there is no screening included in the collision calculation other than the truncation. Second, the truncation of the impact parameter is quite unphysical in that it is not that a finite-ranged potential interaction is used, but rather a potential that is finite in radial extent prior to the collision and infinite after it. [43] It is true that the truncated Rutherford collision operator matched the full MD simulation well under conditions of weak coupling and lower MBTBS-to-binary-collision ratios, but there are reasons to believe that such agreement would likely break down when strong coupling physics became more significant. In addition, recent work indicates that there is a Barkas-like effect in collisions between unlike-signed particles (such as electrons and positively-charged ions) [53] that becomes significant with increasing Γ, and such an effect is not present in the Rutherford scattering operator.

Following the work in Ref. [53], we used a collision operator that included screening effects and the Barkas-like effect as derived from an effective potential to compute the predicted oscillating damping rate at the Γ=0.35 conditions. We obtained the collision differential cross sections necessary for the collision operator from the authors of Ref. [53]. Using this collision operator in the MC simulation, the MC-derived oscillation damping rate increased by 6% over the truncated Rutherford collision operator. While in the right direction, this increase is not enough to explain the original full MD/MC discrepancy. In contrast, using a simple Yukawa interaction potential with

a screening length chosen to match the stopping power and thermalization rates in Refs. [21–23] actually reduced the MC predicted damping rate by 20% as compared to the truncated Rutherford calculation. So the treatment that included the Barkas effect and used an effective potential was much better than a simple implementation of a Yukawa potential. In the end, though, improvements in the MC collision operator did not resolve the full discrepancy with the full MD calculation for the $\Gamma = 0.35$ condition.

In light of this, to further investigate whether rare events that result in a very high deflection of an electron's velocity direction are the cause of the discrepancy, we conducted angle distribution calculations using the usual MC collision operator plus an addition. We added the possibility of another – artificial – collision occurring where there was a probability in a time period for each electron whose speed was below a maximum speed ($v_{\max}$) to have its velocity direction completely randomized. This additional artificial type of collision was chosen to roughly simulate an electron becoming bound, deflecting in direction substantially while bound, and then becoming unbound via a collision after that deflection. The use of a threshold was motivated by the fact that MBTBS collisions are more likely for slower-moving electrons. We adjusted the random probability for these artificial collisions until the oscillation damping decay rate in the MC simulation matched that in the MD simulation.

The resulting angle distribution curves are shown in Fig. 5.7. The random probability rate for the artificial high-angle-deflection collisions was set to be $2.42 \times 10^5\,\mathrm{s}^{-1}$ with $v_{\max} = 8\,\mathrm{km/s}$. It is evident that in the upper plot in Fig. 5.7 the additional artificial collision probability being added to the MC simulation reproduces the angle distribution curve well for Δt=20 ns. The comparison between the modified MC and MD is not perfect, as seen in the lower plot of Fig. 5.7 for a shorter Δt. However, this comparison shows that the MD simulation can be matched over $\Delta t = 20\mathrm{ns}$ in both oscillation damping rate and angle deflection distribution by adding rare but very high-deflection events that would be similar to the net expected effect from actual MBTBS collisions.

It is hard to definitively eliminate the possibility that yet another binary collision operator could reproduce the rates observed in other work [21–23], could match the angle distributions between

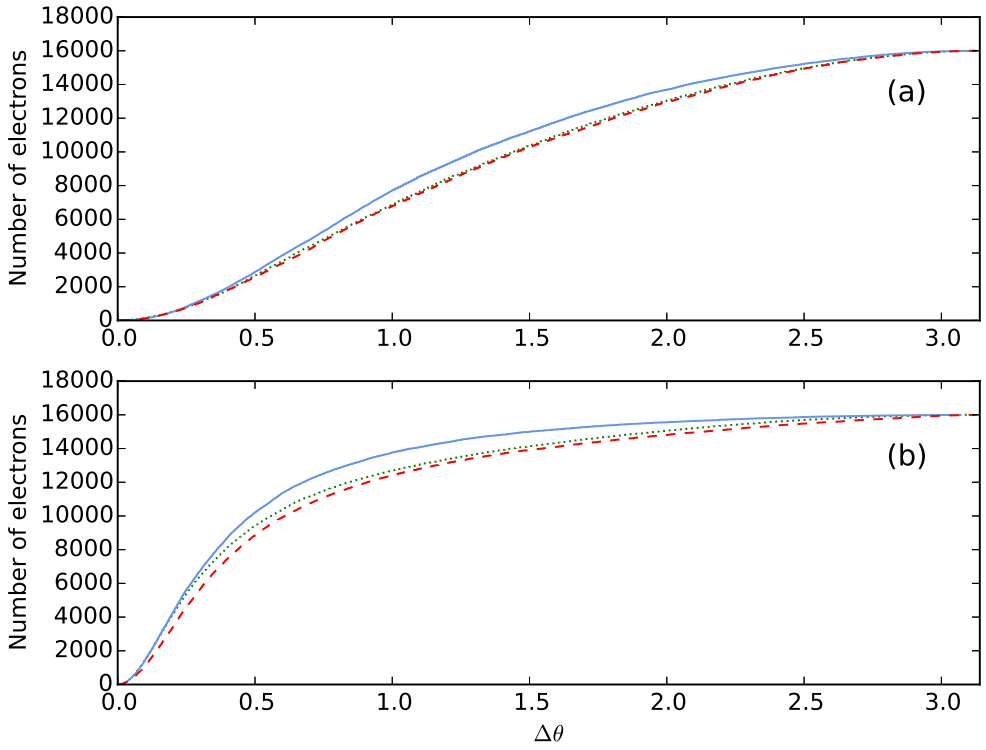

Figure 5.7: Cumulative collision angle distribution plots, similar to those in Fig. 5.2(b). The simulation parameters such as density and temperature are the same in this plot as in that one. Part (a) in this plot represents results obtained with $\Delta t = 20\,\mathrm{ns}$, while part (b) corresponds to $\Delta t = 5\,\mathrm{ns}$. The blue solid line represents the usual MC result as presented in the text, while the red dashed line represents the MD result. The green dotted line represents the MC result with the addition of randomly occurring events where the velocity direction of an electron is completely randomized.

full MD and MC simulations while simultaneously matching the oscillation damping rates, could produce the same degree of electron localization, would tend to reduce to the truncated Rutherford collision operator in the limit of small individual ion charge, and would be physically reasonable. The balance of all of these considerations and results presented above are highly consistent with the majority of the gap between the full MD and MC predictions being due to MBTBS collisions and subsequent scattering of those electrons back into unbound states.

5.5 Conclusion

We have used two separate simulation techniques to calculate the damping rate of electron oscillations in conditions where electron strong coupling is relevant. We found that the result

obtained from a full MD simulation that treated both the electrons and ions as point particles did not agree at the tens of percent level with a MC simulation that treated electron-ion collisions via a random binary collision operator based on an electron-ion collision theory consistent with work published in Refs. [21–23]. We ascribe this difference to the effect of many-body collisions that scatter electrons into being bound to one or more ions. When these electrons become bound, their velocity direction changes quickly. These electrons can be scattered back into a unbound state and thus can contribute significantly to the decay rate of the average electron momentum in the plasma. Scaling studies and characterizations of the degree of "localization" of the electrons indicated that these many-body collisions to bound states are sufficient to observe the explained simulation discrepancy.

In most plasmas, three-body recombination is not the dominant recombination mechanism and can generally be ignored. This won't be the case for sufficiently strongly coupled electrons, however, and MBTBS collisions like those discussed here will be relevant. This is the case, for instance, for some warm dense matter conditions. [54, 55] Also, recombination effects that impact electron-ion collision properties are relevant to plasma stopping power. [56] We note that significant discrepancies have manifested themselves at a relatively mild value of Γ=0.35, indicating that even with only a moderate degree of strong coupling, many-body collisions need careful consideration in order to avoid distorting binary collision predictions or analyses.

Chapter 6

High-frequency RF heating of UNPs from weak to extreme electron magnetization

Magnetic fields are common in plasmas and often have strong influences on plasma transport [22, 45], conductivity [27], energy flow, stability, and, at the strongest magnetic fields, collision rates and screening dynamics [11]

Magnetic fields are used or present in fusion experiments [57], common in astrophysical plasmas [58], and have technological applications in charged particle trapping and control [59]. For sufficiently strong magnetic fields the inverse of the cyclotron frequency of plasma particles becomes a much shorter timescale than that associated with any other plasma dynamics. This makes direct simulation and first-principles theories challenging. Other treatments rely on necessary approximations and assumptions [26].

UNPs are an excellent system in which to study many aspects of magnetic field effects on plasmas. In UNPs, particles are dilute and cold in comparison to most laboratory and many natural plasmas. As a direct result of this, it is possible to obtain substantial degrees of magnetization with only mild laboratory fields, especially for the electron component. In addition, the low densities ($10^{13} m^{-3}$ for our experiments) make the plasma evolution time scale of UNP orders of magnitude slower than many other plasmas. This makes for more accessible and table-top friendly experiments. UNPs usually contain simple components and are made in characterizable field environments. Because of all these features, UNPs can be used to study plasma properties including plasma thermalization [21], expansion [3, 8, 38], conductivity, and heating and cooling mechanisms.

UNPs are also very classical plasmas and so direct comparison to theoretical predictions based on classical physics can be made. In this work, we probe electron-ion collision rates as a function of electron magnetization through measuring the amount of electron heating induced by high-

frequency radiofrequency (RF) fields. We compare our measured heating rates to both direct simulations and predictions from linear response theory. We find qualitative agreement between predictions in experiment but disagreement at the quantitative level. We will describe possible sources of that disagreement and preliminary results of one explanation look promising.

RF fields are generally considered to be high-frequency if the applied oscillation frequency (ω) is greater than the electron plasma frequency ($\omega_p = \sqrt{\frac{ne^2}{\epsilon_0 m_e}}$) where n is the electron density, e the electron fundamental charge, m_e the electron mass, and ϵ_0 the dielectric constant of the vacuum. Given the spherically-symmetric nature of our UNPs, another frequency to be consdiered is the electron center-of-mass oscillation frequency, which is smaller than the usual electron plasma frequency by typically a factor of 2 for our conditions. For high-frequency RF fields, Electron-electron collision-induced heating is approximately zero because all electrons have the same oscillatory motion induced by the RF field and so the RF field does not induce relative motion. That is not the case for electron-ion collisions as the ions do not have the same induced motion from the RF field since they have a much larger mass. The resulting electron-ion collisions heat the electrons and so probing the RF heating rate probes the electron-ion collision rate.

Our experiments are conducted over a range of applied magnetic fields. In UNPs, the magnetic field is externally applied and can be controlled and so different 'regimes' [11] can be accessed from weak to extreme magnetization as mentioned in section 2.5. Here is a review of relevant length scale comparisons: in weakly magnetized plasmas, r_c is less than the mean-free-path transport length but greater than the Debye screening length λ_D and binary collision length b_L. For "extremely" magnetized electrons, r_c is smaller than λ_D and b_L while for "strongly" magnetized electrons $r_L < r_c < \lambda_D$. Very roughly, in weakly magnetized plasmas the magnetic field is relevant for long-range transport, in strongly magnetized plasmas the magnetic field is strong enough to influence screening dynamics, and in extremely magnetized plasmas close-range binary collisions are substantially affected.

6.1 Additional Comments on Electron-Ion Collisions in a Magnetic Field

In our UNPs, the large mass difference between the electrons and ions means that an electron-ion collision can be well-approximated by a collision between an electron and infinite-mass ion. Despite the fact that the equations of motion for an electron colliding with an infinite-mass ion in the presence of a magnetic field are straightforward, the motion of the electron during the collision can be complicated. For particular ranges of initial electron velocity and impact parameter, chaotic behavior occurs with regard to parameters such as the deflection angle that results from the collision. More detailed discussion can be found in chapter 2.5. This behavior complicates the theoretical description of magnetized electron-ion collisions in moderately- to strongly-coupled plasmas where pertubation theory is inapplicable. It is possible to develop a generalized collision operator by computing a sufficient number of trajectories to average over the chaotic variations as has been done in [60]. This work was very computationally intensive, though, as many trajectories needed to be computed to achieve convergence. The screening effect of the plasma needs to be included in the calculation of the collision operator, too, as the binary collisions in the plasma are not occurring between isolated particles.

An alternative way to compute the average forces and energy transfer between electrons and ions in a magnetized plasma is to treat the electrons as a dielectric fluid and compute their response to ions that move through them [27]. Magnetic fields change the dielectric response and hence the predicted energy transfer. This theoretical treatment does not produce the chaotic behavior evident in a binary collision treatment. This is not because the chaotic behavior is not present, but because the assumptions of the linear response theory eliminate the chaos. In particular, while theories describing binary collisions in plasmas have to use some method to account for screening so as to avoid divergences at large collision impact parameters, linear response theories need to use a method to eliminate divergences at small distance scales where the chaotic behavior is most often

found. The more weakly coupled a plasma is, the better the approximations used in the linear response theory should apply.

The fact that we are using high-frequency RF heating simplifies our experimental studies but adds another complication to binary collision theory. A reasonable timescale to associate with a binary collision in a plasma is $\frac{\lambda_D}{v_{th}}$ where $v_{th} = \sqrt{\frac{k_B T_e}{m_e}}$ is a thermal velocity of the electrons. Since $\omega_p = \frac{\lambda_D}{v_{th}}$, high-frequency RF has an oscillation period that is shorter than a binary collision time. This complicates the development of an appropriate collision operator. Linear response theory is not affected in the same way and accommodates high-frequency RF heating more naturally.

In light of these considerations, our first comparison of our experimental results is to the predicted heating rate from linear response theory with magnetized electrons [27]. Our UNPs are not strongly coupled with an electron strong coupling parameter $\Gamma = 0.12$ on average. For similar conditions in a stopping power calculation [61] there is agreement between the predicted friction force on an ion moving slowly compared to v_{th} between linear response theory and a generalized collision operator. This slow-ion region aligns with our experimental parameters. Such an agreement may not hold for high-frequency RF heating but it is an indication that a comparison between experimental results and linear response theory is not doomed to inaccuracy from ignoring the complications evident in binary collision theories. We therefore compare our measured heating rates to linear response theory predictions. Any deviations of observations from those predictions would then give insight into where the theory could be failing and what additional considerations need to be included.

The field geometry that we use is one where the RF field is designed to be applied longitudinally along the direction of the applied magnetic field. It is interesting to consider possible qualitative changes in RF heating rate as a function of magnetic field in this geometry. As the magnetic field is increased, the electrons will be "pinned" more and more to the magnetic field lines and the value of r_c will decrease. General expectations and explicit calculations using a simple Coulomb force show that for sufficiently large impact parameters in a binary collision, increases in magnetic field decrease any deflection of the electron (and hence the RF heating rate). An incorrect inference

would be that as the magnetic field was increased the RF heating rate would go to zero since large impact parameter collisions are significant contributors to collision rates in plasmas. Instead, the predicted RF heating rate from linear response theory hardly varies as a function of magnetic field from weak to extreme magnetization even in the infinite magnetic field limit. This is not because small impact parameter large-angle collisions are offsetting decreases in small-angle large impact parameter collisions. Linear response theory does not treat small impact parameter collisions by assumption and construction. Instead, the screening response of the plasma electrons adjusts as a function of magnetic field in such a way as to keep the predicted RF heating rate approximately constant. The implications of this will be explored in section 6.4 below.

Another option to predicting the RF heating rate via a theory is to construct a simulation of the UNP to predict the RF heating rate numerically. The number of particles in our experiment is not all that large compared to many other plasmas ($\sim 10^5$ electrons and ions) and so 1:1 modeling seemed at least feasible. However, the magnetic field introduces a new time scale that can be very short compared to any other in the plasma. Resolving the cyclotron motion requires very small timesteps in order to get convergence. Additionally, the presence of chaotic behavior in binary collisions could exacerbate this problem by requiring further reduction of the timestep to sufficiently resolve proper deflection angles in these collisions. Our MD simulation studies, involving almost 20,000 particles under the influence of a magnetic field, have showed that the convergence of individual particle trajectories remains unknown at a timestep as short as 10 femtoseconds. This time step already demands substantial computing resources and each simulation run requires 3 days to complete for a number of particles that is an order of magnitude smaller than the number in our experiments. In-depth analysis of this topic is presented in Chapter 3.

Furthermore, under our current conditions, even though the de Broglie wavelength of the electrons (31 nm) is considerably smaller than the other typical length scales that are often discussed (e.g.$b_L = 4.1\mu m$), it's worth noting that our MD simulation is developed on pure classical physics and that some of the collisions in the chaotic regions have deflections that vary substantially for impact parmeter variations smaller than the de Broglie wavelength. At present, the specific quan-

tum effects affecting particle interactions remain unclear, and further investigation in this area is required in the future.

Despite these difficulties, We still performed simulation studies using a molecular dynamics simulation and we want to make comparisons to our experiment results. There are trends in the simulations that can be commented upon and such a comparison will be made after the experimental results are presented.

6.2 Experimental apparatus

In order to collect our RF heating data, UNPs had to first be created and then their parameters tuned. RF pulses had to be applied and the change in electron temperature detected and characterized. Calibrations then needed to be performed to determine the amount of heating, n, T_e, RF field amplitude, and relationship between auxiliary measurements that we performed. This section describes the experimental sequence, data analysis, and calibrations.

The experimental sequence for forming a UNP is presented in chapter 2.6. A very brief review is presented here. An experiment sequence begins by laser-cooling ^{85}Rb atoms to approximately $100\mu K$ in a magneto-optical trap (MOT). The atoms are then transferred to a purely magnetic anti-Helmholz (AH) magnetic trap. After that the cold atoms are transferred to the photoionization region of the vacuum chamber using a translation stage to move the coils producing the field that creates the AH trap. Next, the AH trap magnetic field is turned off and a 780nm (red) diode laser is used to excite the ^{85}Rb atom from the $5S_{1/2}$ ground state to $5P_{3/2}$ excited state. Then a pulsed dye laser with a tunable wavelength near 478nm (blue) is used to photoionize the excited state atoms. The electron initial kinetic energy can be tuned through changing the blue laser wavelength. After photoionization some electrons leave the region in space where the atoms were and that creates a space charge from the ions that creates a potential that traps the remaining electrons forming a UNP [2].

Around the UNP formation region is a collection of wire grids and electrodes that allow the application of DC and RF electric fields to the UNP. Electrons that escape from the UNP are directed

along the z-axis to a microchannel plate (MCP) detector that produces a signal proportional to the electron escape rate. This is the primary signal for our experiments. In addition to the electric fields, a 120-turn coil is used to apply a fast turn-on and steady magnetic field to the UNP along the z-axis. Besides that coil, a separate coil "downstream" of the plasma towards the MCP is used to create a guiding magnetic field for electrons that have escaped the UNP to help ensure they strike the MCP. Again, more detailed description can be found in chapter 2.6.

After the UNP is formed, we use programmed electric fields to adjust UNP parameters, collect a signal that is sensitive to the electron temperature, and measure the total electron number. A typical sequence for this applied field is shown in Figure 6.1. Right after the UNP is formed, a $2\mu s$-long triangle ramp with 5 V/m field amplitude is applied in order to remove some of the electrons from the plasma adiabatically. This deepens the confining potential for the remaining electrons. The resulting charge imbalance δ is defined as the ratio of the number of electrons to ions. δ needs to be within an acceptable range because when it is too low the ions will trap the electrons too deeply and it is hard to use electric fields to extract the electrons out of the plasma, which contains electron temperature information (the most important data in our analysis). On the other hand, we don't want any electron loss because of weak ion trapping too early (during the heating process) because we rely on conservation of energy in our analysis. In our experiment we keep δ around 0.75. After the triangle ramp there is a "test period" during which a variety of different pulses used to heat the plasma can be applied. These are described in more detail below. After that period, electric field ramps are used to extract first some and then later all the electrons. The first of these electric field ramps is called the "partial extraction ramp" and its amplitude is set to extract 10-15% of the total electrons. For a fixed δ, the higher the value of T_e the larger the number of electrons that are extracted by this pulse and so it provides a signal that is sensitive to T_e and this is the signal that tells us how much heating occurs in the UNP. The last ramp we term the "full extraction" ramp and it directs all the electrons in the UNP to the MCP, allowing for a determination of the total electron number. It is possible to create a model that relates the electron temperature to the fraction of electrons that escape due to the partial extraction voltage.

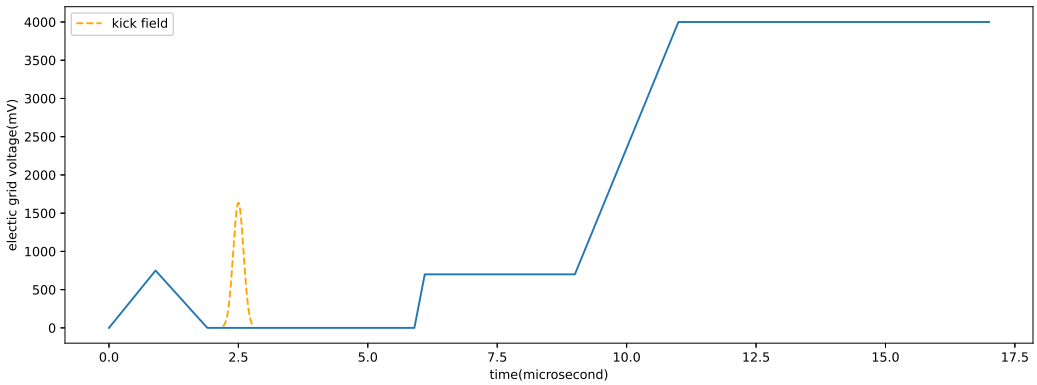

Figure 6.1: Voltage levels of a programmed DC electric field applied in the plasma region of the chamber created by an arbitrary function generator vs. time (t). The UNP is created at t=0. t=0 to 2 μs is the triangle ramp being applied to tune the charge imbalance. There is a test period that follows where an RF pulse or a kick is applied (see main text) and then there is a thermalization period. For clarity, the shortest dead period used is shown in this figure. After the dead period are the partial and full extraction pulse to determine the electron temperature and the total electron number, respectively. 1 V produces a field of 7.5 $\frac{v}{m}$ at the UNP. The orange dashed line in the plot represents the 'kick' field, which can be applied at time $2.5\mu s$. Other forms of fields, such as the RF field, can also be applied at this time. It's important to note that, for presentation purposes, the orange line only shows the kick field's amplitude, and not its direction. In the experiment, the kick field has the opposite sign of the DC electric field.

That fraction, however, is very sensitive to UNP parameters such as density and number as well as stray electric fields and such a model would be not only complex but require a substantial amount of data to confirm its validity. To measure electron temperature changes, we instead compare the fraction of electrons that escape due to the partial extraction voltage between two different heating methods. One of the methods is the one that we would like to test and one is a method that induces a calibrated amount of heating. By finding the conditions that result in the same partial extraction voltage-induced electron escape between the two methods, the amount of heating from the method being tested can be determined to be the same as the calibrated heating amount. Using this method, a model of the fraction of electrons that escape due to the partial extraction voltage is not needed. This comparison does require that the electrons are sufficiently close to thermal equilibrium. If they are not, finding the conditions such that the extracted electron fraction between different heating methods is the same no longer means that the amount of heating imparted to the electrons is the same. In this work, it was found that initial measurements and assumptions about thermal

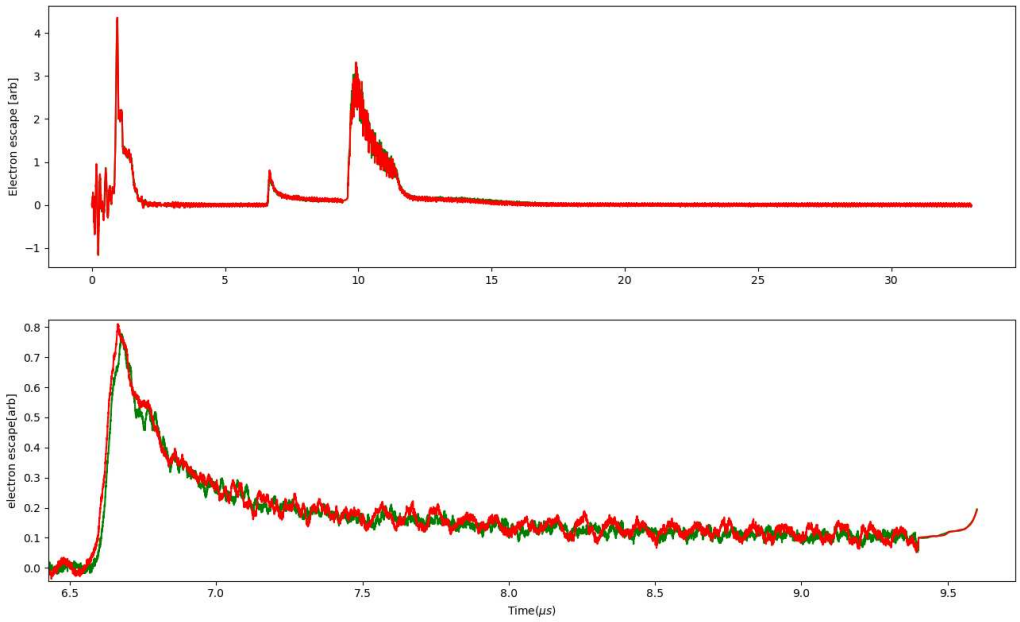

Figure 6.2: The upper plot shows the electron escape MCP signal in arbitrary units, guided by the field provided in Figure 6.1. The red curve represents the escape signal with a "kick" field applied during the time window from 2 to $3\mu s$, as shown in Figure 6.1, the "kick" field will be explained in detail in section 6.3. The green curve is without the "kick" field. The lower figure is an enlarged trace from the upper figure, covering the time range from 6.5 to $10\mu s$. It's important to note that the overall difference between the green and red traces is quite small. The most critical part of our data analysis comes from the difference between the green and red traces in the lower figure. Each trace represents an average of 100 experimental shots.

equilibrium times were flawed. New measurements indicate how long equilibration needs to be established for these measurements.

6.3 Description of RF heating experiment

To characterize the off-resonance RF Heating rate we define a parameter η that is a function of UNP density n, degree of magnetization $\beta = \omega_c/\omega_p$ where $\omega_c = eB/m_e$ is the electron cyclotron frequency, RF field amplitude E, and RF frequency ω_0 and is defined such that the average rate of kinetic energy (KE_e) increase in the electrons due to RF heating is given as

$$\frac{dKE_e}{dt} = \frac{1}{2}\eta m_e \omega_0^2 a^2 \tag{6.1}$$

where a is the amplitude of the oscillation of the electrons caused by the RF field. In the limit that E goes to zero, η becomes independent of E. In the absence of electron-ion collisions, η is approximately zero for our experimental conditions as determined through MC simulations. It is directly proportional to the absorptive part of the AC conductivity of the plasma, and so measurements of η are in turn measurements of the absorptive part of the AC conductivity as well.

Table 6.1: Plasma and Experiment Conditions

Parameter	Value
Density	$1.4 \times 10^{13}\,\mathrm{m}^{-3}$
Temperature	$5.75\,\mathrm{K}$
$\beta(\omega_c/\omega_p)$ Range	1-12
Plasma Center-of-Mass Resonance Frequency	$16\,\mathrm{MHz}$
RF Frequency For Heating Experiment	$60\,\mathrm{MHz}$

In order to measure the relative RF heating rate vs. β, several quantities can be fixed such as n_e, ω_0, and electron temperature rise amount ΔT. Then the relative heating rate can be obtained by using the ratios of E applied under different magnetizations with the same n , ω_0, and ΔT. Smaller values of η require larger values of E when these other quantities are fixed and vice-versa.

So, instead of measuring n and ΔT, these quantities are calibrated and stay the same throughout the experiment.

Once the relative values of η are known, the absolute RF heating rate can be determined at a single value of β to get information about the absolute heating rate at other values of β.

As mentioned above, the goal of our measurements is to measure η, or equivalently the absorptive part of the AC conductivity of the plasma, as a function of electron magnetization from "weak" to "extreme" To do so we apply an RF field for a fixed period of time to observe the electron heating that is induced. The RF field amplitude is turned on and off slowly enough that the electrons follow it adiabatically and in the absence of electron-ion collisions there would be no electron heating for the frequency that we used. We confirmed this with simulations, too.

We measured the RF electric field amplitude E for each value of β that produced a fixed temperature rise. We assume that the RF heating scales linearly with E^2 and from that can determine relative values of η at different values of β. Theoretical estimates [27] indicate that nonlinear effects are expected to be smaller than the error bars in the measurements being conducted, being at most a several percent effect.

Before presenting the data that we obtained and more details about the RF heating measurement, we will discuss the calibrations that were performed. Some of these calibrations were necessary to determine the absolute value of η while others were necessary in order to make relative comparisons.

6.3.1 Density calibration

Since η is a function of n relative comparisons are easiest for conditions with the same n. If the electrons are displaced relative to the ions, they will oscillate with a center-of-mass frequency ω_{cm} that is proportional to $\sqrt{n}$. To set the UNP density n, we vary the total ionization number of electrons and ions through altering the intensity of the red photoionization light while applying an RF field tuned to the value we desire for ω_{cm}. The UNP size is fixed because it is determined by the magnetic field strength of the AH coil and the temperature of the ultracold atoms prior to

photoionization and that does not vary on average. When the center-of-mass frequency of UNP electrons closely matches the applied RF frequency, electron oscillations become resonant with the RF frequency. This resonance results in electrons acquiring sufficient kinetic energy to escape from the UNP. We name the escaped electron number as $N_{RFescape}$ and total electron number as N_{total}. N_{total} can be counted when we apply the full extraction ramp. When UNP oscillation is on resonance with the applied RF field (which we set to 16 MHz), maximum $N_{RFescape}$ reached. Figure 6.3. shows the N_{total} vs $N_{RFescape}$ under different magnetic fields. We use a least square fit method and fit this data to a Lorentzian shape function that can have an offset from zero that at high number. The total electron number corresponding to the resonant value is identified from the fit. After this measurement, we prepared our UNPs using the total electron number that matched our desired density and kept using this number for the remainder of our experiments under that specific magnetic field. As needed, we would periodically re-measure the resonant frequency condition to check for any drifts. The resonant condition was observed to be stable over several days. The density calibration is done at each magnetic field of interest before collecting off-resonance RF heating measurement data in order to make sure the UNP density stays the same no matter how the magnetic field changes. The RF amplitude is also fixed to ensure our calibration is consistent. To maintain the most consistent UNP conditions, we sought to hold the density of the UNP as constant as possible while studying the RF heating rate versus magnetic field. We also wanted to maintain the same internal and external electric fields as much as possible. This was achieved by ensuring that both the charge imbalance and plasma density remain constant across different magnetic fields. We made sure that the charge imbalance was consistent within a set of measurements at a given magnetic field at the same time that we were making sure the density was at our desired value as well. By adjusting both the triangle ramp amplitude and the plasma density, we maintained a consistent internal electric field environment within the UNP.

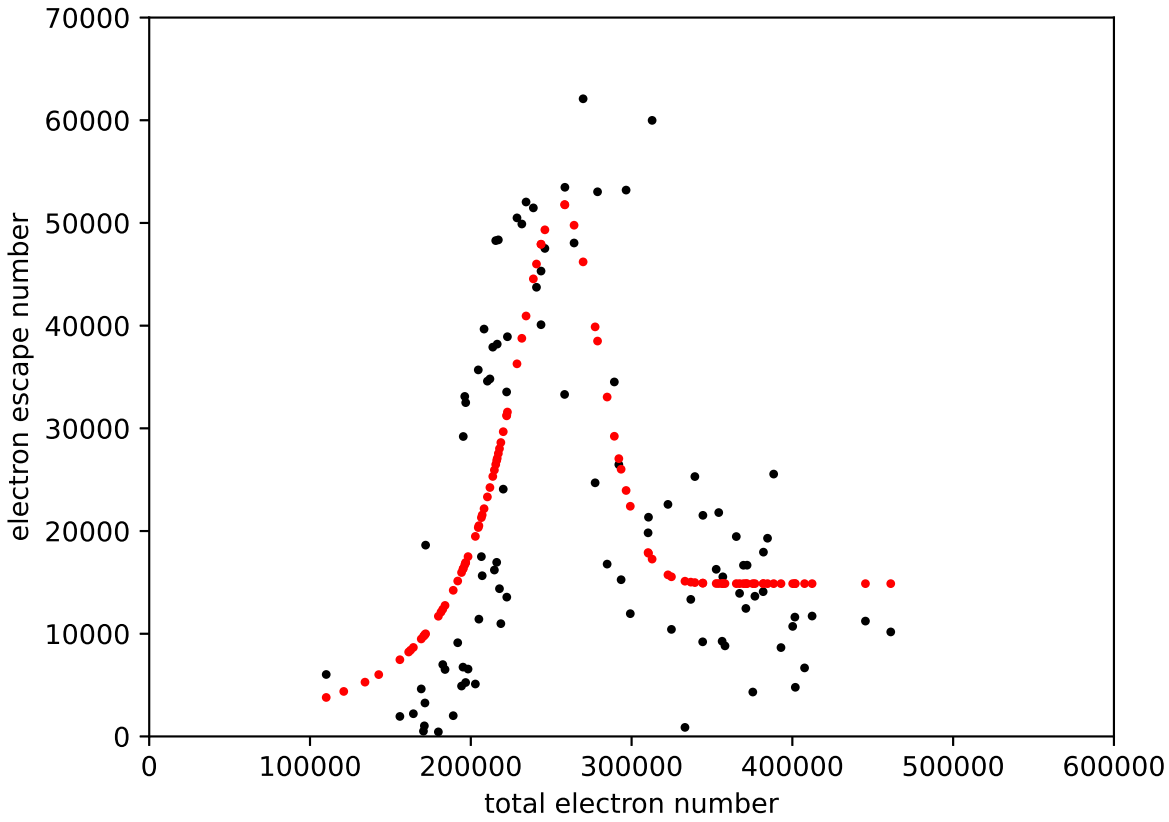

Figure 6.3: Total electron number vs electron escape from RF field under different magnetic field. Changing the intensity of the red laser changes the total number and we sweep through a density range to find the maximum escape from RF field associated total number. Black dots are the experimental data and the red dots is a chi-square minimization of a Lorentzian shape fit function. We use the fit function to find the value of total number at the maximum $N_{RFescape}$ and collect data under those conditions.

6.3.2 Initial electron temperature calibration

The electron temperature is determined by the blue photoionization laser wavelength and is very sensitive to the difference between the blue laser photon energy and the atoms' photoionization threshold from the $5P_{3/2}$ state. To calibrate the wavelength of that threshold, a relatively small number of atoms were photoionized such that a plasma would not form. If the blue laser wavelength was below threshold then Rydberg atoms would be created and fewer free electrons would be produced. Above threshold the opposite is true. There is not a sharp transition because even at the low densities used there still is the possibility of electron-Rydberg atom and Rydberg atom-Rydberg atom collisions, as well as a finite frequency width to the blue laser and gradients in the applied electric field. The fraction of free electrons could be measured by observing the electrons that initially strike the detector vs. those that are extracted with an ionization electric field applied a few μs after photoionization. Molecular dynamics simulations showed that the when the laser wavelength was at threshold the initial free electron signal was 50% of the total signal. To determine this threshold frequency, we initially create an atom cloud with a factor of 30 times lower density than that used for generating UNPs by reducing the number of ionized atoms. This avoids complications from Rydberg atom interactions. We then sweep through a range of blue photoionization laser frequencies while applying a mild DC electric field in the Z direction. Two μs after the blue laser pulse, the applied electric field is increased to a value strong enough to field ionize any Rydberg atoms. By tuning the laser wavelength, we can identify the point where roughly half of the electrons initially escape and identify that as the 50 percent ionization value. Figure 6.4 illustrates the relationship between the proportion of escaping electrons and the blue wavelength under a DC field produced by 900mV on the wire grid on the MCP side of plasma; one data point is an average value from 20 shots.

The DC electric field amplitude affects the ionization threshold. We collect our data with different downstream grid voltages, spanning from 450mV to 1500mV. The data in Figure 6.5 is trending in the proper direction. As the voltage on the grid is increased, the electric field directed

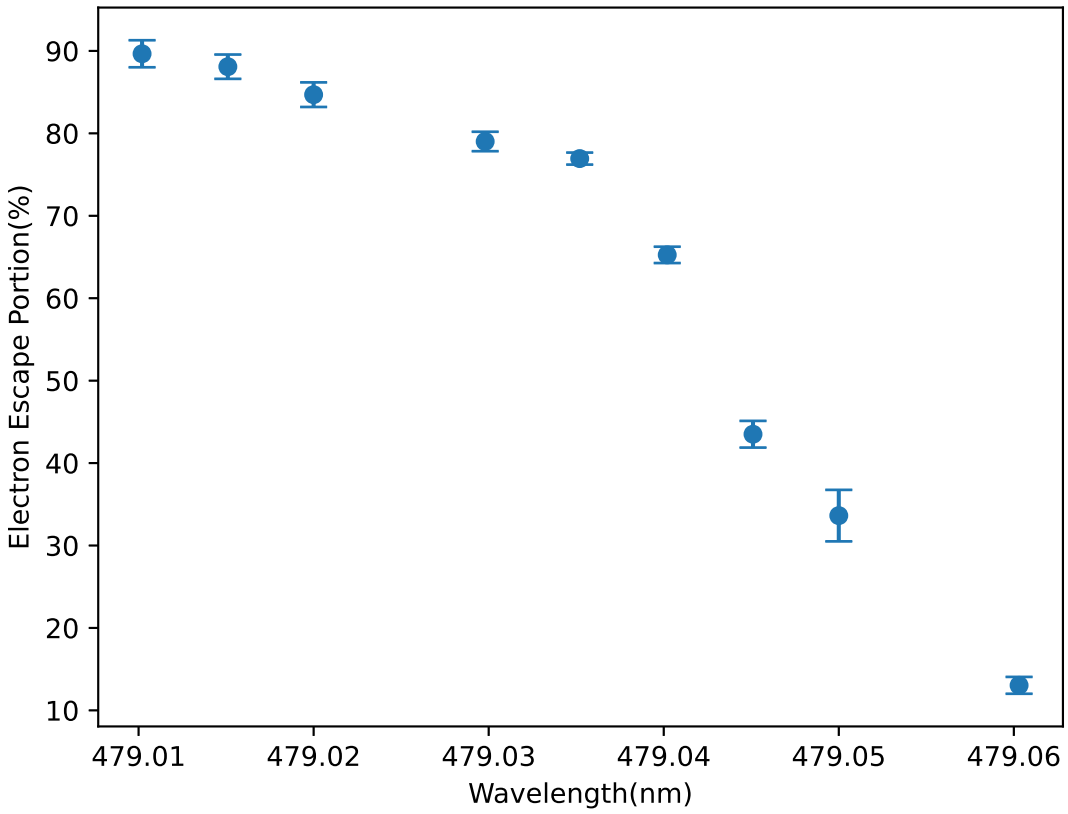

Figure 6.4: This plot illustrates how the electron escape rate changes with the wavelength under a 6.75 V/m electric field. The electron escape rate is defined as the percentage of electrons that escape due to the applied electric field relative to the total number of electrons. By fitting the point at which 50% of electrons escape, we can determine the threshold wavelength for this specific field.

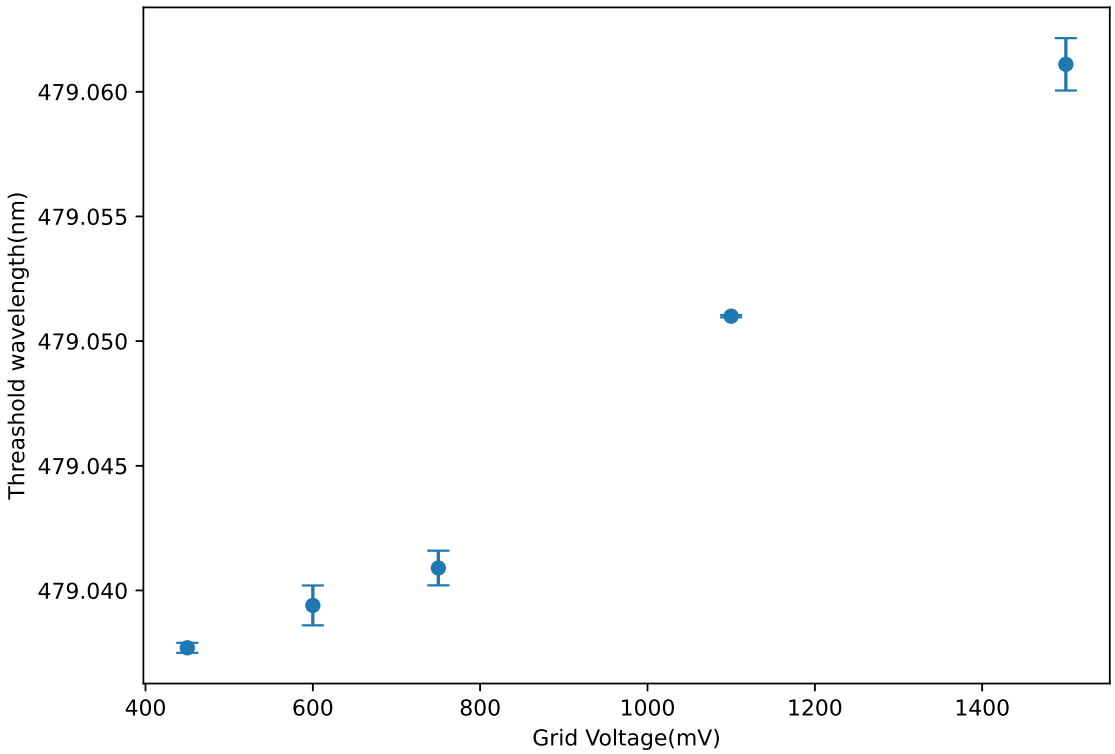

Figure 6.5: This plot demonstrates the relationship between the downstream grid voltage and the corresponding threshold wavelength. The increasing trend in the grid voltage is due to the field shift, which in turn lowers the ionization threshold of the electrons.

away from that grid increases and so the total electric field at the plasma increases. Our model for the total electric field F at the plasma is:

$$F = \sqrt{F_r^2 + (F_{z0} + \alpha\, V_{grid})^2} \tag{6.2}$$

Where F_r and F_{z0} are the stray electric fields in the radial and z direction, respectively, for 0V on the downstream grid. α is a parameter that scales the grid voltage to the z-direction field at the plasma from the grid and $\alpha = 7.5m^{-1}$ as determined from previous work did by John Guthrie [24]. We performed a chi-squared minimization analysis using this data to find the stray field values in the axial and radial direction along with the offset in the blue photoionization laser wavelength between its apparent and true values. This analysis produced values of F_r (1.04 V/m), F_{z0} (-4.11 V/m), and a shift in the blue laser from its nominal values (18.2 pm).

We had intended to have an initial electron temperature of $3.5K$ for the UNPs used to measure the RF heating data. Two shifts are present, though. First, there's a 0.75K shift due to the 18 pm alteration in calibration. This shift was in the direction of a bluer wavelength and thus results in a higher temperature than initially expected. Secondly, there's a shift attributable to electric field heating, which we have assessed through MD simulation from the other parameters obtained in this calibration. From this analysis we determined that our initial electron temperature is $T_e = 5.07 \pm 0.25K$.

6.3.3 ΔT calibration and RF vs kick matching

While it is possible to calibrate the RF-heating-induced temperature rise ΔT for each set of experimental conditions, that is somewhat cumbersome for reasons described below and so a short electric field pulse is used to create a fixed ΔT for comparison to RF-heating data.

We can apply a 16ns FWHM short electric field pulse to "kick" the electrons. This impulse causes to the electrons to oscillate with respect to the ions. Electrons subsequently collide with ions, resulting in energy transfer and, eventually, electron heating as the oscillation damps [4] and the electrons thermalize the energy via collisions. What's particularly noteworthy is that this kick

field introduces a fixed amount of energy into the UNP, regardless of the magnetic field strength. This is due to the period of the kick field being short in time as compared to the timescale of the electron oscillation.

To determine the amount of heat introduced into the system by the "kick" field, we conducted a calibration that relied on a comparison of the heating from the kick to a change in the initial electron temperature induced via a known change in the photoionization laser wavelength. We prepared a UNP with an initial (intended) electron temperature of $3.5K$ and applied the kick field. Subsequently, we prepared another UNP with an initial electron temperature of $2.0K$ greater, achieved by adjusting the blue photoionization laser wavelength. An error in the colder temperature is not a problem for this calibration as it is the energy difference that is critical.

The experiment includes 5 data sets: 3 sets at 3.5K with a 600mV amplitude triangle field with no kick, 1.4V and 1.8V kick applied; 2 sets at 5.5K with a either a 600mV (set 1) or 550mV (set 2) triangle ramp, with no kick field. By comparing the partial and the full electron escape signal of the three no kick sets, which are the 3.5K 600mV, 5.5K 600mV and 5.5K 550mV triangle ramp sets, we are able to interpolate and calculate a triangle field amplitude we need at 5.5K to create the same charge imbalance as 3.5K condition. In other words, at the equivalent amplitude the triangle ramp should cause the same loss of electrons for both the 3.5K and 5.5K cases. After knowing the equivalent amplitude, the partial electron escape for the 5.5K case can be adjusted and so as to make further comparisons. This is done by assuming a linear variation of partial extraction electron escape with the triangle amplitude and using the equivalent amplitude value obtained as described above to determine the equivalent partial electron escape value that allows a direct comparison. Once this charge-imbalance-adjusted number was obtained, we can compare this number with the partial electron escape number at 3.5V no kick, 1.4V kick and 1.8V kick, make our usual quadratic fit, and find the right kick amplitude that raises the electron temperature by 2K. This technique is described in detail in John Guthrie's thesis, chapter 4.6 [24].

As an example of how this adjustment would work, consider the case where the charge imbalance for $3.5K$ was exactly halfway between the two hotter temperature sets. Then the partial

extraction number that would be used for the hotter set to compare to the colder would be the average of the two partial extraction numbers. If the charge imbalance was 3/4 of the way above the lower triangle ramp value on the way to the higher triangle ramp value, then a linear interpolation of the partial extraction numbers at the lower and higher triangle ramps would be performed and matched to the 3/4 value, etc. Standard error propagation was used to determine the uncertainty.

Through this calibration process, we established that a $1.70 \pm 0.1V$ kick results in a plasma temperature increase of 2K.

6.3.4 Measuring RF heating rates vs. β

We employed the same technique as matching the kick amplitude to the $2K$ heating to match a 60MHz RF field to the kick field heating to measuring the RF heating rate as a function of β. These measurements represent the main data that we wanted to collect.

For each data set, 5-6 data conditions were collected. The data signal was the number of electrons that escaped as a result of the partial extraction ramp. One condition had no heating pulses applied to the UNP to establish a baseline. A second condition included the application of a kick pulse to induce a calibrated amount of heating. The rest of the conditions had 60 MHz RF fields applied with different RF amplitudes. The goal was to have a range of amplitudes such that the RF heating from these sets bracketed the heating from the kick pulse. A fit to the electron escape number as a function of RF amplitude was used to determine the RF amplitude whose heating matched that of the kick pulse. Standard error propagation was used to determine the uncertainty of the measurement. In order to avoid heating from turning the RF on and off, the amplitude was increased slowly over 100 $ns$with a time constant of 32 ns and then turned off equally slowly. The total length of the RF pulse was 1.2 μs including the turn-on and turn-off time. MC simulations indicated that this rate of change in amplitude induced an ignorably small amount of heating compared to the $2K$ target.

This data allowed us to determine, at specific magnetic field strengths, the required RF field amplitude to increase the UNP temperature by a known amount. For most of the data collected,

this was $1.36 \pm 0.08K$. For instance, at 10G magnetic field strength, we found that applying a $4.98 \pm 0.311V_{pp}$ RF field as specified by the arbitrary waveform generator used to produce the RF signal used for UNP heating would achieve a $1.36K$ temperature increase. The density for this data was $1.39 \pm 0.04 \times 10^{13} m^{-3}$. We conducted measurements under seven different magnetic field strengths, spanning from weakly magnetized to extremely magnetized electron conditions. With the field amplitude measurements, we were able to establish the relative RF heating rate coefficient versus magnetic field. This measurement constitutes a significant portion of the entire experiment, requiring several months of data collection to achieve the desired level of precision in our error bars. To ensure the reliability and consistency of our results, we conducted a reproducibility test at magnetic field strength of 10 Gauss by conducting measurements separated by several months. It's worth noting that this technique is not newly developed, and for the original description of the data collection procedure and analysis, please see John Guthrie's thesis, chapter 4 and 5 [24].

It is important to note, however, that after that work was completed, we discovered an error in the magnetic field calibration. The magnetic field is determined spectroscopically by measuring the Zeeman shift between the stretched m_F states on the ^{85}Rb cycling transition. The data in John's thesis at $65G$ is at $50G$ and the data at $134G$ is at $107G$.

6.3.5 Kick equilibrium time check

In our 2021 study when matching the 'kick' to the RF, we operated under the assumption that the electrons were in equilibrium when applying the partial extraction ramp. However, as we transitioned to measuring the RF heating rate under strongly or extremely magnetized conditions, we noticed a error. Specifically, the 'kick' field resulted in even less partial electron escape than when there was no kick, if the delay between the 'kick' and the partial extraction ramp ($4\mu s$) remained consistent with our data collection in low magnetic fields.

This observation suggested that the electrons were not in equilibrium. In particular, there was concern that the assumption of thermal equilibrium did not apply at higher magnetic field strengths as the electron thermalization times are expected to be longer [62]. Measurements and calculations

in a trapped pure electron non-neutral plasma showed [62] that as the degree of magnetization increased the energy equipartition rate, which is the rate at which thermal energy equilibrates between the axial and radial directions in the trap, decreased significantly as the degree of electron magnetization increased. The equipartition rate is not the equilibration rate, but it is reasonable to expect that the two are proportional to one another [17]. We were aware of this issue and had created two tests to check on the thermal equilibrium assumption. One test consisted of examining the matching RF heating field amplitude to kick data as a function of how much of the partially extracted electron signal was used (i.e. how long the signal was integrated after the partial extraction voltage). In equilibrium, the expectation would be that the matching RF amplitude would be insensitive to the amount of partial extraction voltage signal used. The additional measurements described in this section show that this test was flawed and could signal sufficient equilibration when that was not the case. The second test involved altering the time between the end of the triangle ramp and the partial extraction voltage by up to 2 μs [24]. In retrospect, these delay times were not long enough for sufficient signal-to-noise.

To test whether the electrons were in sufficient thermal equilibrium, we repeated magnetic field RF heating measurements with longer delay times between the RF heating/kick and the partial extraction voltage. Each repeated data set took anywhere from two to four additional days of data collection. If the electrons were in thermal equilibrium, then the RF heating amplitude that matched the kick-induced heating should not change as the delay time was extended. To compare the data to expectations, we plotted the ratio of the RF matching amplitude taken at shorter times to longer times. For instance, at 107 G, the RF matching amplitude with a 4 μs delay was 4.09$\pm$0.78 V and a 8 μs delay 7.63$\pm$0.47 V. These data points are different by nearly 4 standard deviations, indicating that 4 μs delay at this magnetic field was not sufficiently long. For the UNP conditions at the shorter delay time, 4 μs is 5 equipartition times (e.g. the equipartition time is about 0.8 μs) as calculated via Ref. [62].

Figure 6.6 shows a plot of the results from all four sets of data we collected testing this thermal equilibrium assumption. The ratio of the RF matching amplitude obtained for the shorter delay

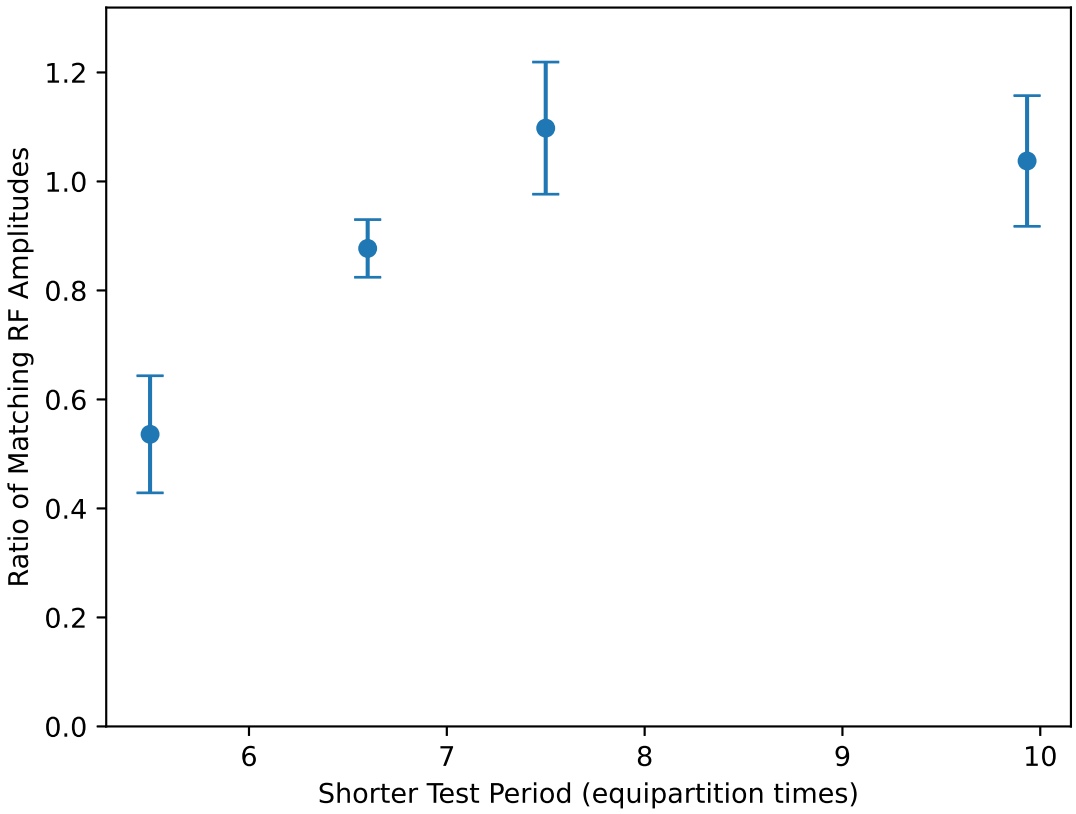

Figure 6.6: Kick equilibrium check: each data point represents an analysis based on a pair of measurements: the ratio of the matching RF amplitude from the short test period($4\mu s$) to that of the longer test period($8\mu s$ or $12\mu s$). The test period is the time between the end of the triangle ramp and the start of the partial extraction voltage. The left three points use the same short($4\mu s$) and longer test period($8\mu s$), while the right point represents the 127G data, which requires a longer equilibration time for the longer test period (12 µs). The x-axis represents the ratio of the longer test period to the equipartition time.

time to the amplitude from the longer delay time is plotted as a function of the shorter delay time expressed in units of equipartition time given the UNP conditions. The magnetic fields at which the data were tested correspond to 107G, 75G, 51G, and 127G from left to right in Figure 6.6. The 127G delays were longer than the others since the need for a longer equilibration time was anticipated prior to any measurements at these fields were made. From this data we estimate that 8 equipartition times should be long enough to ensure sufficient thermal equilibration.

6.3.6 RF electric field calibration

The presence of many conducting surfaces around the plasma region along with the fact that there is not 100% coupling of the applied RF into the vacuum chamber makes any calculation of the applied RF amplitude difficult. Instead, we measure the RF amplitude by using the UNPs. To do this we match ΔT for two different conditions: the usual RF heating pulse applied to collect data that is turned on and off adiabatically ("slow turn-off") mentioned earlier and an RF heating pulse that is instead turned off suddenly at the end of an RF cycle when the waveform generator output is zero ("fast turn-off").

In the limit of perfect electronics, turning off the RF heating pulse suddenly when it is at zero volts is at a time at which the center-of-mass velocity of the electrons is at the maximum of its oscillation in response to the RF field for high-frequency RF fields. In the absence of an applied RF field, the electrons continue to oscillate at their natural resonant frequency but that oscillation damps due to electron-ion collisions and eventually the center-of-mass kinetic energy thermalizes into heat. The amount of heat depends on the amplitude of the center-of-mass velocity oscillation due to the RF, and in turn that velocity amplitude is determioend by the RF amplitude. Through matching ΔT for the slow and fast turn-off RF pulses and the calibration of ΔT described in section 6.3.4 above the absolute value of η and the RF amplitude E can be determined.

The electronics in the experiment are not perfect, of course, which complicates this calibration. The response of the electrodes in the vacuum chamber to the fast turn-off RF pulse were measured by monitoring the voltage at the feedthrough to the chamber. Cable effects were accounted for by using variable numbers of cables and extrapolating. The electrode response was modeled as an RLC circuit and the measured voltage at the feedthrough was sufficient to fix all the needed parameters. Once the RLC parameters were characterized, the electric field at the plasma due to the applied RF fast turn-off and slow turn-off pulses were calculated and the measured ΔT match between the heating induced by the fast and slow turnoffs was used to calibrate the value of the RF field E and the absolute (i.e. not relative) value of η. See [24] for additional details and

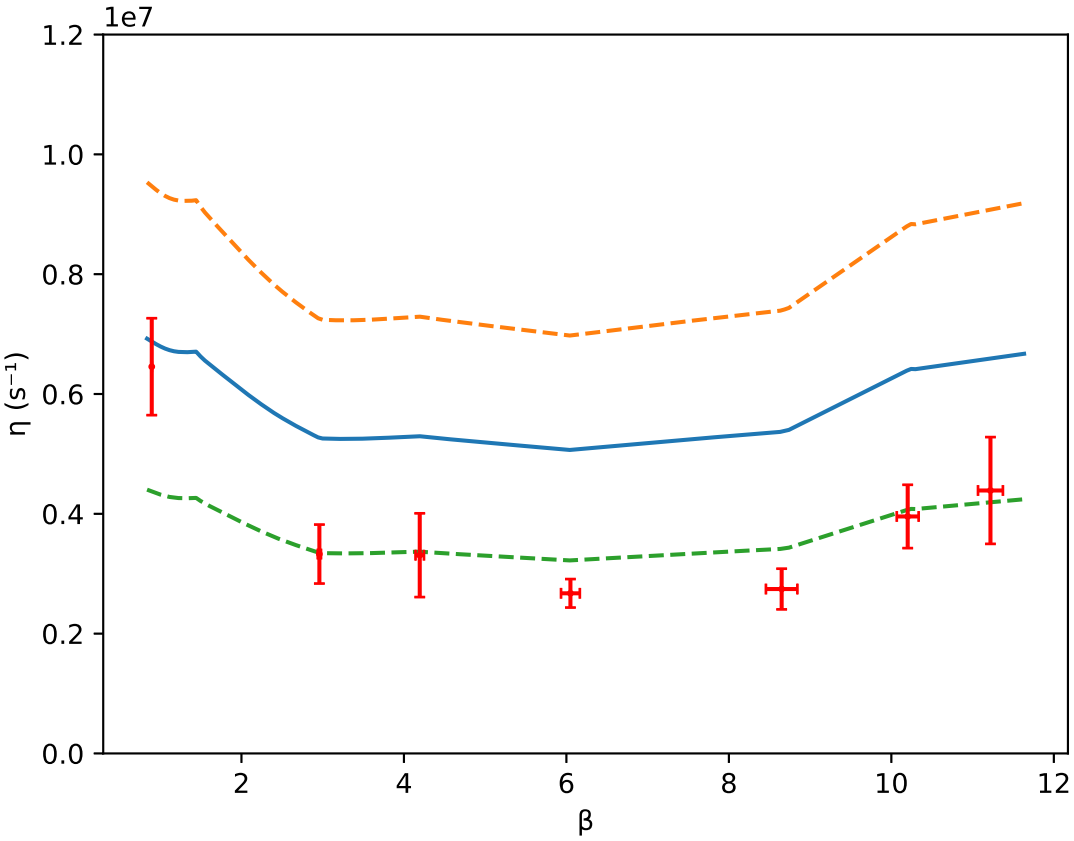

Figure 6.7: This figure presents the results of our RF heating experiment compared to the theoretical prediction, focusing on the relationship between β and η. The solid blue line represents the predicted theoretical results based on Guthrie's work in [27]. The red and green dashed lines indicate one standard deviation of systematic variation in the calibration of η. The red dot, along with its associated error bar, represents the RF heating rate derived from our experimental data. These results cover a wide range from the weakly magnetized regime (10 Gauss) to the extremely magnetized regime (140 Gauss).

information. For the work in this thesis, it was determined that $1V_{pp}$ on the waveform generator corresponded to $1.17(22)\frac{V}{m}$ RF electric field amplitude at the plasma.

6.4 Experimental results and discussion

The heating rate η vs. magnetic strength β is shown in figure Figure 6.7 and Figure 6.8. We plot the theory prediction compared to the experimental measurements and the simulation results separately for clarity.

Our measurement technique measures relative changes in η much more precisely than the absolute value of η. This is because the calibration of η has a 38% systematic uncertainty associated with it for our measurements. There are some unfavorable factors such that several percent precision in matching the ΔT of the fast- and slow-turn-off leads to tens of percent of uncertainty. The dash lines in fig. Figure 6.7 represent one standard deviation of systematic variation in the calibration of η. At low magnetic field the theory prediction, simulation, and measurement are in agreement within this systematic uncertainty.

Both the experimental measurements and the linear response theory predictions, and the MD simulation and linear response theory predictions, agree with each other qualitatively but not quantitatively. This is not surprising in the case of the linear response theory given its approximations. The lack of agreement between MD simulation and experiment would initially seem more difficult to understand but given the convergence and computational time challenges it is difficult to know whether the disagreement represents a problem for the theory (or simulation) or is a numerical error. The cause for the quantitative disagreement between theory and experiment is currently unknown, although there are multiple hypotheses. It is always possible that there is some undetected systematic error in the experimental data, but care was taken to exclude such a possibility. In particular, data was collected to check that η scaled appropriately with n and tests were made at 50G with reduced RF amplitude E to show that the deviation was not due to nonlinearity effects. The reduced E data was consistent the larger E data at the 15% level. Most of our data was taken with the RF-induced center of mass velocity of the electrons being less than $3\frac{km}{s}$.

Several MD simulations were conducted with parameters similar to the experimental parameters. Due to runtime constraints, it was not possible to match the total number of particles in the experiment. Instead, we simulated the evolution of 7500 electrons and 10000 ions UNP for 2.2 μs, setting the same initial temperature and adjusting the spatial size so that the density matched the experiment to make a better comparison. During the first 1 μs we let the UNP evolve and come into thermal equilibrium. At 1 μs we apply the exact form of the slow turn-on/off RF field with a amplitude of $8V/m$ for 1.2 μs, mimicking the RF field we applied for the experiment. At the

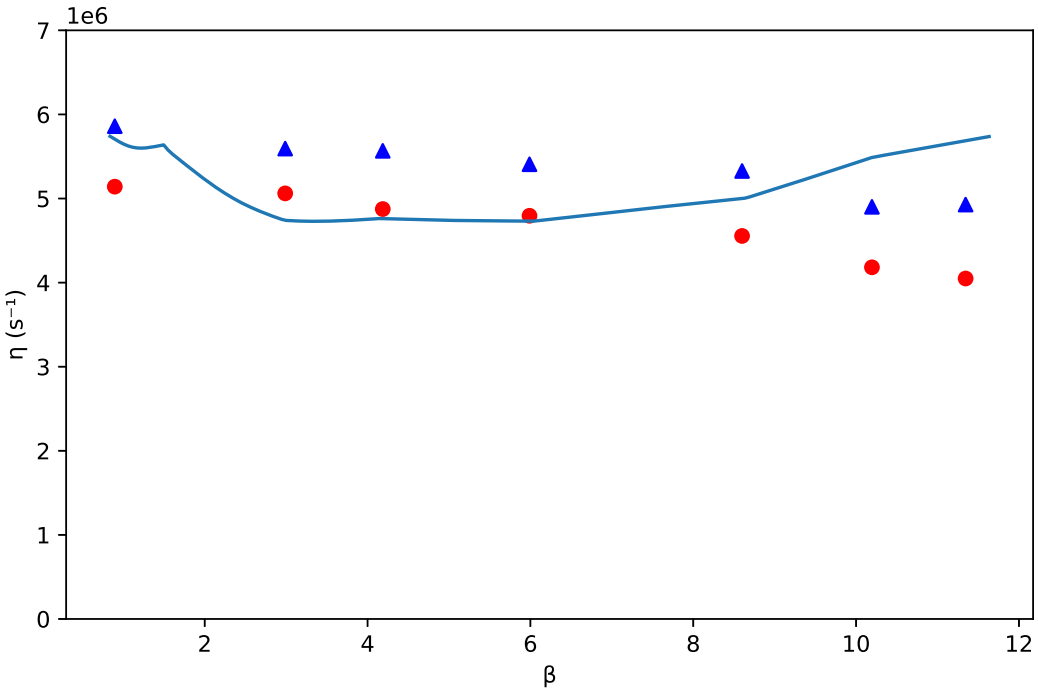

Figure 6.8: This figure shows the RF heating rate simulation results vs theory results, The solid blue line represents the predicted theoretical results based on Guthrie's work in [27]. The red and blue data points in the plot represent our simulation results conducted under the conditions outlined in this section. The distinction between these two datasets lies in the choice of the softening parameter α. This discrepancy serves as an indicator that the code encounters convergence issues when employing different α values. Specifically, the blue dataset employs an α value of 100 nm, while the red dataset uses $\alpha = 500nm$.

end of this time the electron temperature at 2.2 μs is calculated using the technique mentioned in chapter 4.2. These simulations were run for several different values of β that spanned the same range as our experimental measurements. Following the equation (6.1) at the start of this section, the heating amounts were turned into a η coefficient and figure Figure 6.8 shows the simulation results.

When comparing with theory/simulation and experiment results, the theory/simulation doesn't have the"dip" at around 70 Gauss. The fact that the theory/simulation is over-predicting η indicates that the theory/simulation is not missing a class of collisions that contributes to η such as short-range collisions. The situation is not indicative of some unanticipated heating mechanism

being present (e.g. electron cyclotron heating, which should be ignorably small for all conditions studied).

The quantitative disagreement with the MD simulation suggests that either there is relevant physics that has not been included or there is a persistent numerical problem (or both). Convergence challenges are discussed in chapter 3.3 above and while the simulations are perhaps not fully converged the shifts that are observed are not large enough to explain the difference between simulation and experiment. This doesn't rule out a persistent numerical problem that is unresolved even at the fine timesteps used, but there is no candidate that we have identified for such a problem.

The disagreement between simulation and experimental measurement thus remains unresolved. We plan to conduct measurements in the future at higher electron temperatures. This increases the required thermalization times during the test period but that should be able to be accommodated. Higher magnetic fields will be needed to cover the same range of magnetization. We expect that as the electron temperature is increased theory calculations move closer to perturbation theory calculations and numerical issues should be less significant. On the simulation side, there is a need to enhance the code efficiency to enable more efficient simulations and the exploration of smaller time steps.

Recent results that have been obtained related to a completely different UNP experiment in the our research group may provide for an explanation of the quantitative disagreement between the theory predictions and experimental RF heating measurements. However, these recent results are part of a work in progress. At the time of the writing of this thesis, there are still many detailed questions, measurements that need to be made, and analysis that needs to be performed.

The new UNP experiment in our research group is designed to study use field ionization of Rydberg atoms to measure RF electric field amplitudes. Highly-excited Rydberg atoms can be ionized by a sufficiently strong electric fields. DC electric fields are commonly applied to do so. For Rydberg atoms in low angular momentum states, the field F required to ionize an atom in quantum state n is [63]

$$F = \frac{3.21 \times 10^{10}}{n^4} \frac{V}{m} \tag{6.3}$$

A typical Rydberg atom binding energy is about 4 times $k_B T_e$ [10]. Experiments are being conducted with colder UNPs than those used in this thesis. For a $T_e = 2K$ UNP Rydberg atoms will have a typical binding energy corresponding to $n = 162$, requiring an ionization field F of $83\frac{V}{m}$. More deeply bound Rydberg atoms require higher electric fields.

There are limits in our system to how high a DC electric field can be applied. The problem is that as the DC electric field is increased in our relatively long and narrow geometry electrons are pulled into the wire grids and/or do not make it to the MCP. RF fields don't have this problem since they oscillate. As long as the RF field frequency is much smaller than the Rydberg electron orbit frequency, the RF field is effectively a DC field. At $n = 162$ the electron orbits the nucleus roughly 1.5×10^9 per second and so RF fields at 10s of MHz are effectively DC.

Our new experiments have been done to deliberately create low-density gases of Rydberg atoms at a chosen binding energy, it is similar to the measurement mentioned in Section 6.3.2. The goal was to find the RF field amplitude that ionizes these Rydbergs and thereby calibrate the field. Pairs of these measurements calibrate not only the RF amplitude but also are an alternative way to calibrate the blue laser wavelength.

An odd observation was made in these experiments. A fraction of weakly bound Rydberg atoms was not easily ionized by the RF field. This was true despite the field being able to ionize more tightly bound Rydberg atoms. One possible explanation is that the RF amplitude varies substantially in space, being strong for some locations in the low-density Rydberg gas, and weak in others.

As a test, experiments were performed where the Rydberg gas was physically displaced by changing the track position of the AH coils prior to laser excitation. There was a clear dependence of the Rydberg ionization on position.

It was expected that the RF field is largely longitudinal along the axis. That is what an electrostatic calculation predicts. For a 60MHz RF field, the RF wavelength is $5.0m$, much larger than the size of the apparatus and so the expectation was that an electrostatic calculation would be accurate. But there are inductances and capacitances in the ground return path for the RF field current. If the

inductances are large enough, then surfaces that are supposed to be at ground may not be at ground and there could be a structure to the RF field amplitude.

If there is a variation in the longitudinal electric field amplitude, then since $\nabla \cdot \vec{E} = 0$ (at least approximately) there must be a radial electric field. The reason that a radial field matters for the RF heating measurement is that a low magnetic field the electrons can oscillate in response to such a field while a high magnetic fields the electrons are pinned to the magnetic field lines. The larger oscillation amplitude at lower electric fields "artifically" boosts their heating, making the apparent heating coefficient for those fields too large.

The experiments that will characterize the RF amplitude variation scale are underway. Preliminary estimates with a sine-like variation longitudinally indicate a length scale of about 700 μm (i.e. a value of $k = 9 \times 10^4 m^{-1}$).

Using $\nabla \cdot \vec{E} = 0$ with this longitudinal variation and assuming a small-parameter approximation in the radial field, the oscillation amplitude of the electrons in the UNP can be calculated in the applied magnetic field and averaged over all electrons in the UNP.

Assuming that the longitudinal and transverse heating coefficients are the same (which is not the case [64]) and assuming that the calibration at 10.7 G is still valid (which has to be checked), a correction factor for all fields can be developed and the result of this correction factor on the data can be shown in the blue triangle data of figure Figure 6.9 This is an intriguing result as now the experiment is in agreement with the prediction. But, this is highly speculative and very preliminary: the spatial variation scale has yet to be precisely measured, the difference in longitudinal and transverse conductivity has to be incorporated into the analysis, simulations and other tools need to be used to determine whether the RF calibration is still valid, and the rough shape of the RF amplitude has to be established.

6.5 Conclusion

We have measured the absorptive part of the AC conductivity as a function of electron magnetization from the weakly magnetized to extremely magnetized regimes in an ultracold neutral

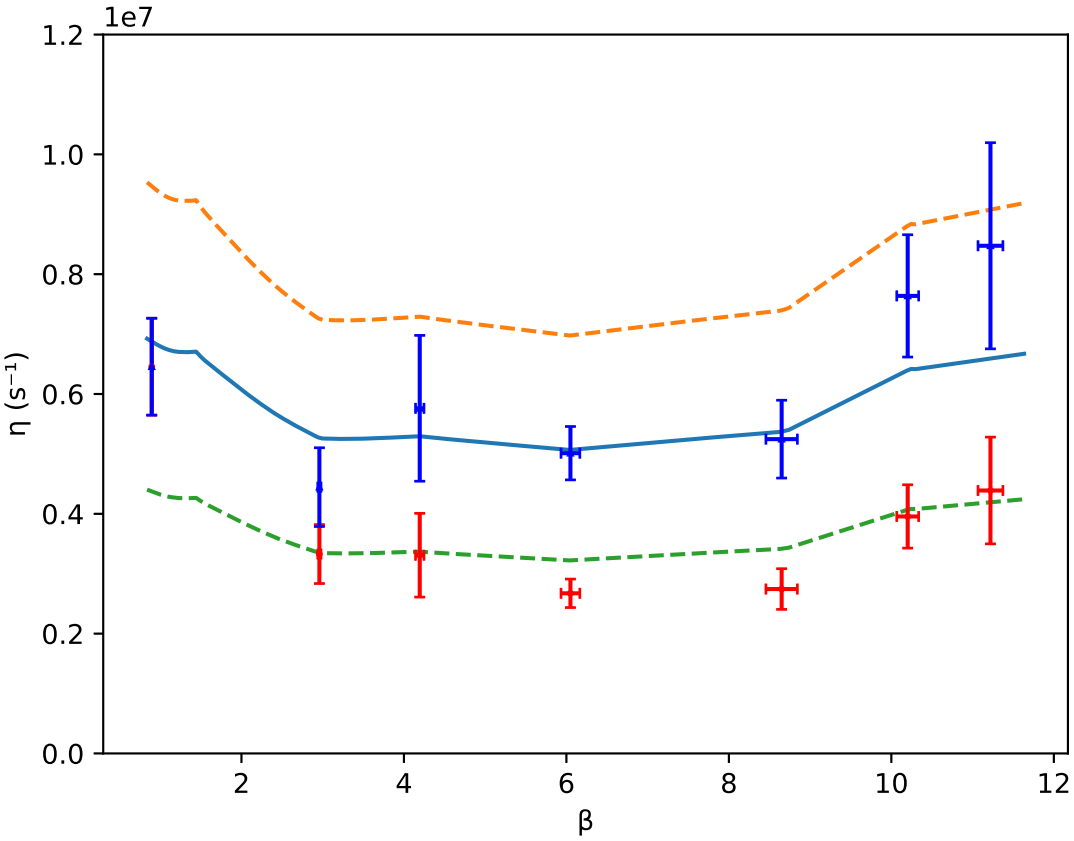

Figure 6.9: This figure provides a comparison between experimental results and theoretical predictions. The dashed line, solid line, and red dot correspond to the same data as shown in Figure 6.7. The blue dot represents the experimental data adjusted to account for the spatial variation of the RF field and the assumptions detailed in this section.

plasma using an applied frequency larger than the electron plasma frequency (i.e. through applying high-frequency RF).

The low densities and cold electron temperatures of the UNPs is highly advantageous for these studies. Obtaining the same degree of magnetization in (the much more common) hotter plamsas would require fields of 1kT or greater rather than the modest laboratory fields used in our experiments.

Our measurement was done via matching the amount of heating induced by an applied RF field to a calibrated amount heating in an ultracold neutral plasma. Despite the fact that the electron magnetization is changing substantially over the range of the fields that were applied, the observed variation of the absorptive part of the AC conductivity of the plasma did not change radically, with the value at the highest field similar to the value at the lowest field, albeit with some variation in between.

The experimental results were compared to both linear response theory and molecular dynamics simulation and while they agree qualitatively there are quantitative differences between the experimental and linear response theory and simulation results. The disagreement with linear response theory is not as surprising given its incompleteness in other contexts and the likelihood that its approximations were strained for the parameters studied. However, it is not clear where the disagreement with the MD simulation is coming from. Future studies at higher electron temperatures have the potential to help discover where the observed discrepancies are originating, and recent results indicating a variation of the RF amplitude with position are highly intriguing.

Bibliography

[1] M Lyon and S L Rolston. Ultracold neutral plasmas. *Rep. Prog. Phys.*, 80(1):017001, January 2017.

[2] TC Killian, S Kulin, SD Bergeson, Luis A Orozco, C Orzel, and SL Rolston. Creation of an ultracold neutral plasma. *Physical Review Letters*, 83(23):4776, 1999.

[3] S Kulin, TC Killian, SD Bergeson, and SL Rolston. Plasma oscillations and expansion of an ultracold neutral plasma. *Physical review letters*, 85(2):318, 2000.

[4] Wei-Ting Chen, Craig Witte, and Jacob L Roberts. Observation of a strong-coupling effect on electron-ion collisions in ultracold plasmas. *Physical Review E*, 96(1):013203, 2017.

[5] P Gupta, S Laha, CE Simien, H Gao, J Castro, TC Killian, and T Pohl. Electron-temperature evolution in expanding ultracold neutral plasmas. *Physical review letters*, 99(7):075005, 2007.

[6] Thomas C Killian, T Pattard, T Pohl, and JM Rost. Ultracold neutral plasmas. *Physics reports*, 449(4-5):77–130, 2007.

[7] Thomas K Langin, Grant M Gorman, and Thomas C Killian. Laser cooling of ions in a neutral plasma. *Science*, 363(6422):61–64, 2019.

[8] Francis Robicheaux and James D Hanson. Simulation of the expansion of an ultracold neutral plasma. *Physical review letters*, 88(5):055002, 2002.

[9] TC Killian, MJ Lim, S Kulin, R Dumke, SD Bergeson, and SL Rolston. Formation of rydberg atoms in an expanding ultracold neutral plasma. *Physical review letters*, 86(17):3759, 2001.

[10] G Bannasch and T Pohl. Rydberg-atom formation in strongly correlated ultracold plasmas. *Physical Review A*, 84(5):052710, 2011.

[11] Scott D Baalrud and Jérôme Daligault. Transport regimes spanning magnetization-coupling phase space. *Physical Review E*, 96(4):043202, 2017.

[12] Puchang Jiang and Jacob L Roberts. Electric field influences on the initial electron temperature of ultracold plasmas. *Physics of Plasmas*, 26(4), 2019.

[13] Puchang Jiang, John Guthrie, and Jacob L Roberts. Many-body collision contributions to electron momentum damping rates in a plasma influenced by electron strong coupling. *Physics of Plasmas*, 27(1), 2020.

[14] Ross E Falcon, Gregory A Rochau, James E Bailey, Thomas A Gomez, Michael Houston Montgomery, Donald E Winget, and Taisuke Nagayama. Laboratory measurements of white dwarf photospheric spectral lines: Hβ. *The Astrophysical Journal*, 806(2):214, 2015.

[15] AB Zylstra, AL Kritcher, OA Hurricane, DA Callahan, K Baker, T Braun, DT Casey, D Clark, K Clark, T Döppner, et al. Record energetics for an inertial fusion implosion at nif. *Physical review letters*, 126(2):025001, 2021.

[16] R Aymar, P Barabaschi, and Y Shimomura. The iter design. *Plasma physics and controlled fusion*, 44(5):519, 2002.

[17] Lyman Spitzer. *Physics of fully ionized gases*. Courier Corporation, 2006.

[18] Francis F Chen et al. *Introduction to plasma physics and controlled fusion*, volume 1. Springer, 1984.

[19] Setsuo Ichimaru. Strongly coupled plasmas: high-density classical plasmas and degenerate electron liquids. *Reviews of Modern Physics*, 54(4):1017, 1982.

[20] Stanislav G Kuzmin and Thomas M O'Neil. Numerical simulation of ultracold plasmas. *Physics of Plasmas*, 9(9):3743–3751, 2002.

[21] Guy Dimonte and Jerome Daligault. Molecular-dynamics simulations of electron-ion temperature relaxation in a classical coulomb plasma. *Physical review letters*, 101(13):135001, 2008.

[22] Scott D Baalrud. Transport coefficients in strongly coupled plasmas. *Physics of Plasmas*, 19(3), 2012.

[23] Paul E Grabowski, Michael P Surh, David F Richards, Frank R Graziani, and Michael S Murillo. Molecular dynamics simulations of classical stopping power. *Physical review letters*, 111(21):215002, 2013.

[24] John M Guthrie. *Off-Resonant RF Heating of Strongly Magnetized Electrons in Ultracold Neutral Plasma*. PhD thesis, Colorado State University, 2021.

[25] B Hu, W Horton, C Chiu, and T Petrosky. Coulomb scattering in a strong magnetic field. *Physics of Plasmas*, 9(4):1116–1124, 2002.

[26] Hrachya B Nersisyan, Günter Zwicknagel, and Claude Deutsch. Stopping power of ions in a magnetized plasma: Binary collision formulation. In *Plasma Science and Technology-Basic Fundamentals and Modern Applications*. IntechOpen, 2019.

[27] John M Guthrie and Jacob L Roberts. Finite-amplitude rf heating rates for magnetized electrons in neutral plasma. *Physics of Plasmas*, 28(5), 2021.

[28] H Ludvigsen, A Äijälä, A Pietiläinen, H Talvitie, and E Ikonen. Laser cooling of rubidium atoms in a vapor cell. *Physica Scripta*, 49(4):424, 1994.

[29] Truman M Wilson. *Dynamics of low-density ultracold plasmas in externally applied electric and magnetic fields*. PhD thesis, Colorado State University, 2013.

[30] Michel A Cuendet and Wilfred F van Gunsteren. On the calculation of velocity-dependent properties in molecular dynamics simulations using the leapfrog integration algorithm. *The Journal of chemical physics*, 127(18), 2007.

[31] Dusanka Janezic and Bojan Orel. Implicit runge-kutta method for molecular dynamics integration. *Journal of chemical information and computer sciences*, 33(2):252–257, 1993.

[32] Konstantin N Kudin and Gustavo E Scuseria. A fast multipole method for periodic systems with arbitrary unit cell geometries. *Chemical Physics Letters*, 283(1-2):61–68, 1998.

[33] Gautham Dharuman, Liam G Stanton, James N Glosli, and Michael S Murillo. A generalized ewald decomposition for screened coulomb interactions. *The Journal of chemical physics*, 146(2), 2017.

[34] Sanat Kumar Tiwari and Scott D Baalrud. Reduction of electron heating by magnetizing ultracold neutral plasma. *Physics of Plasmas*, 25(1):013511, 2018.

[35] John C Stewart and Kedar D Pyatt Jr. Lowering of ionization potentials in plasmas. *Astrophysical Journal, vol. 144, p. 1203*, 144:1203, 1966.

[36] YC Chen, CE Simien, S Laha, P Gupta, YN Martinez, PG Mickelson, SB Nagel, and TC Killian. Electron screening and kinetic-energy oscillations in a strongly coupled plasma. *Physical review letters*, 93(26):265003, 2004.

[37] M Lyon and SD Bergeson. The influence of electron screening on disorder-induced heating. *Journal of Physics B: Atomic, Molecular and Optical Physics*, 44(18):184014, 2011.

[38] Truman Wilson, Wei-Ting Chen, and Jacob Roberts. Influence of electron evaporative cooling on ultracold plasma expansion. *Physics of Plasmas*, 20(7):073503, 2013.

[39] Michael S Murillo and Scott D Bergeson. Ultracold neutral plasmas well into the strongly coupled regime. In *Advances in atomic, molecular, and optical physics*, volume 64, pages 223–271. Elsevier, 2015.

[40] G Bannasch, J Castro, P McQuillen, T Pohl, and TC Killian. Velocity relaxation in a strongly coupled plasma. *Physical review letters*, 109(18):185008, 2012.

[41] Trevor S Strickler, Thomas K Langin, Paul McQuillen, J Daligault, and Tom C Killian. Experimental measurement of self-diffusion in a strongly coupled plasma. *Physical Review X*, 6(2):021021, 2016.

[42] R Haenel, M Schulz-Weiling, J Sous, H Sadeghi, M Aghigh, L Melo, JS Keller, and ER Grant. Arrested relaxation in an isolated molecular ultracold plasma. *Physical Review A*, 96(2):023613, 2017.

[43] Liam G Stanton and Michael S Murillo. Ionic transport in high-energy-density matter. *Physical Review E*, 93(4):043203, 2016.

[44] Scott D Baalrud and Jérôme Daligault. Extending plasma transport theory to strong coupling through the concept of an effective interaction potential. *Physics of Plasmas*, 21(5):055707, 2014.

[45] RS Fletcher, XL Zhang, and SL Rolston. Using three-body recombination to extract electron temperatures of ultracold plasmas. *Physical review letters*, 99(14):145001, 2007.

[46] Peter Mansbach and James Keck. Monte carlo trajectory calculations of atomic excitation and ionization by thermal electrons. *Physical Review*, 181(1):275, 1969.

[47] JA Frenje, PE Grabowski, CK Li, FH Séguin, AB Zylstra, M Gatu Johnson, RD Petrasso, V Yu Glebov, and TC Sangster. Measurements of ion stopping around the bragg peak in high-energy-density plasmas. *Physical review letters*, 115(20):205001, 2015.

[48] FL Hinton and Richard D Hazeltine. Theory of plasma transport in toroidal confinement systems. *Reviews of Modern Physics*, 48(2):239, 1976.

[49] JP Morrison, CJ Rennick, JS Keller, and ER Grant. Evolution from a molecular rydberg gas to an ultracold plasma in a seeded supersonic expansion of no. *Physical review letters*, 101(20):205005, 2008.

[50] Wei-Ting Chen, Craig Witte, and Jacob L Roberts. Damping of electron center-of-mass oscillation in ultracold plasmas. *Physics of Plasmas*, 23(5):052101, 2016.

[51] MS Murillo. Using fermi statistics to create strongly coupled ion plasmas in atom traps. *Physical review letters*, 87(11):115003, 2001.

[52] RR Goforth and P Hammerling. Recombination in an expanding laser-produced plasma. *Journal of Applied Physics*, 47(9):3918–3922, 1976.

[53] Nathaniel R Shaffer and Scott D Baalrud. The barkas effect in plasma transport. *Physics of Plasmas*, 26(3):032110, 2019.

[54] Byeoung Ick Cho, T Ogitsu, K Engelhorn, AA Correa, Y Ping, JW Lee, Lee Jin Bae, D Prendergast, RW Falcone, and PA Heimann. Measurement of electron-ion relaxation in warm dense copper. *Scientific reports*, 6:18843, 2016.

[55] Tobias Dornheim, Simon Groth, and Michael Bonitz. The uniform electron gas at warm dense matter conditions. *Physics Reports*, 744:1–86, 2018.

[56] Claude Deutsch and Gilles Maynard. Ion stopping in dense plasmas: a basic physics approach. *Matter and Radiation at Extremes*, 1(6):277, 2018.

[57] D. A. Yager-Elorriaga, M. R. Gomez, D. E. Ruiz, S. A. Slutz, A. J. Harvey-Thompson, C. A. Jennings, P. F. Knapp, P. F. Schmit, M. R. Weis, T. J. Awe, G. A. Chandler, M. Mangan, C. E. Myers, J. R. Fein, B. R. Galloway, M. Geissel, M. E. Glinsky, S. B. Hansen, E. C. Harding, D. C. Lamppa, W. E. Lewis, P. K. Rambo, G. K. Robertson, M. E. Savage, G. A. Shipley, I. C. Smith, J. Schwarz, D. J. Ampleford, K. Beckwith, K. J. Peterson, J. L. Porter, G. A. Rochau, and D. B. Sinars. An overview of magneto-inertial fusion on the z machine at sandia national laboratories. *NUCLEAR FUSION*, 62(4), APR 1 2022.

[58] Bruce T. Tsurutani, Gary P. Zank, Veerle J. Sterken, Kazunari Shibata, Tsugunobu Nagai, Anthony J. Mannucci, David M. Malaspina, Gurbax S. Lakhina, Shrikanth G. Kanekal, Keisuke

Hosokawa, Richard B. Horne, Rajkumar Hajra, Karl-Heinz Glassmeier, C. Trevor Gaunt, Peng-Fei Chen, and Syun-Ichi Akasofu. Space plasma physics: A review. *IEEE TRANSACTIONS ON PLASMA SCIENCE*, 2022 NOV 23 2022.

[59] D.H.E. Dubin and T.M. O'Neil. Trapped nonneutral plasmas, liquids, and crystals. *Rev. Mod. Phys.*, 71:87–172, 1999.

[60] Scott D Baalrud and Trevor Lafleur. dc electrical conductivity in strongly magnetized plasmas. *Physics of Plasmas*, 28(10), 2021.

[61] Louis Jose and Scott D Baalrud. A generalized boltzmann kinetic theory for strongly magnetized plasmas with application to friction. *Physics of Plasmas*, 27(11), 2020.

[62] Michael E Glinsky, Thomas M O'Neil, Marshall N Rosenbluth, Kenji Tsuruta, and Setsuo Ichimaru. Collisional equipartition rate for a magnetized pure electron plasma. *Physics of Fluids B: Plasma Physics*, 4(5):1156–1166, 1992.

[63] Thomas F Gallagher. Rydberg atoms. In *Springer Handbook of Atomic, Molecular, and Optical Physics*, pages 231–240. Springer, 1994.

[64] Kyoko Matsuda. Classical anomalous absorption in strongly magnetized plasmas and effective shielding length. *Physical Review Letters*, 46(7):481, 1981.